ÉLECTRONIC PROPERTIES OF NIOBIUM MONOXIDE
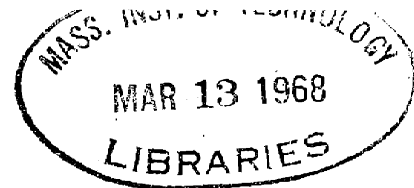
by

EDWARD RILEY POLLARD, JR.

B.Sc.   Massachusetts Institute of Technology (1960)

S.M.   Rensselaer Polytechnic Institute (1963)

Submitted in partial fulfillment of the requirements

for the degree of

DOCTOR OF PHILOSOPHY

at the

MASSACHUSETTS INSTITUTE OF TECHNOLOGY

1968

Signature of Author
Department of Metallurgy
and Materials Science

Signature of Professor
in Charge of Research

Signature of Chairman of
Departmental Committee on
Graduate Studies

ELECTRONIC PROPERTIES OF NIOBIUM MONOXIDE

by

EDWARD RILEY POLLARD, JR.

Submitted to the Department of Metallurgy and Materials Science on
January 12, 1968 in Partial Fulfillment of the Requirements for the
Degree of DOCTOR OF PHILOSOPHY.

ABSTRACT

Niobium monoxide has a crystal structure based on the rocksalt
lattice but containing 25 percent vacancies on both the anion and cation
sublattices. The point positions occupied by the three niobium and the
three oxygen atoms are $\left(\frac{1}{2}\frac{1}{2}0\right)\mathbb{O}$ and $\left(\frac{1}{2}00\right)\mathbb{O}$ respectively. Its space
group is considered as 0_h^1.

Niobium monoxide has a hardness comparable to sapphire, cleaves
easily on $\langle 100\rangle$, a melting point of about 1950°C, and a superconducting
transition temperature of 1.45°K. It exhibits normal metallic resistiv-
ity from liquid helium temperature to 300°K, having a value of about
twenty micro-ohm-cm at room temperature. The low temperature
resistivity exhibits a T^5 dependence analogous to the behavior of a non-
transition element.

Niobium monoxide exhibits Pauli paramagnetism, has a small
composition dependent thermoelectric power, and a small negative Hall
constant.

The niobium-oxygen phase diagram about the equiatomic region has
a homogeneity range from 0.980 to 1.020 ± 0.002 oxygen/niobium molar
ratio. A congruent melting point is found at an O/Nb ratio of 1.006 ±
0.002. These limits were determined by precise lattice parameter
measurements utilizing a symmetrical back reflection X-ray focusing

camera. All compositions were determined by combustion analysis on one to two gram samples.

The specular reflectivity was determined to 12 eV at room temperature and the real and imaginary parts of the dielectric constant were calculated by a Kramers-Kronig analysis. The loss function and the number of optically active electrons was also calculated. Single particle excitations were assumed to account for the peaks in the imaginary part of the dielectric constant and were used to set a relative scale of energy on a proposed one-electron energy band scheme. A Slater-Koster L. C. A. O. calculation was performed for the $\langle 100 \rangle$ direction in the simple cubic Brillouin Zone of NbO. This calculation indicated that a splitting of the niobium t_{2g} orbitals occurs.

Spin-orbit splitting and trap-mediated bonding were demonstrated to have the proper effects necessary for the stabilization of the NbO structure. The resulting energy band scheme has localized trap levels which remove electrons from the lower part of the split niobium t_{2g} band.

Magnetoresistance in several directions was determined as a function of field strength as well as at a constant field strength as a function of crystal orientation. With the current in the $\langle 100 \rangle$ direction, the transverse magnetoresistance exhibited maxima in the $\langle 100 \rangle$ and minima in the $\langle 011 \rangle$ directions. The most interesting property found was the apparent magnetic breakdown at about 20 kOe in the $[\langle 100 \rangle, \langle 010 \rangle]$ configuration.

Niobium monoxide was found to react with most crucible materials; only tungsten was able to contain it when molten, although nearly one percent tungsten was found to be in solution in the melt. The reactivity of niobium monoxide necessitated the development of a new crystal growing technique utilizing the molten puddle of material obtained in an arc-melter. The device for crystal growth, the Tri-Arc Czochralski Furnace,© its construction and operation is described. The versatility

of the new technique was demonstrated by the growth of seven different crystals in one working day, from tin (melting point 230°C) to titanium carbide (3150°C).

Thesis Supervisor: Harry C. Gatos

             Title: Professor of Electronic Materials

TABLE OF CONTENTS

LIST OF ILLUSTRATIONS AND FIGURES

LIST OF ILLUSTRATIONS AND FIGURES (continued)

LIST OF ILLUSTRATIONS AND FIGURES (continued)

LIST OF ILLUSTRATIONS AND FIGURES (continued)

LIST OF ILLUSTRATIONS AND FIGURES (continued)

LIST OF TABLES

ACKNOWLEDGEMENTS

ELECTRONIC PROPERTIES OF NIOBIUM MONOXIDE

I. INTRODUCTION

A. Preface to the Transition Metal Compounds

The transition metal (TM) oxides differ from the carbides and nitrides
in that the oxides tend to have d electron bands in the relatively large
gap (5 to 10 eV) between the valence and conduction bands.[1] The
increase in electro-negativity difference in going from the carbides to
the nitrides, to the oxides causes the outer 2s, 2p electrons of the
oxygen anion (X) to be lower in potential energy with respect to the
outer d, s and p electrons of a TM atom. In the carbides and in most
nitrides the TM d, sp levels and the X p levels will lie in about the
same energy range and so will be involved in a high degree of admixture
leading to large overlapping X p, TM d and TM s bands. In the transi-
tion metal oxides, the oxygen s and p levels are well separated from
the TM d, sp levels and so the d levels tend to go into isolated, narrow
energy bands. This situation then enables one to concentrate on the
characteristics of the d band electrons and by suitable experiments,
determine their collective vs localized behavior.

Three members of the transition metal oxide family which are of
particular interest theoretically are titanium monoxide, vanadium mon-
oxide, and niobium monoxide. These oxides are the only stable mon-
oxides in the group IV, V, and VI transition metals. They are

structurally based on the rocksalt lattice but contain from 15 to 25 percent vacancies on each sublattice. The vacancies in titanium monoxide (15 percent vacancies) and vanadium monoxide (16 to 18 percent vacancies) can be ordered by a suitable heat treatment,[2,3] while niobium monoxide has 25 percent vacancies on each sublattice and remains an ordered, stable configuration at all temperatures. TiO is known to be metallic [2] and to have a superconducting transition temperature around one degree.[4] It is known that oxygen rich compositions of vanadium monoxide (O/V molar ratio > 1) are antiferromagnetic with Néel temperatures below $10°K$[5] and that they have positive Seebeck coefficients at $300°K$.[6] As for NbO, only its structure had been definitely determined, although Meissner in 1932[7] using sintered rods of "NbO" reported the possibility of a superconducting transition at about $1.4°K$. Krebs[8] believed that in NbO there should be pronounced antiferromagnetism and an enhanced bonding resulting from resonance coupling (so-called superexchange[9]) between two next-nearest neighbor niobium t_{2g} orbitals through an intermediary oxygen p orbital (a cation-anion-cation interaction[1]).

B.   Bonding in the Transition Metal Rocksalt Compounds

The sodium chloride lattice seen in most transition metal

monocarbides, nitrides and oxides, consists of two overlapping

face-centered cubic sublattices.   Each metallic atom (TM) is surrounded

octahedrally by six nonmetallic (X) atoms and vice versa.   The large

increase often seen in the melting point and the hardness, as well

as the extreme brittleness, in the transition from pure metal to the

compound formation point to a strong TM-X bonding, presumably,

some part of which is ionic.   However, most of these compounds also

possess metallic conductivity, are weakly paramagnetic and are

generally superconductors.   The transition metal rocksalt compounds

usually have a metallic appearance, similar to silver or gold.   The

metallic-like properties indicate a propensity for TM-TM atomic

wave function overlap typically seen in the transition metals themselves.

Thus, it is understandable that although bonding in the transition metal

rocksalt compounds has been considered by a number of investigators,

few have come to assenting conclusions.

Rundle [10] was the first to undertake a study of these compounds.

Based on the observation of the high hardness and brittleness yet good

conductivity and metallic luster, Rundle concluded that the dominating

influence in these compounds was the TM-X interaction resulting in a

homopolar character of the bonding.   The homopolar nature was due

to p-type electrons or to s-p hybridized functions on the anions forming

bonds of 1/2 or 2/3 bond number respectively (in the fashion of Pauling [11]) with the adjacent cations. Rundle classified the known TM rocksalt compounds into 1/2 and 2/3 bond number groups according to the metal-metal interatomic distance and the total number of electrons available for bonding. The bond order 2/3 was preponderantly associated with the carbides whereas 1/2 tended to be coupled with the nitrides. Hume-Rothery [12] supported the association of the bonding numbers 1/2 and 2/3 with the nitrides and carbides by the argument that a nitrogen atom requires three electrons to fill its 2p shell, i.e. in every case 1/2 from each of its six TM neighbors, whereas a carbon atom requires correspondingly 2/3 electrons. One should thus expect the oxides to have a bond order of 1/3. This simple scheme fitted some compounds nicely but generally there was no real correlation to the TM-TM distances and the fractional bond order. (Although vacancies were not considered in Rundle's work, they are not sufficient to bring the number of electrons in line with Pauling's empirical distance-bond order relation [12].) Rundle does point out, however, that the instability of the rocksalt structure for the VIth group and higher carbides and nitrides must be due to the increase in the number of electrons available for metal-metal bonding thereby tending to decrease the TM-TM distance and forcing the structure to hexagonal.

Krebs [8] expanded upon Rundle's work on the homopolar nature

of the bonding while considering the stability of the rocksalt TM

compounds, basing his study on the resonance coupling of orbitals,

in particular, the π-bond resonance of metal d-t$_{2g}$ orbitals and

nonmetal p orbitals. The transition metal d-t$_{2g}$ orbitals are particularly

suited for metal-metal bonding in the rocksalt structure as the lobes

of the orbitals are directed towards one another from the respective

metal sites. However, Krebs states that the enhanced bonding that

should result from the resonating π-bond between an oxygen p electron

(say with spin up) in the appropriate p-orbital with first one near

neighbor TM d-t$_{2g}$ orbital with a d-electron (spin down) and then the

TM neighbor (spin up) on the opposite side of the oxygen, outweighs

that anticipated from direct TM-TM bonding. At each point in the

resonance, one has an electron pair bond of opposite spins located on

one of the d-t$_{2g}$ orbitals. According to Krebs, most of the rocksalt

TM compounds (including NbO) should show antiferromagnetism due

to the resonance coupling.

In contrast to the TM-X interaction as the dominant influence

in bonding, Costa and Conte [13], Dempsey [14], Kiessling [15],

and Robins [16] proposed the TM-TM interaction as leading to the

strongest bonding. These investigators were primarily concerned

with the carbides and nitrides of the rocksalt compound group. A

major assumption that was made in these studies was that the anion

p electrons were mixed into the cation d states with a subsequent

transfer of p electrons to the cations to aid in the filling of the d states. One of the more significant facts about the rocksalt TM compounds is that the transition metals of importance in forming these substances have in their free atoms, d shells containing relatively low numbers of electrons (not necessarily true for the oxides, for instance, NiO). The stability, based on the melting point, of the transition metals has been shown to increase towards the middle of each series [12]. Dempsey [14], using the assumption that all of the metalloid p-electrons go into the TM d bands upon compound formation, found good correlations for the melting point, electrical resistivity, and magnetic susceptibility of the transition metal (diborides, carbides, and nitrides) compounds as compared with the transition metals.

While charge transfer from anion to transition metal may occur for the carbides due to the mixing of anion p levels with the cation d levels, it is less likely to occur for the nitrides and especially the oxides. Evidence justifying Dempsey's assumption is conflicting. Surovoi, Shvartzman and Alekseev [17] conclude, from a study of heats of atomization, that C^{2+} ions are present in the monocarbides. On the other hand, measurement of the electron diffracting power in Mo_2C by Nagakura, Kikuchi and Oketani [18] led to the assumption of the existence of C^{-1} ions in the lattice indicating at least partial transfer of electrons from Mo d states to the C p states. From X-ray emission

and absorption spectra of chromium refractory compounds,

Menshikov and Nemnonov [19] conclude that charge transfer, if it

takes place, is to the Cr d bands. Fischer and Baun [20] as well

as Holliday [21] have investigated the soft X-ray emission bands in

some refractory borides, carbides and nitrides and concluded that

there was little if any charge transfer from X to TM atoms.

A semi-quantitative calculation by Bilz [22] using a simplified

Linear Combination of Atomic Orbitals (L. C. A. O.) method (see

for instance Slater and Koster [23]), on a TM_6X molecular unit led

to the conclusion that besides TM-X bonding, a definite TM-TM

bonding also should be considered. One TM_6X molecule was isolated

from the crystal and examined for the one TM ligand, of the six valence

functions which were obtained through sp^3d^2 hybridization, that was

directed toward the central X atom. This orbital was almost entirely

localized in that direction. A nearly self-complete complex of

molecular functions within an TM_6X group was obtained which barely

extended beyond its edge. Metal-metal interactions were brought into

the model through consideration of the remaining d functions (the t_{2g}

functions) acting to couple the molecular units together. The influence

of the TM-TM interaction was to make an overlapping band structure

probable. Without the TM-TM interaction the bands would tend to

be isolated and narrow.

Bilz considered the TM-d and s orbitals with the X-p functions (i. e. nine atomic functions altogether) in the Slater-Koster scheme, obtaining values for the various two-center integrals from other work on nickel [24] and copper [25] and on NaCl [26] and LiF [27].

Calculations were performed in the three principal directions $\langle 100 \rangle$, $\langle 110 \rangle$, $\langle 111 \rangle$ and a density of states curve was qualitatively estimated (Figure 1). Included in this figure are the Fermi levels to which various compounds would be considered to fill. The density of states curve derived by Bilz exhibits a similarity to that obtainable from an interpolation between TM-TM and TM-X only bonding (broad overlapping bands versus narrow localized bands respectively). The essential characteristic of the density of states shown in Figure 1 is a broad s-band with a low density of states overlapping narrow d-bands of high state density.

A more quantitative calculation of the energy bands in rocksalt TM compounds was performed by Ern and Switendick [28] on TiC, TiN, and TiO using the Augmented Plane Waves (APW) method. The density of states curves resulting from the APW calculations are shown in Figure 2 . Although these state density curves are similar to that derived by Bilz, the decrease in mixing of anion p states with the titanium d states as one progresses from the carbide to the oxide is evident. It appears that across this series of compounds there is an increasing proportion of ionicity that is to be considered while

maintaining definitive metallic-like bonding.

With either of these last two approaches to the study of the TM rocksalt compounds, investigators such as Piper [29] have been able to fit experimentally observed quantities (such as soft X-ray emission energies, specular color of a material, or high versus low temperature superconductivity) to the calculated band structures. Either of these two calculations then should provide an invaluable starting point in the qualitative understanding of numerous compounds in the TM rocksalt group.

What has been seen then is that the coincidence of high-temperature strength and metallic electrical conductivity suggests an admixture of covalent (homopolar) bonding and metallic bonding, although the simple application of these models has led to apparently antithetical explanations of material properties. In this class of refractory compounds, there must exist combinations of all the types of bonding that have been considered and so one should be able to find systematic variations in the relative strengths of the bonding types. For example, whenever the difference in electronegativity between cation and anion is large, the bonds should exhibit a significant ionic (heteropolar) component and in fact, it should be permissable to assume that although different kinds of bonding may be operative, there will be a continuous transition from one dominant bond type to another in some given series of compounds. This situation is quite analogous to that encountered in the modern theory of alloys.

C. Niobium Monoxide Crystal Structure

The crystal structure of niobium monoxide was first investigated by Brauer[29] in 1941 and later by Andersson[30] in 1955. The basic cell consists of three atoms each of niobium and oxygen arranged on the face centered sites of two superimposed simple cubic lattices but with the origin site being vacant on both sublattices. It can be considered as a defective NaCl lattice with the Na type (000) and Cl type $\left(\frac{1}{2}\frac{1}{2}\frac{1}{2}\right)$ sites vacant. The remaining sites $\left(\frac{1}{2}\frac{1}{2}\frac{1}{2}\right)$ and $\left(\frac{1}{2}\,00\right)$ can be considered as occupied by niobium atoms only and oxygen atoms only, respectively (Figure 3). This particular order results in an overall simple cubic structure with an ambiguous definition of its space group, O_h^1, T_d^1, O^1, or T_h^1. The group O_h^1 was chosen because it is the one containing the highest degree of symmetry.

The early work on the structure of NbO was accomplished by X-ray analysis using film techniques and as such did not give a completely unambiguous measure of the location of oxygen atoms on the various sites. Approximately, equally good fits to the relative intensities of the NbO powder patterns were obtained for the niobium atoms ordered on one type site only with the oxygen atoms either ordered or distributed at random on the other type sites. The oxygen atoms have a small X-ray scattering factor compared to that of niobium and so contribute only a small portion to the diffracted intensity. Within the accuracy of the measurements, one could not truly tell if the oxygen atoms were ordered. It was considered highly probable that the resulting oxygen vacancies were ordered

since the niobium atoms were apparently ordered. The recent work of

Bowman et al[31] (1966) at Los Alamos using neutron diffraction gave

convincing proof that the oxygen atoms were indeed ordered in the same

fashion as the niobium atoms.

Figure 4 shows the Brillouin zone for the simple cubic structure

of niobium monoxide, the symmetry points are labeled according to the

notation of Bouckaert, Smoluchowski, and Wigner.[32]

D. Reasons for the Investigation of Niobium Monoxide

The present investigation on niobium monoxide was initiated because of its many interesting apparent properties such as:

(1) a large vacancy content; the largest of any structure if NbO is considered to be a rocksalt type compound.

(2) totally ordered vacancy concentration to its melting point in contrast to TiO and VO.

(3) the possible occurrance of superconductivity.

(4) the possibility of antiferromagnetism, which when considered with superconductivity would make NbO a unique compound.

(5) an apparently narrow homogeneity range which is in direct contrast to all of the other transition metal carbides, nitrides and monoxides; for example, TiO and VO are stable over the compositional range of about 0.8 to 1.25 O/TM molar ratio while NbO is limited to 0.98 to 1.02.[33]

(6) its cubic structure when the ordered vacancies should lead to a tetragonal or other distortion (Figure 3), such as occurs in TiO when the vacancies order at low temperature (a monoclinic unit cell results[34]).
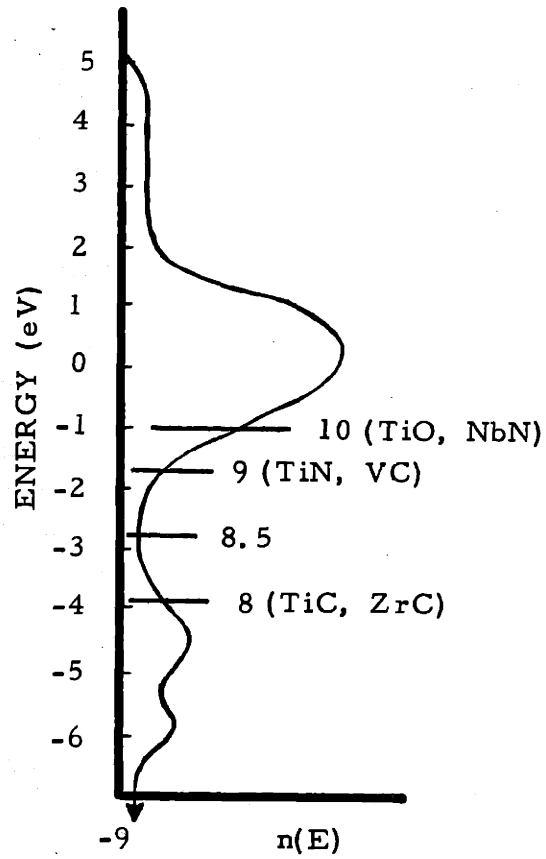
Figure 1   Tight Binding Calculation of the Density of States
for a General Transition Metal Rocksalt Compound
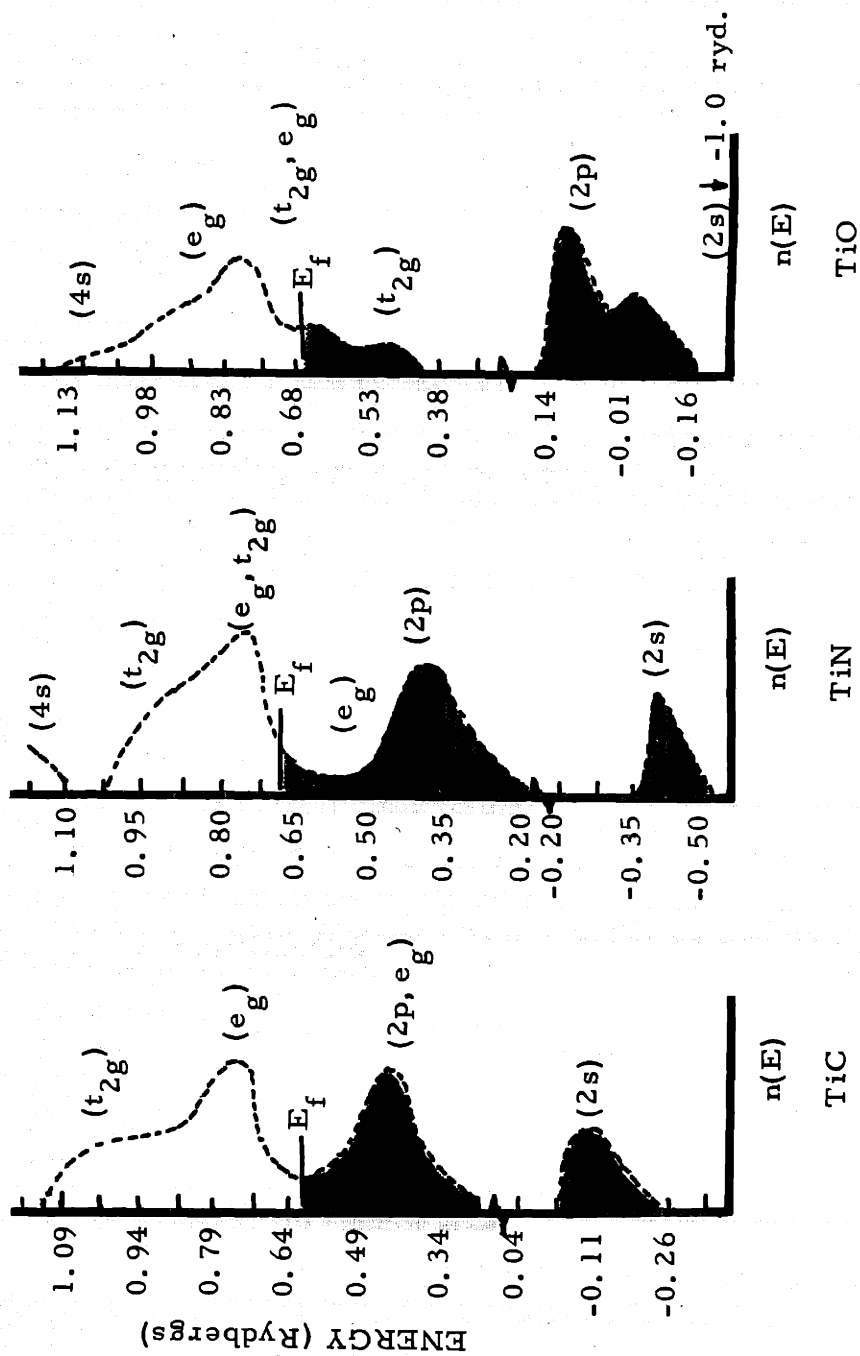
Figure 2   Augmented Plane Waves Calculation of the Density of States for Titanium Carbide, Titanium Nitride and Titanium Oxide
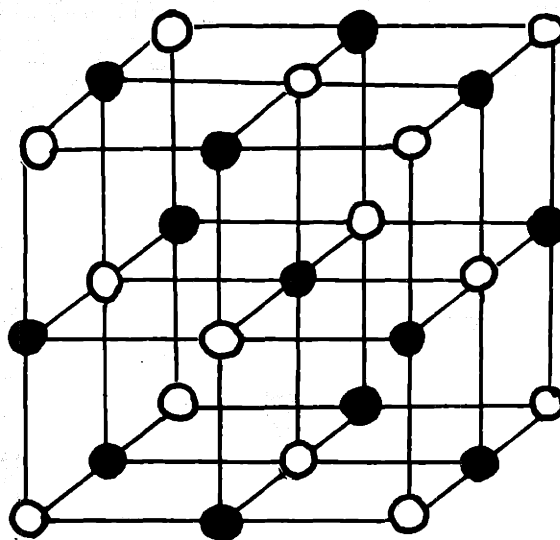
SODIUM CHLORIDE
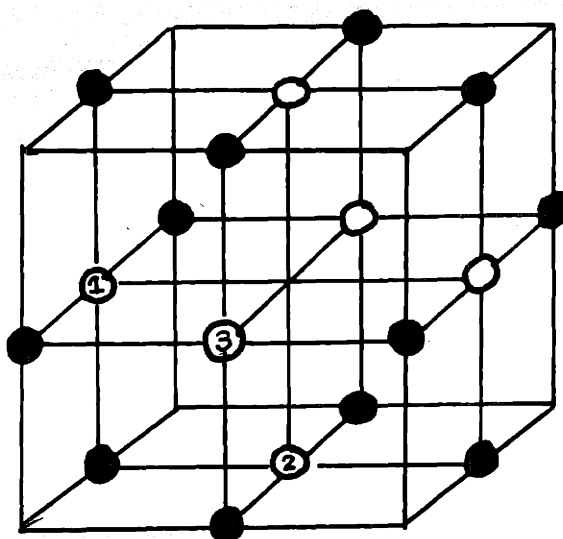
NIOBIUM MONOXIDE

Figure 3   Comparison of Rocksalt (NaCl) and the Niobium
Monoxide Structures
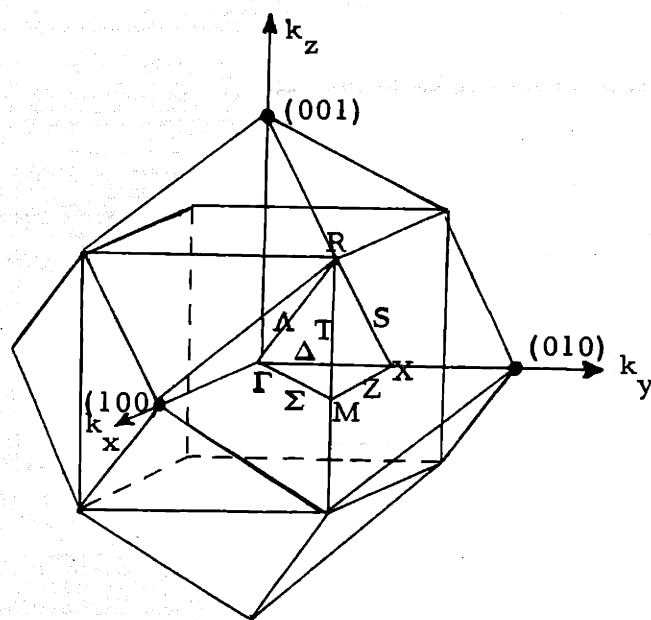
Figure 4 First and Second Brillouin Zones for a Simple Cubic Lattice

II. OUTLINE AND PLAN OF WORK

The objective of the present investigation is to examine in detail the electrical and magnetic properties resulting from the apparently, highly defected structure of niobium monoxide.   The general method of approach may be summarized as follows.

First, techniques for the growth of niobium monoxide single crystals must be investigated or, if none are available, developed. Single crystals of good purity are essential to any study into the solid state properties of a material.

Secondly, measurements of such properties as the electrical resistivity, the magnetic susceptibility, the Hall effect and the thermoelectric power as well as optical reflectivity are required for the understanding of the characteristics of a material. It should be possible to compare these results with existing theories or any modifications of such theories which may be developed.

Thirdly, since the niobium monoxide structure contains an extremely high, ordered, vacancy content, as much information on the band structure as is possible should be collected with the aim of understanding the stability of such a compound in comparison with other members of the large transition metal rocksalt compound family.

III.   MATERIALS PREPARATION AND EXPERIMENTAL PROCEDURES

A.   Development of the Tri-Arc Czochralski Furnace

Early attempts to prepare niobium monoxide single crystals were largely unsuccessful. The growth of niobium monoxide from the melt is extremely difficult due to its reactivity with most container materials. Seamless welded tungsten crucibles were used by Reed and Fahey[35] to grow NbO crystals in a resistance-heated furnace, but the resulting crystals contained 1 to 2 percent tungsten. A new approach was obviously necessary to obtain pure single crystals of niobium monoxide. It was decided to investigate the possible use of the "cold hearth" (or arc melting) phenomenon, as a technique for single crystal growth.

In arc melting, a charge of material that is to be melted is placed on a water cooled hearth acting as an anode. An electrode, generally tungsten, is touched to the hearth initiating an electric arc. The arc is then played over the charge melting it, and resulting in a molten pool sitting on the cooled hearth. Power is conveniently supplied by a D. C. arc welder. The hearth and electrode are contained in a chamber with an argon or other inert gaseous atmosphere. The atmosphere provides a conduction path for the arc as well as protection for the molten material.

The bottom of an arc-melted 'button' of most materials typically showed a highly puckered surface indicating that the molten sample was not totally in contact with the hearth, but rather was supported by a

stilt-like network with surface tension maintaining the molten charge in an overall button shape. As more heat was supplied to the melt, more point contacts were required as supports. Thus the melt apparently was maintained in a skull of non-molten material, acting as its own crucible. It appears that across this skull, temperature gradients of the order of 200,000°C/cm obtain. Utilization of this skull melting technique avoids the problems of crucible containment and sample contamination. Mass spectrometric analysis typically shows no copper or tungsten contamination (at the 5 ppm level) in the arc-melted button.

1. Introduction to Arc Melting

(a) Brief History of the Electric Arc

The electric arc was first described by Davy[36] in 1809, but was not used for the preparation of materials until 1839 when Hare[37] using a cold hearth melted Platinum, Phosphorous and Calcium and synthesized CaC_2. Other early researchers such as Moissan[38] (1897) worked mainly with carbon electrodes in air or carbon monoxide atmospheres attaining temperatures up to 4000°C. The use of the arc melter was restricted primarily because of such atmospheres and the limitations on the understanding of the nature of the arc and its associated plasma. The Moissan type furnace is still in use for synthesis and growth of some refractory materials such as MgO.

Interest in the arc melter as a laboratory tool increased with the rising interest in aluminum technology in the 1930s, and the accompanying increase in availability of argon and helium. Kroll[39] in 1940 described an inert gas arc melting furnace, using a water cooled hearth and tungsten electrodes, for processing refractory metals in inert atmospheres. Various electric arc techniques are reported in detail by Sheer and Korman.[40]

(b) Physical Description of the Arc

An arc is defined generally as the small volume of plasma heated by the passage of charge between two electrodes. The simplest method of producing such a heated plasma is to pass a large direct

current between two electrodes. Arcs have been operated at current levels below one ampere and above one million amperes. But general laboratory operations occur between ten and one thousand amperes. The temperature in the body of the plasma ranges from 10,000 to 30,000°K: the lower limit is set by the temperature required for ionization and an appreciable conduction to occur, the upper limit is determined by available power densities.

An important part of the arc is the high velocity ($\sim 6 \times 10^4$ cm/sec) magnetohydrodynamic (MHD) electrode flame issuing from the cathode tip as the result of the high current density there. The high current density at the cathode tip, which is an order of magnitude larger than in the body of the plasma, creates a magnetic pinch field causing the plasma to stream away from such a region. This electrode flame is particularly important in the melting of non-conductors.

In melting conductors, the principle heating mechanism, with heat intensities up to 10 KW/cm^2, is the condensation of electrons at the anode yielding five to twenty watts/ampere. In a typical arc configuration, approximately 90 percent of the total arc energy is delivered to the anode by the two mechanisms, electron condensation and MHD flame.[41]

Thoriated tungsten is a generally used electrode as it has a low work function and is readily available because of its use in welding.

(c) Power Requirements

Since a plasma does not have a fixed resistance or voltage

drop, certain relationships must obtain due to the static and dynamic

interactions between the plasma and its power source. The electric arc

operates approximately at a fixed voltage. At low currents the voltage

falls with increasing current, and at higher currents it starts to rise

with current, but the potential typically will change by less than a factor

of two while the current changes by one order of magnitude. Thus, a

constant voltage source such as a battery would be unsuitable for a stable

arc, as a small change in the arc length leads to a very large current

change. A suitable power source to provide a stable arc would be one

having a falling I-V characteristic, i. e. a negative resistance region.

Figure 5 shows the variation with current of arc voltage, total arc

power, and thermal power transferred to the anode for a typical arc

operating in argon.[42] For arc stability it is necessary for the

characteristic voltage-current curve of the power supply to intersect

the arc characteristic curve at a steep angle, as is shown in the figure.

A battery could be used as a power source but only with a large

ballast resistance in series. This arrangement is satisfactory up to

50 amperes, but the majority of the voltage drop occurs across the

ballast.

Commercially available D. C. welding rectifier power units

are inexpensive and give excellent results. Stabilization is achieved by

a reactance in the A. C. part of the rectifier circuit, and approximately 95 percent of the total power is transferred to the arc. The units are characterized by an open circuit voltage (at least twice the operating voltage), and a short circuit maximum current so that they can be short circuited without damage during arc initiation.

(d) Atmosphere

Argon at a slightly positive pressure is used in most arc melting operations, although helium, nitrogen, and argon-hydrogen mixtures may be used. When using an oxidizing or carburizing atmosphere, electrodes other than tungsten must be used. Carbon electrodes have been used with some success although they are consumed in oxidizing atmospheres. Zirconium electrodes which may become protectively coated with a thin layer of zirconia have also been used. Most commerical gas cylinders contain oxygen or water vapor contaminants which form volatile tungsten oxides, usually seen as a white smoke issuing from the tungsten electrodes. Commerical welding argon contains 5 to 50 ppm oxygen which is fairly satisfactory for operation but occasionally a black deposit will form on the anode.

The arc operates well at pressures above about 100 torr; at lower pressures the cathode heat balance changes and the MHD forces are not effective in stiffening the arc, so the arc tends to wander.
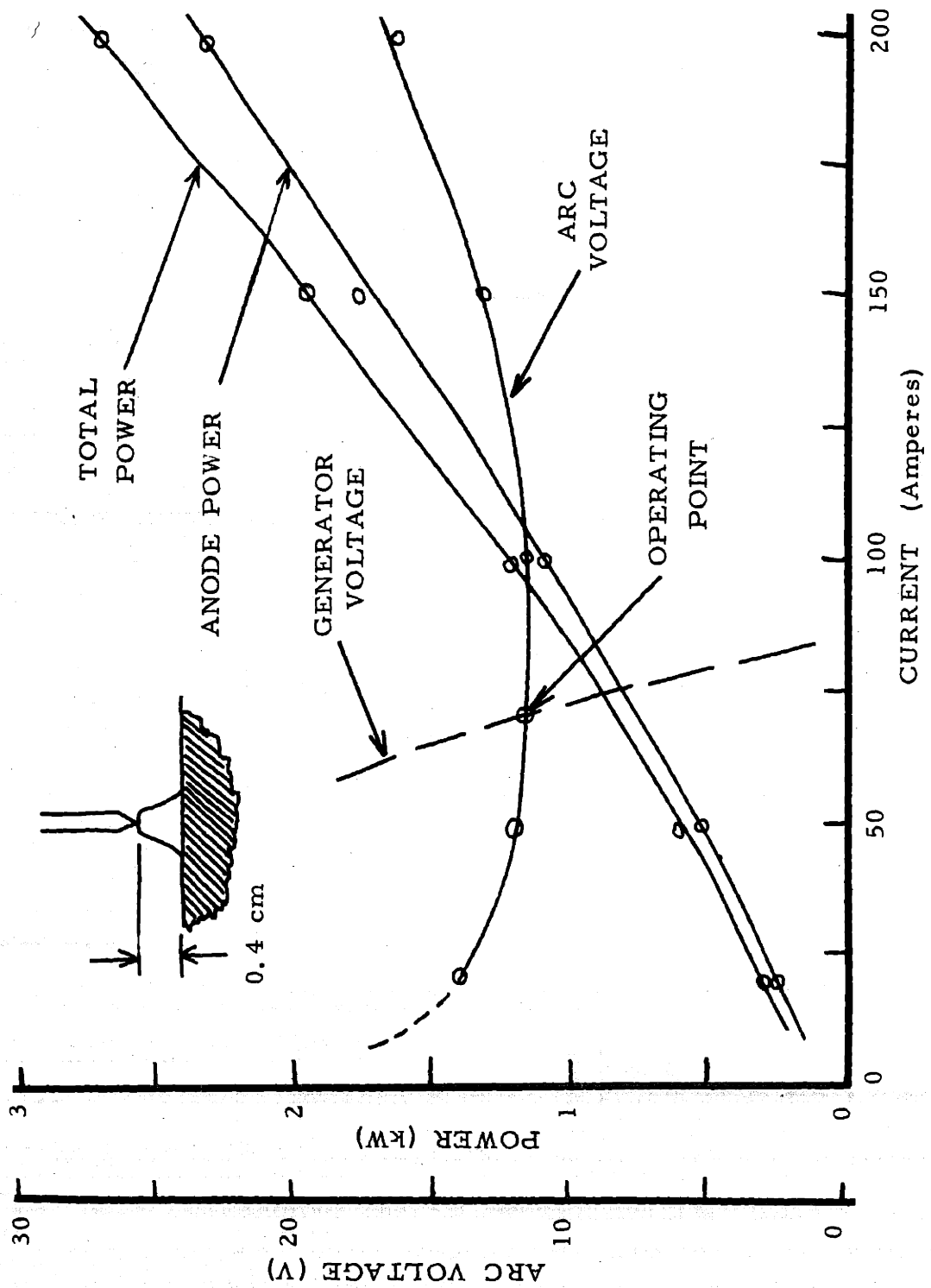
Figure 5 Current - Voltage Characteristics for an 0.4 cm Arc

2. / Physical Description of the Tri-Arc Furnace

The molten 'puddle' that occurs during arc melting, should be suitable for the growth of crystals under proper conditions. With this in mind, a conventional commercial arc melter was modified by the addition of an electrically insulated water-cooled seed holder. The holder was located off-center over one of the hearth insets. A rotator-pulling mechanism was attached at the top of the arc melter and several small crystals were grown. The major problems with this single arc technique were the instability of the molten area and the inability to maintain a stable crystal-melt interface.

The arc-melting furnace constructed for Czochralski-type growth is shown in Figures 6 and 7 . The melt instability found in the single electrode unit is solved by the use of three cathodes to heat the periphery of the melt (Figures 8 and 9). The melt is supported by a water cooled copper crucible. The furnace consists of an upper cathode member and a lower anode member, which are insulated from each other by an annealed Pyrex ring resting on 'O' rings. Pyrex was chosen instead of quartz because Pyrex stops most of the UV radiation generated by the arcs. It is necessary to protect the eyes from the UV radiation. Welding goggles of optical density 8 - 10 are suitable, or a shield of the same material may be used in front of the furnace.

The upper member contains a central hole through which a water-cooled seed rod, mounted in a ball and socket, is raised or lowered by

a pulling mechanism. The pulling mechanism (Figure 10) is manually operated. It operates by rotating a hollow threaded shaft (A) concentric with a smaller hollow threaded shaft attached to a ball (B). At the top of the outer shaft is a press-fitted bearing and a recessed 'O' ring (C). Attached to the top of the bearing is a standard 3/8 inch "Swagelok" fitting containing an 'O' ring (D). When the fitting is tightened, rotation of the outer shaft raises or lowers the seed rod without rotation. At the end of the threaded track, which is about 2-1/2 inches long, the Swagelok is loosened allowing the puller shaft (A) to be returned to its starting position without disturbing the growing crystal. The inner shaft (B) has a tapered inside hole to allow the growing crystal (maximum diameter of included crystal is 1/2 inch) to be drawn up inside it. This could be adapted as a afterheater. The puller mechanism is easily adapted to automatic pulling by the attachment of a variable speed motor with an 'O' ring belt or gear drive mechanism (Figure 11). However, raising and lowering by hand enables one to maintain control over the dimension of the crystal - melt interface which may fluctuate during growth.

In the cathode head there are also six holes equally spaced around the circumference, three containing tungsten electrodes mounted in ball and 'O' ring sockets and three sealed with quartz windows (Figure 12). Water circulates in the electrode sockets providing electrical insulation as well as cooling. The current leads are attached to brass collars (G) that are threaded onto the copper body (H) of each electrode (Figure 13).

The lower member consists of a central graphite or copper piston (~ 2.5 cm in diameter) that can be raised or lowered manually utilizing an arrangement similar to that used for pulling (Figure 14). The feed piston (Figure 7 , part A) moves inside a copper cylinder (B) which is tapered to fit into a water-cooled brass cylinder (C) containing the gas ports and electrical grounding lead. The six gas ports exit tangentially to the brass cylinder from a distribution ring (D). This arrangement leads to turbulent flow of the chamber gas and aids in effective flushing. The small total volume of the furnace (about 200 cm^3) allows rapid initial purging. The gases used (typically argon) are passed through a purification furnace containing titanium strips and so trace oxygen and water vapor are effectively removed.

The Tri-Arc furnace is powered by a commercial 500 ampere D. C. welding generator. Each arc is stabilized independently by a variable ballast resistor (1/2 to 4 ohms) allowing electrode currents from 5 to 120 amperes.

An adaptation to the hearth is useful when melting or growing non-conductors or materials which are non-conducting until some elevated temperature. Three equi-spaced tungsten spikes are inserted into the top near the inside diameter of the tapered copper cylinder (part B of Figure 7 or part F of Figure 13). The spikes provide anchorage points for the arcs and are necessary because the power levels required for melting something like Al_2O_3 would erode the copper hearth. The

electrodes are screwed down until they are almost touching the material

so that heat is supplied to the material by the arc and its flame as it

streams to the anchoring spikes.
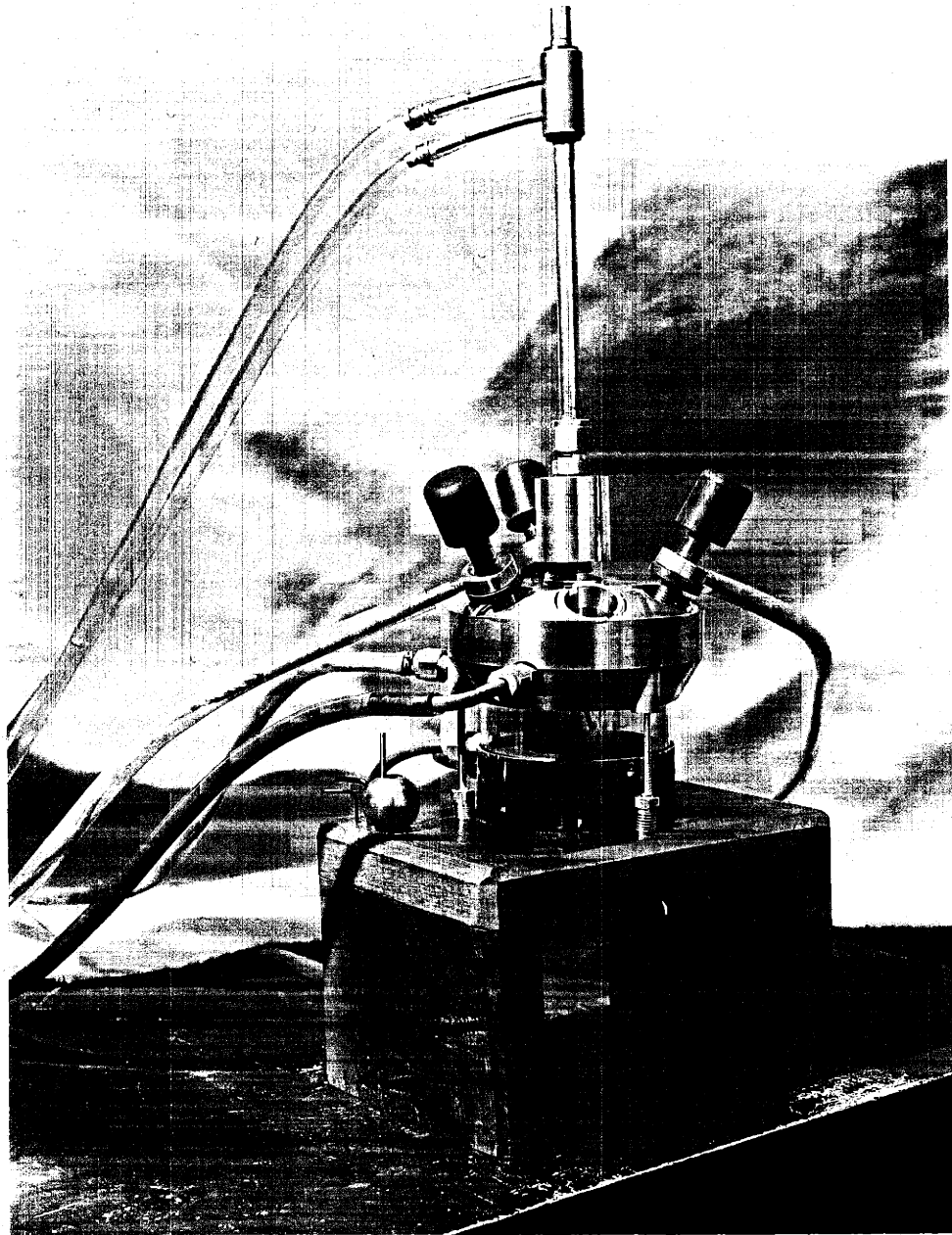
Figure 6   Photograph of initial Tri-Arc Czochralski Furnace with
            manual pulling mechanism.

CATHODE BODY

WINDOW

PULLING ROD

PYREX WINDOW

HEARTH

COOLING

STAND

CATHODE (−)

SEED

CRYSTAL D

C

B

A

(−)

PISTON

GAS

CURRENT LEAD

ANODE BODY (+)
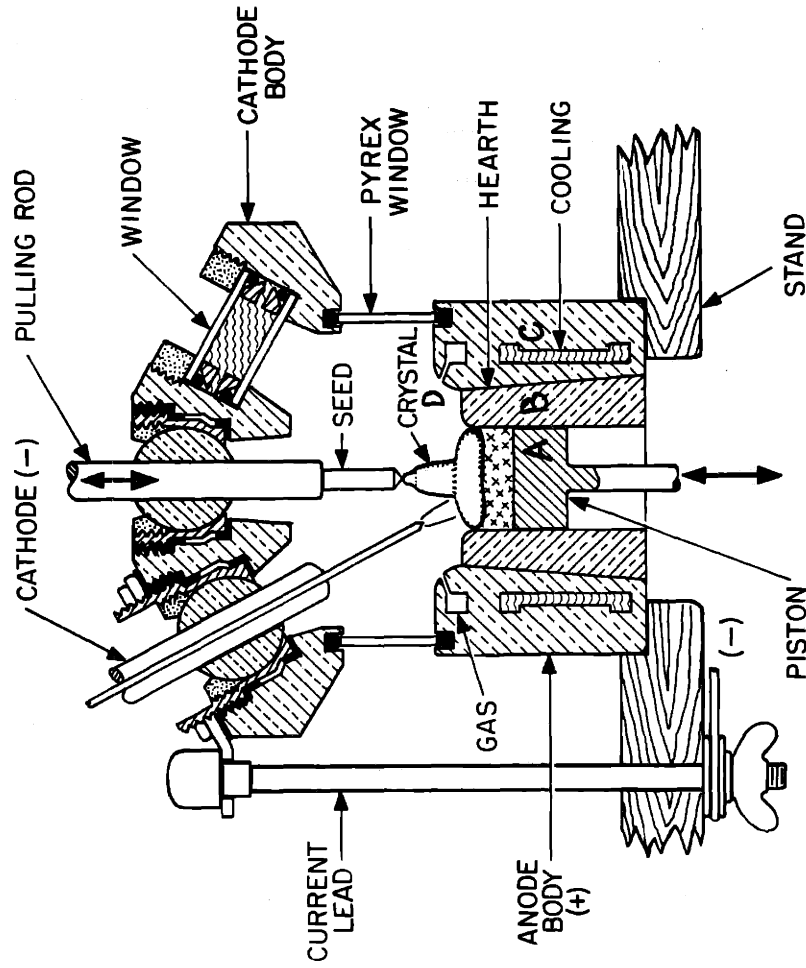
Figure 7   Schematic of the Tri-Arc Czochralski Furnace.

Figure 8   View through the Pyrex ring of the molten charge showing the three arcs.
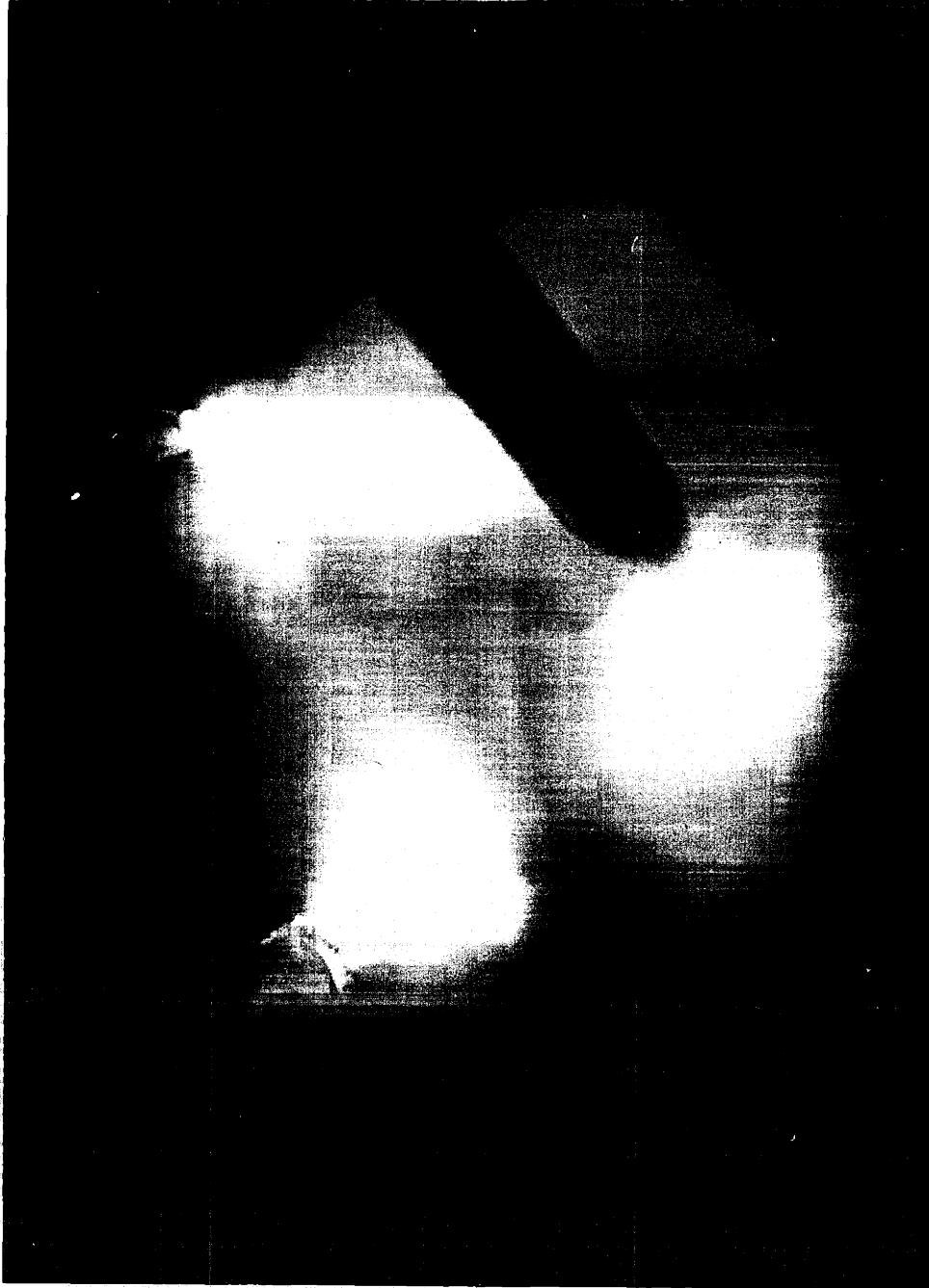
Figure 9 View through an upper quartz window showing the melt and the three arcs.

D, Swagelok Fitting

C, Press Fit Bearing

A, Elevator

B, Threaded Elevator
Shaft with
Attached Bronze
Ball
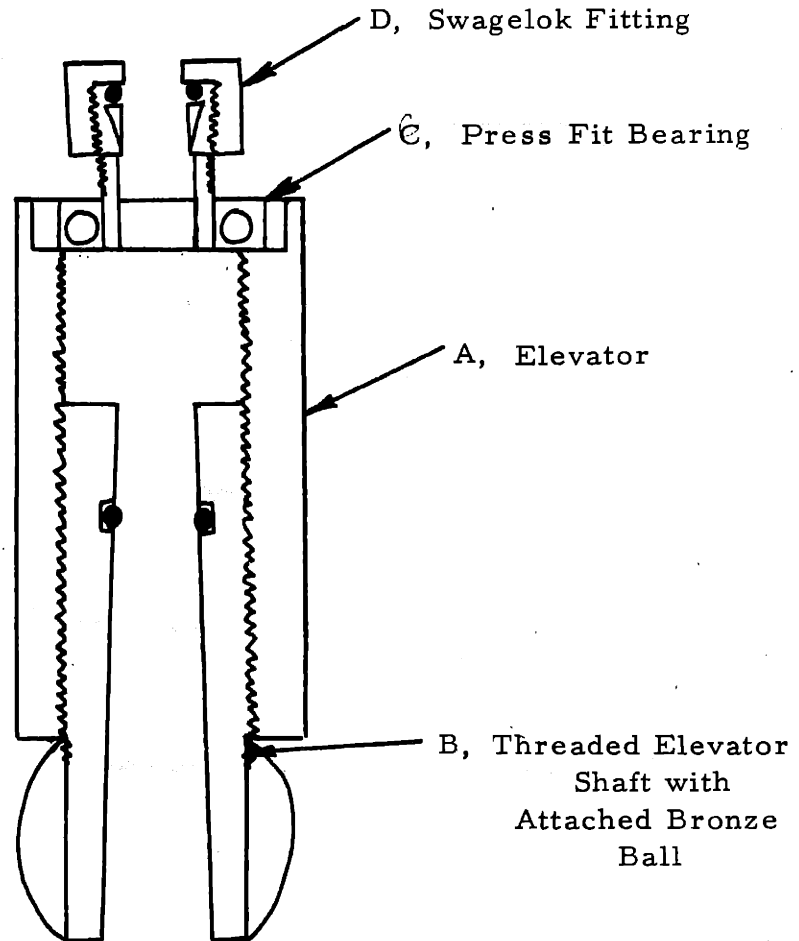
Figure 10 Manual crystal pulling mechanism
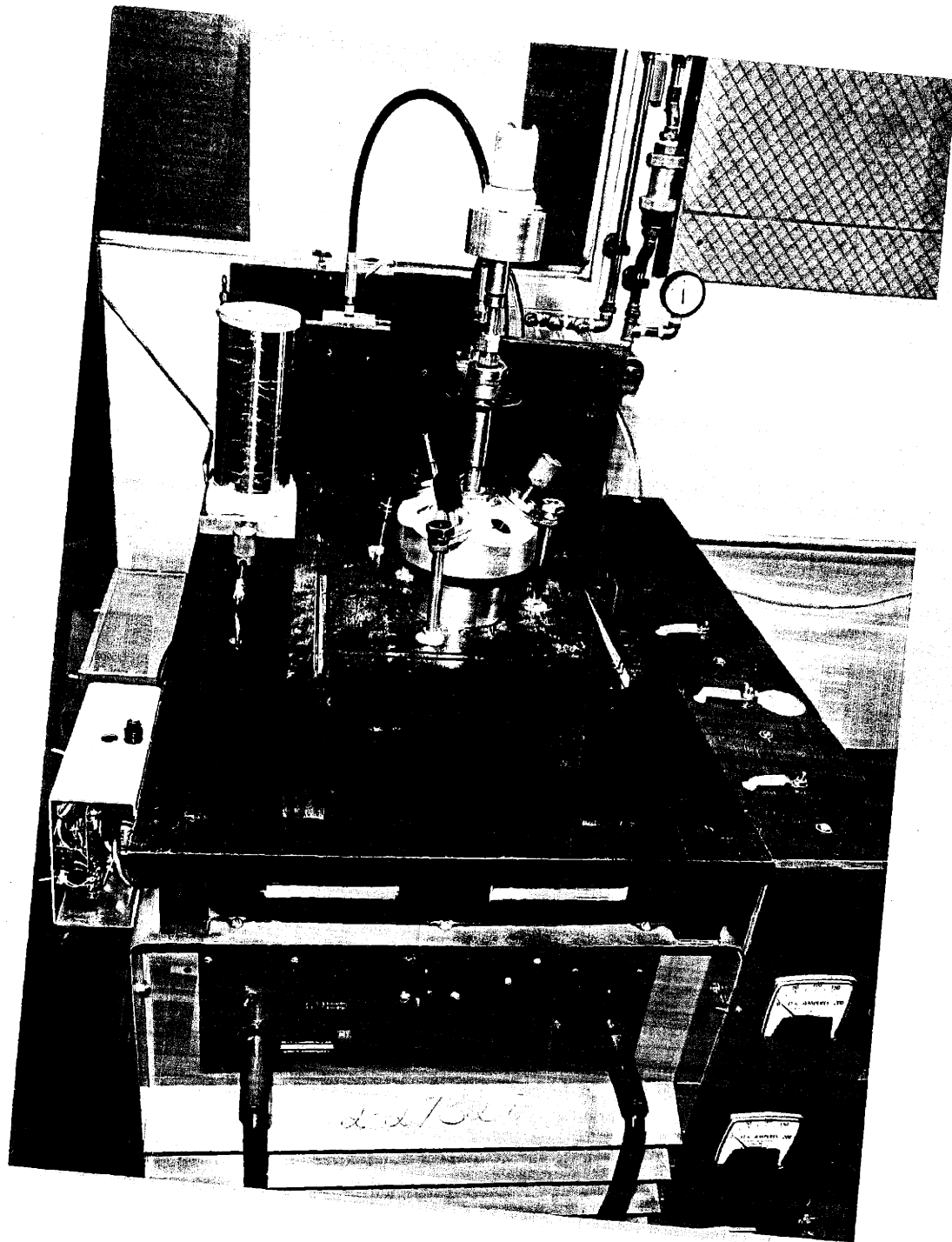
Figure 11   Recent stage in the development of the Tri-Arc Czochralski Furnace showing automatic rotation and pulling mechanism.
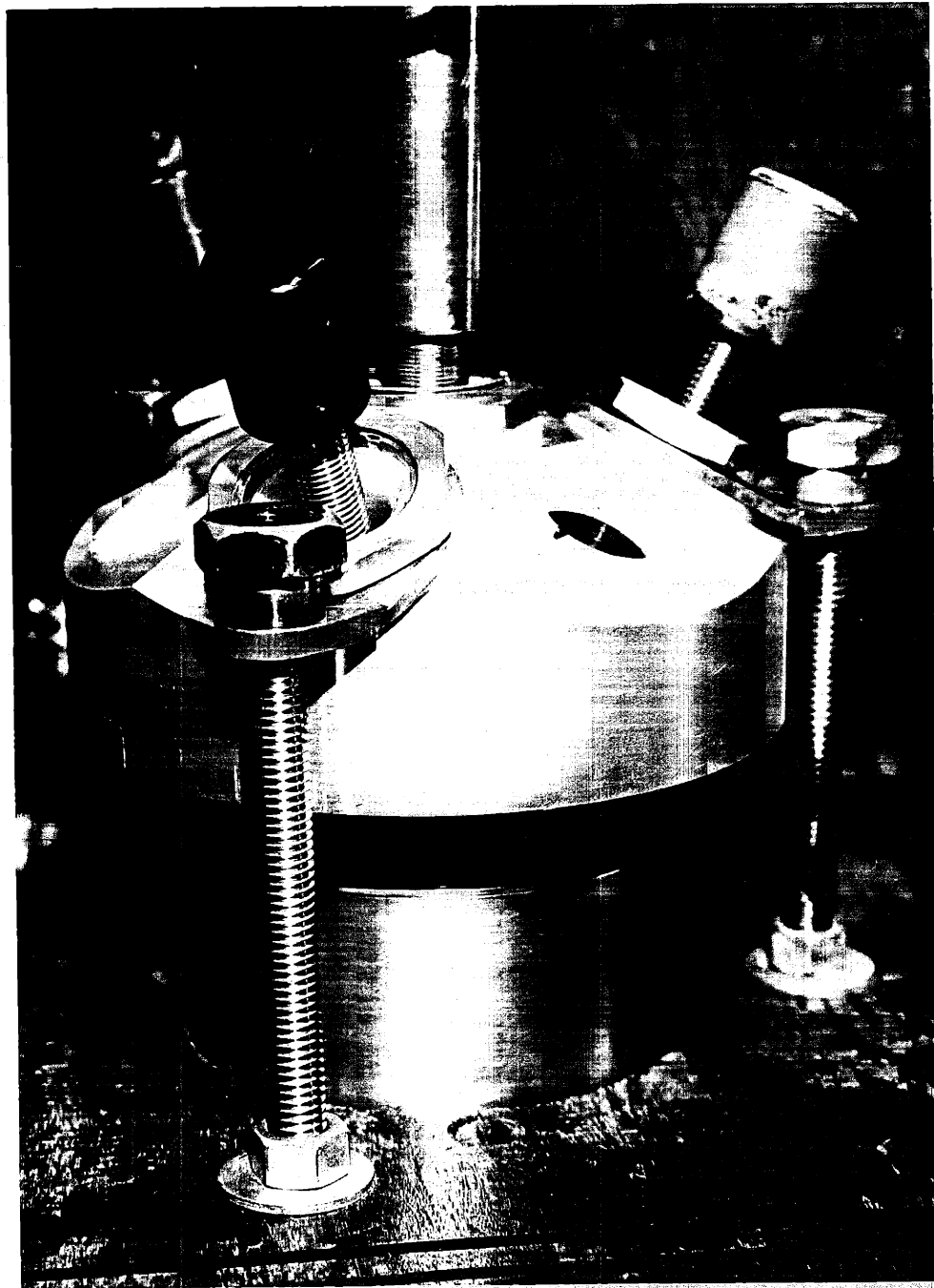
Figure 12   Upper view of the Tri-Arc Furnace showing the
electrode and window arrangement.
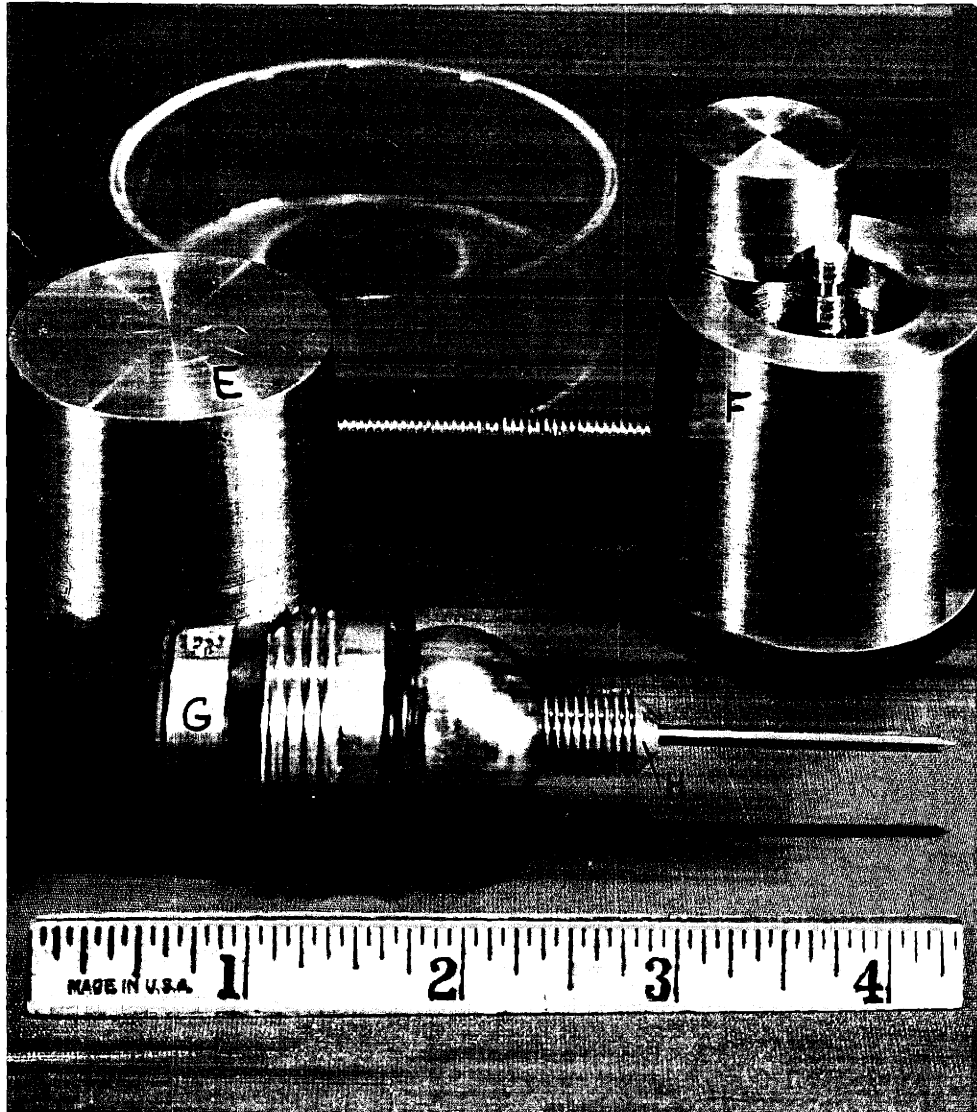
Figure 13 Electrode unit and various hearths used in the Tri-Arc
Furnace.

Feed Piston

Tapered
Copper Cylinder

Threaded Feed Post

Press Fit Shaft Bearing
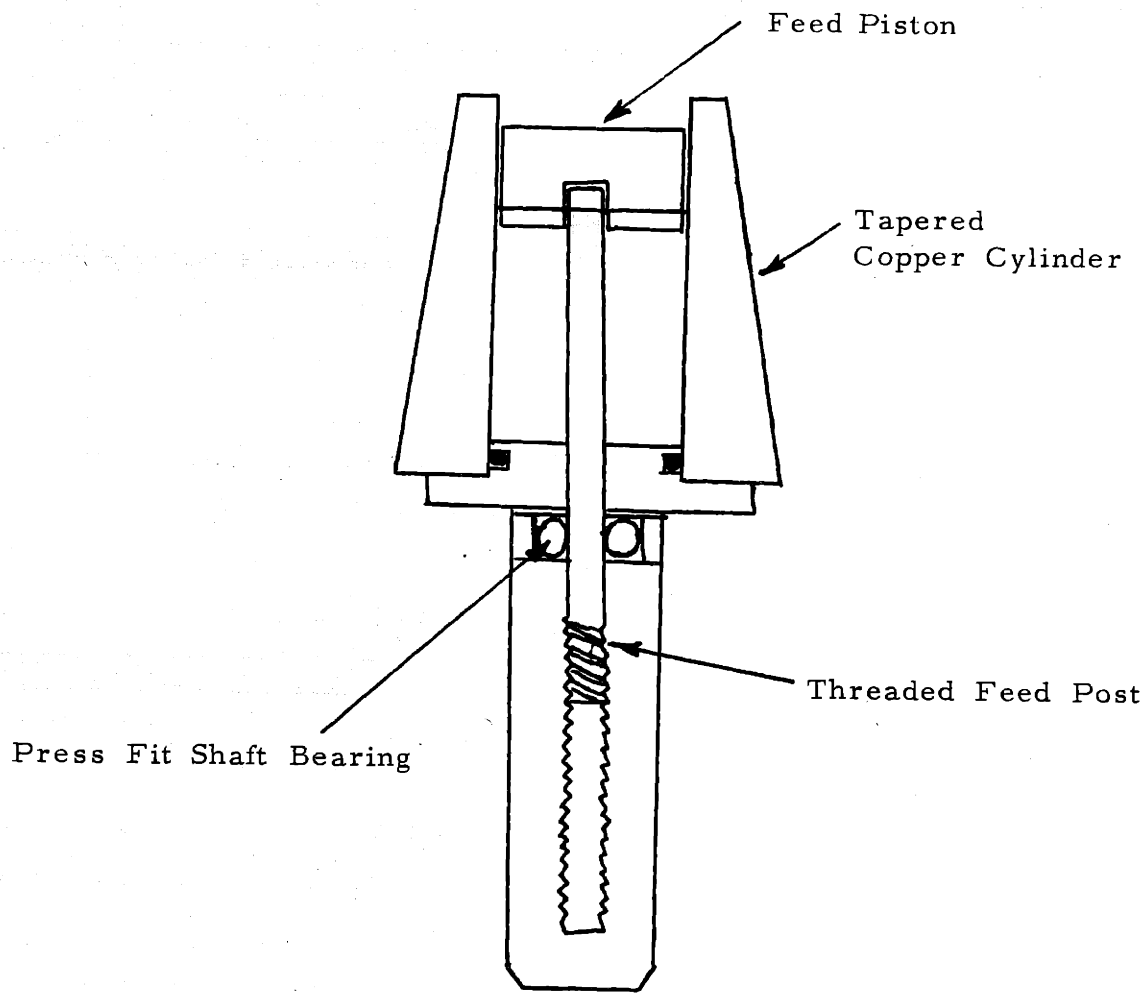
Figure 14   Manual feed piston mechanism.

3.   Materials Preparation

Several procedures were followed to obtain material for single

crystal growth. In one method, high purity niobium bars were used to

prepare both the niobium pentoxide and the niobium hydride that were to

be subsequently used to form the monoxide. In the second procedure

commercially available niobium pentoxide was reacted with niobium

hydride that had been formed from the high purity niobium. A third

procedure utilized high purity niobium rods and commerically available

niobium pentoxide powder, the reaction being carried out directly in the

Tri-Arc furnace.

(a) Hydriding Procedure and Pentoxide Formation

Electron beam refined niobium bars of 99.999 percent purity

were obtained from the Kawecki Company, New York City, New York.

Three six inch long bars, 3/8 inch in diameter, were placed in a niobium

foil-lined open-ended quartz ampoule, the foil liners were to prevent

silicon pickup from the quartz upon subsequent heat treatments. These

bars were then out-gassed consecutively at 200, 400, 600, 800, and

1000°C in a dynamic vacuum. The temperature was raised to the next

level when the pressure dropped below 5×10^{-6} torr. Starting at 1000°C,

hydrogen, diffused through palladium was admitted into the system.

After reaching a dynamic equilibrium at 1000°C, the temperature was

lowered in 200 degree steps whenever a dynamic equilibrium obtained.

Hydriding was done so that the bars could be reduced to powder form

for a more complete oxidation. Crushing and sieving (to > 325 mesh but
< 100 mesh) was carried out in a portable dry box under a purified
helium atmosphere utilizing a diamond brand mortar and pestle and
stainless steel sieves. Part of the niobium hydride powder was stored
under a positive helium pressure for later use. The remainder was
transferred to a double-trapped, flow-through furnace in which a posi-
tive pressure of purified oxygen was passed. The furnace temperature
was raised in steps until upon reaching 800°C, oxidation was allowed to
proceed to completion (Nb_2O_5). The oxidation product was tested by
X-ray diffraction and found to be only the low temperature, non oxygen
deficient form of niobium pentoxide.

(b) Niobium Monoxide Formation

In one of the procedures listed above, niobium hydride powder
and niobium pentoxide powder, both formed from the pure niobium rods,
were mixed in the proper proportions according to the equation

$$3 \, Nb + Nb_2O_5 \rightarrow 5 \, NbO$$
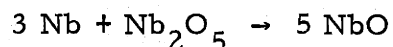
The powders were mechanically mixed and placed in a 10 inch long
recrystallized alumina boat; then heated to 1000°C for 24 hours under
a vacuum of about 5×10^{-5} torr. X-ray diffraction analysis showed
lines of niobium, the monoxide, the dioxide, and a trace amount of the
pentoxide. The prereacted powders were pelletized (one inch diameter,
1/2 inch thick, 50,000 psi) and placed on an alumina support inside a
vacuum furnace. The vacuum unit was a tantalum resistance heated

furnace capable of obtaining temperatures in excess of 2000°C for
several hours while operating in vacuum or a purified argon atmosphere.
The niobium-oxide pellets were heated to 1650°C for two hours. X-ray
examination showed small amounts of free niobium and NbO_2 as well as
the monoxide. After two more hours at 1650°C, the niobium and NbO_2
phases were still present. Some of the previous investigators[29, 33] have
reported the formation of the monoxide by one-half hour treatment at
1650°C in vacuum. In the present investigation, the elimination of free
niobium and of the dioxide was completed only upon melting of the sam-
ples. Combustion analysis of samples subjected to 1650°C treatments
under vacuum showed as much as a 20 percent decrease in the oxygen/
niobium molar ratio. Thus, it is not surprising to find a variation of
the lattice parameter for "$NbO_{1.0}$" as in the literature (see Section
IV-G).

A much closer control of stoichiometry was achieved by the
use of the Tri-Arc furnace. Pressed niobium powder or niobium rods
were placed on top of a pellet of niobium pentoxide inside the feed
cylinder of the hearth. The arcs were initiated to the niobium bars
which melted and then reacted with its 'container', the pentoxide. One
could see the melt settle down into the feed cylinder as the reaction
proceeded. The copper (or graphite) feed piston was elevated as the
reaction progressed. In this manner, oxygen losses were kept below two
percent and the stoichiometry desired could be obtained by the addition
of a small excess of niobium pentoxide.

As experience was gained by further use of the Tri-Arc furnace, the powders were not pressed into pellets, but rather just tamped in the feed cylinder with a glass rod. Initiation of fusion was accomplished by playing the plasma surrounding the arcs over the surface of the metal powder.

4.   Crystal Growth of Niobium Monoxide

Starting materials were either previously arc-melted buttons of some given nominal composition (NbO_x) or pressed pellet mixtures of niobium and its pentoxide. In some cases niobium rods were placed on top of a pellet of niobium pentoxide. Approximately 25 to 35 grams was placed into the feed cylinder. The three arcs were initiated in an argon atmosphere and then moved to the starting material. Material was added to the molten pool from below by raising the feed piston. As material was added the power level was raised to maintain the liquid state in the buttons. A tapered tungsten rod was lowered into the melt and the arc power raised until wetting of the 'seed' was observed. The elevator was then locked and pulling begun. When the growing crystal had been tapered down to a thin neck, the water cooled seed holder was tilted off-axis towards one of the electrodes and the elevator raised, allowing the necked portion to grow back towards the thermal center. The angled necking procedure continued until the outside edge of the lower part of the neck was inside the inner edge of the upper neck. This "elbowing" helped ensure the elimination of extraneous grains. Occasionally one could see surface features in the neck region and so make an intelligent choice as towards which electrode to tilt the seed.

To start the boule growing out from the neck the heat balance between the necked crystal and the molten puddle had to be changed. The change in the heat balance was accomplished in two ways, (1) by

turning down the total power to the three arcs as a unit, or (2) by moving the electrodes further out towards the periphrey of the melt and decreasing the arc length. Since each electrode has a series variable ballast resistor, manipulation of the electrodes provided a more fine control over the crystal growing operation than that given by raising or lowering the total power of all three arcs simultaneously. Shortening the arc length puts the incident power into a smaller area thereby lowering the temperature slightly at the crystal-melt interface and enhancing the growth.

As the boule began to grow and when the desired diameter was reached, either of two operations was performed to maintain an approximately constant dimension; the total power level was raised by a small amount with the electrode positions remaining fixed or the pulling speed was increased. To obtain diameters of about 1/2 inch in NbO, pulling speeds of the order of 3 to 4 inches per hour were used. Occasionally with smaller diameter boules of NbO, it was not possible to manually rotate the elevator shaft fast enough to decrease the diameter (approximate pulling speeds of 20 to 30 inches per hour). Until more is known about the heat balance-growth velocity relationships in the Tri-Arc Czochralski furnace, its limitations as to pulling speeds cannot be known.

Figure 15 shows the growth of an off-stoichiometry NbO crystal. In this photograph the solid-liquid interface is seen to be approximately at the liquid surface, whereas in the growth of crystals with an apparently poorer thermal conductivity such as Ti_2O_3, the solid-liquid

interface was maintained as high as 1/8 inch above the melt for a 3/8 inch diameter boule. The crystal shown in Figure 15 had a growth direction of $\langle 111 \rangle$ and is seen to have a poor surface luster. Crystals grown in the $\langle 110 \rangle$ or $\langle 100 \rangle$ direction tended to have brillently silver surfaces.

If one uses a $\langle 100 \rangle$ seed crystal of NbO, it was found that square cross sectional crystals could be grown with ease. Maintaining a constant dimension in this case was however more difficult than when growing an arbitrary orientation. Occasionally with the $\langle 100 \rangle$ seed orientation, sections of the crystals would be uniform enough to give large (100) facets that could be used for optical measurements (1/8 by 1/4 inch).

The combination of a single total power control, the positioning of the electrodes, the current variability to each electrode, and the ability to change the arc length enabled the author to melt and grow crystals of from tin (melting point 232°C) to titanium carbide (melting point ~ 3150°C). The versatility and ease of operation of the Tri-Arc Czochralski furnace was demonstrated by the formation and growth of seven different materials in one day (Figure 16). Although some of the boules were not single crystals, they had large enough grains for certain measurements. By judicious choice of seed, power level, and pulling speed, all of the crystals exhibited could be grown single.

Some of the crystals that have been grown thus far in the Tri-Arc Czochralski furnace include: NbO; VO; $(Nb_{1-x}V_x)O$ for $x < 0.2$; Ti_2O_3; Ti_3O_5; Ti_2O_3 with 2 percent V doping; Ti_2O_3 with 2 percent V, 1 percent Fe, and 1/2 percent Mn doping; Sn; Ge; Ni; Co; Cr; V; Nb; Ti; $TiO_{1.2}$; Cu_2O; and TiC.
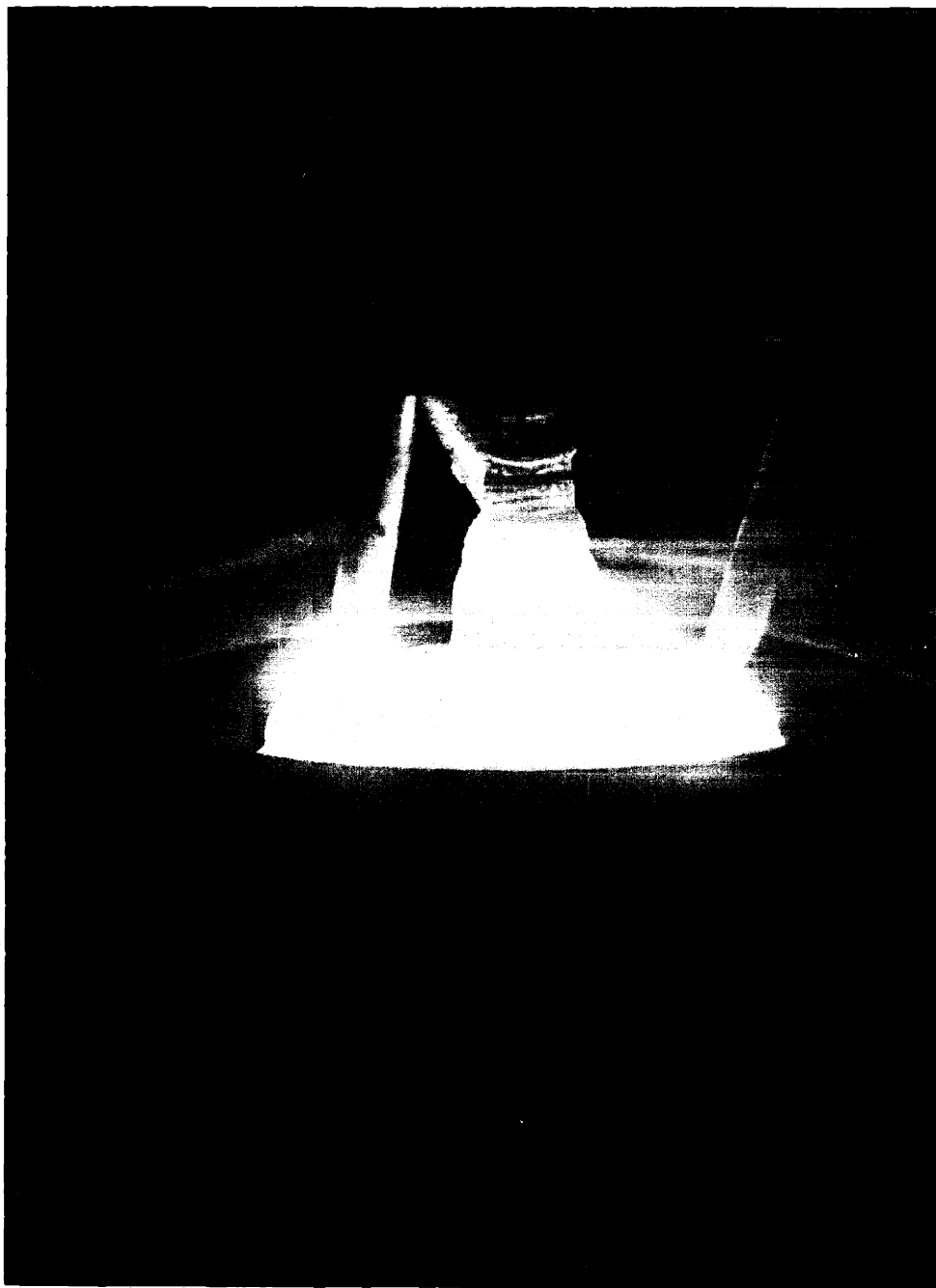
Figure 15   Growth of off-stoichiometric NbO_x.
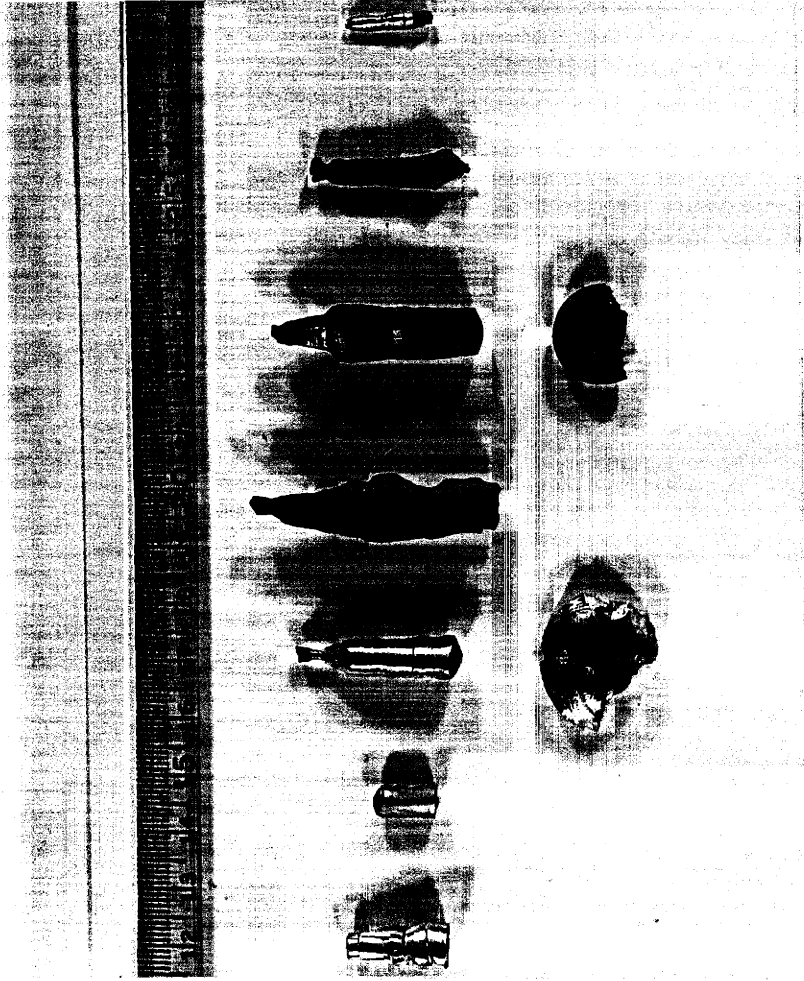
Figure 16   Display of crystals grown in one day with the Tri-Arc Czochralski Furnace
(l. to r., Sn, Ge, V, VO, Ti_2O_3, Cr, and Nb).

5.   Other Applications of the Tri-Arc Furnace

Several other uses can be made of the Tri-Arc unit, including splat cooling, drop casting, pressure casting, and operation as a plasma torch.

(a) In splat cooling, a spring loaded solid copper cylinder (hammer) is subsituted for the crystal pulling shaft (Figure 17). A solid base (part E in Figure 13) is used in place of the feed piston unit. A small charge of material is melted using a large power density. The hammer is then released onto the melt, spreading the sample rapidly and thinly over the hearth.

(b) In drop casting, the sample is placed over a slightly smaller hole in the hearth. As the sample is melted it is initially supported by the solid portion in contact with the rim of the hole. When this portion finally melts, the whole sample drops into the hole (Figure 18a).

(c) In pressure casting, the sample is forced by the slightly positive chamber pressure into a silica or carbon tube when the tube is dipped into the melt, as shown in Figure 18b. Drop casting or pressure casting are nicely suited for making solid samples for use in high pressure experiments.

(d) A plasma torch can be made very simply by using a single cathode in place of the crystal pulling mechanism and a copper anode shaped as a nozzle, as is shown in Figure 19 . Laminar and turbulent flames of argon, nitrogen, and air, some extending 15 to 30 cm beyond the nozzle, have been generated in this manner.[42]

SPRING-DRIVEN
COPPER HAMMER

SAMPLE
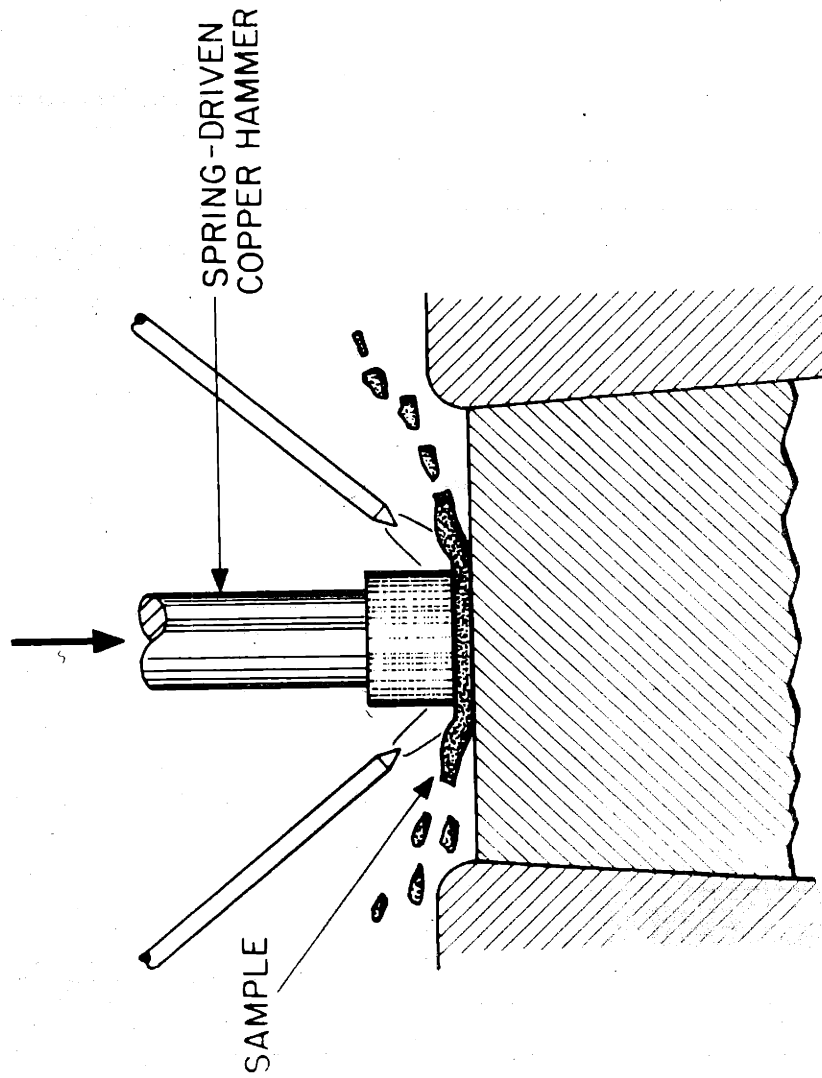
Figure 17   Schematic of a splat-cooling adaptation of the Tri-Arc Furnace.

CASTING
TUBE

SAMPLE

SAMPLE
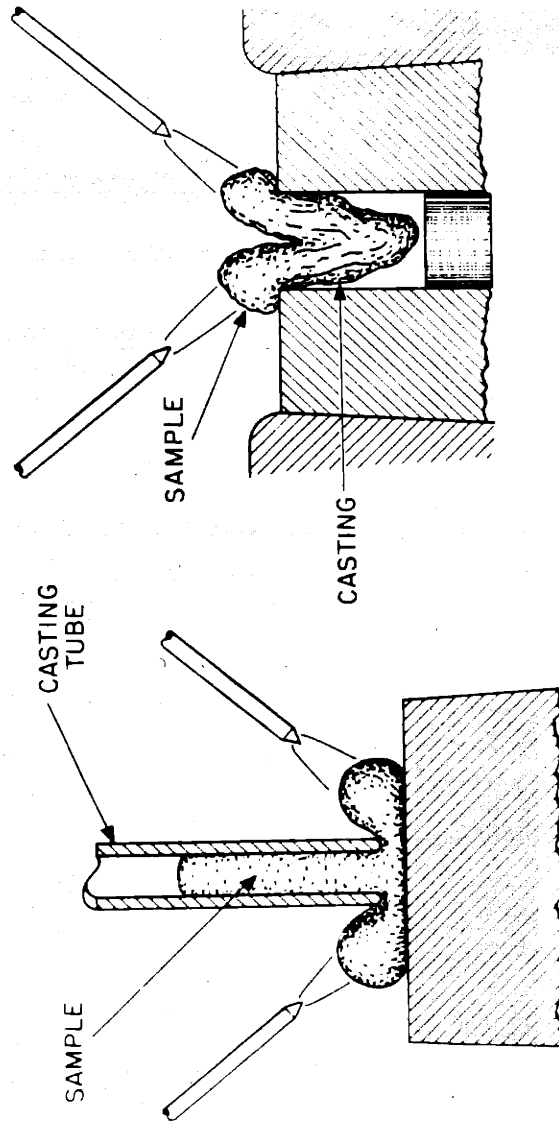
CASTING

Figure 18a and b   Schematics of drop-casting and pressure casting adaptations to the
Tri-Arc Furnace.

NOZZLE
ANODE

PLASMA FLAME
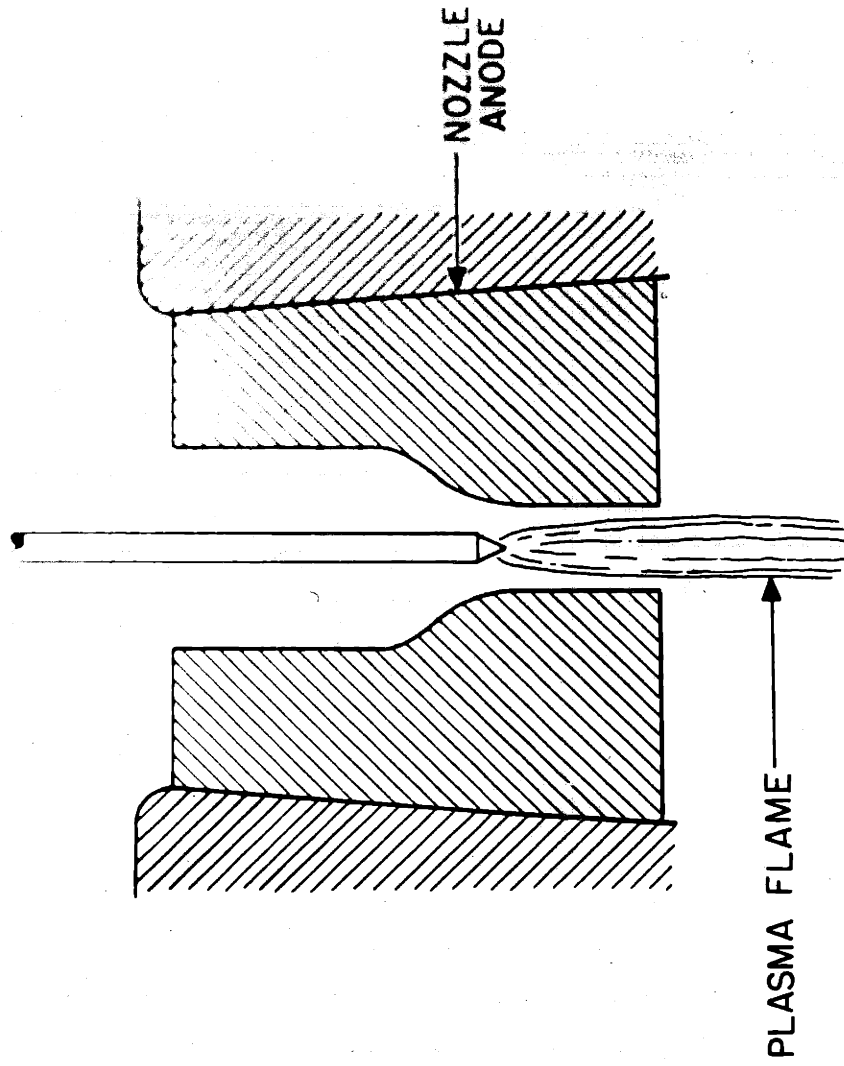
Figure 19 Schematic of plasma torch configuration in the Tri-Arc Furnace.

B. Property Measurements Procedures

1. Electrical Resistivity

The electrical resistivity of the NbO_x samples was measured using a standard four point probe technique. A block diagram of the apparatus is shown in Figure 20. Resistivity as a function of temperature was determined over two ranges: (1) 4.2 to 77°K and (2) 77 to 300°K. Temperature control was maintained by enclosing the sample inside a copper sheath which contained a wire wound resistance heater. The sample chamber was then either immersed in a liquid helium (nitrogen) bath or suspended over the bath while current was supplied to the heater. Several minutes were required for the sample and chamber to equilibrate. Voltage drop between the resistivity leads was generally measured for several current levels, typically 1/2, one, and two amperes. The direction of current flow was reversed twice for each current level, the four values obtained for each current level were then averaged for the single datum point.

Good electrical (ohmic) contacts were made to the NbO samples by a number of conventional techniques, however, they were generally poor mechanical bonds. Two techniques that led to good electro-mechanical bonds were (1) capacitance-discharge welding of 1 mil copper lead wire and (2) ultrasonic indium dotting. The capacitance welder had a total capacity of 8000 μfarads and operated best at a potential of fifteen volts. In ultrasonic indium dotting the sample was heated to 150°C on a hotplate,

an unheated ultrasonic probe (not vibrating) was dipped into an indium

bath. The ultrasonic probe with the small indium dot was then touched

to the sample and the vibrator turned on. The probe was in contact

with the sample for only a few seconds. The sample was taken off the

hotplate and put into a jig that held the copper lead wires against the

indium dots. A tinned (with indium) needle point soldering iron was

then brushed across the copper lead and the indium dot.

The distance between the voltage probes was measured with the

aid of a traveling microscope.

$\frac{1}{2}$-12NC Threaded for
Heater Cap

1) Current measurement
2) Resistivity
3) Temperature
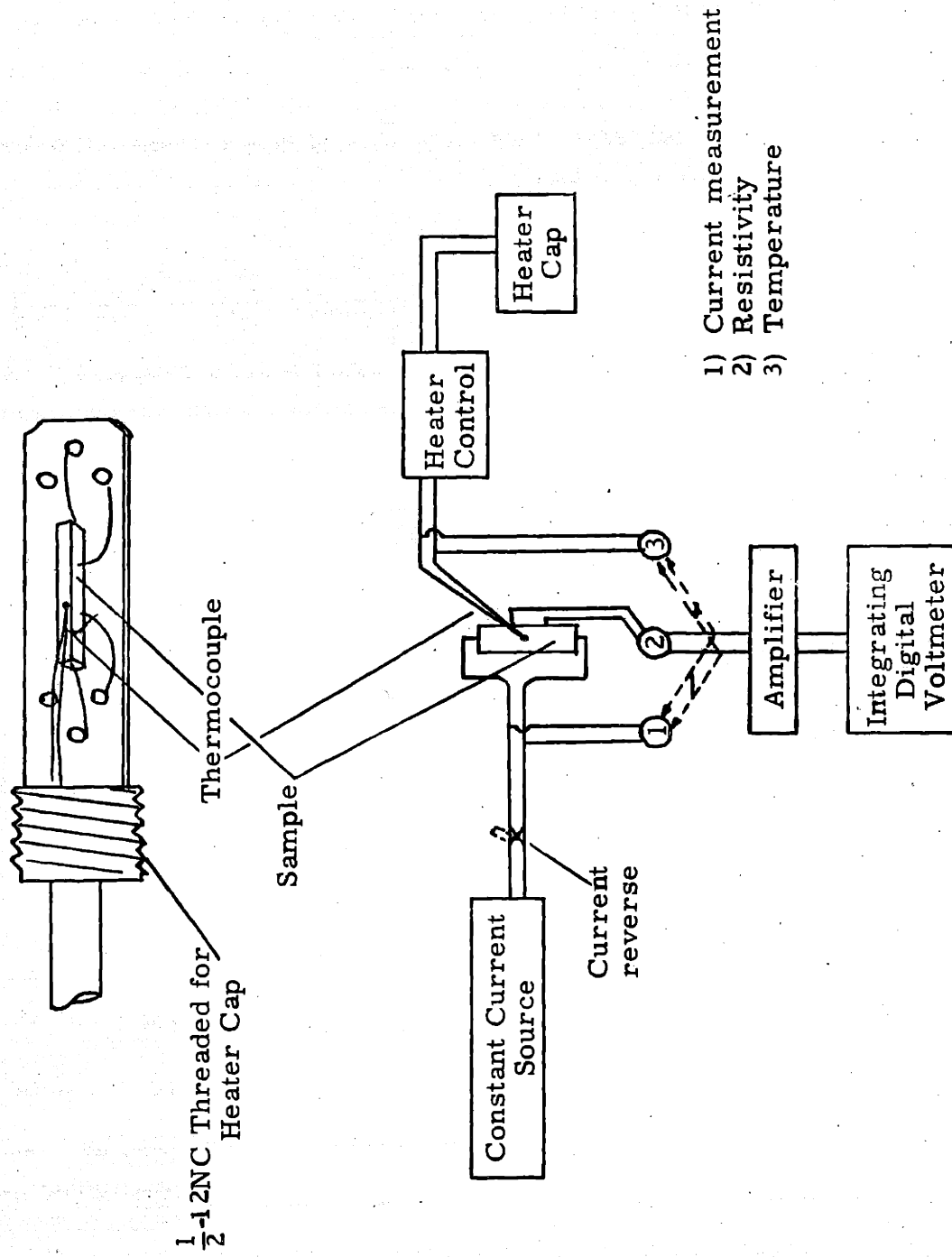
Figure 20   Schematic of the electrical resistivity apparatus and the sample holder.

2. Magnetoresistivity and High Field Hall Effect

The sample configuration and the experimental schematic for the measurement of the magnetoresistance and the high-field Hall constant is shown in Figure 21a, b, and c. The samples were mounted on a Teflon slab which was attached to the end of a thin walled stainless steel tube. The insulated leads were twisted and brought up through the tubing, exiting at the top of the tubing via a Jones connector. The tube and sample holder were inserted through a styrofoam and brass cap attached to the top of a liquid helium dewar. For fixed-angle transverse magnetoresistance and high-field Hall effect measurements, a helium dewar with a 17 inch long, 2 inch OD tail piece was placed in a 2 inch bore, axial-B, magnet that was capable of attaining 150,000 gauss. For the rotation experiments to determine the angular dependence of the transverse magnetoresistance, a belt driven rotatable head was attached to the sample wand and this total unit was placed in a helium dewar with a 12 inch long, one inch OD tail piece. A special one inch radial-access magnet was then used for the measurement. The radial-access magnet had a high field limit of about 95,000 gauss.

In measuring the fixed angle magnetoresistance, the magnetic field would be raised to the desired value, the potential drop measured, and then the current direction would be reversed and the potential drop measured again. The current reversal procedure was used with

each increase in the magnetic field up to its maximum strength and again upon the return to zero field. On reaching zero field strength the magnetic field direction was reversed and measurements repeated with increasing and decreasing fields.

For rotational transverse magnetoresistance, a constant value of magnetic field was used. The potential drop was continuously recorded as a function of angle and for several angular velocities. Current reversal and field reversals were also carried out. After the angular-dependant potential drop had been measured at one rotation rate, the current leads were shorted and the e. m. f. generated by the current-loop motion through a magnetic field was determined. The actual potential then for the angular dependence of magneto-resistance is the difference between the current-on and the shorted conditions.

As will be noted in the results of these measurements in Section IV A, the belt driven device did not give complete slippage free operation and thus led to some variation in the rotation results. A more positive drive mechanism would be much desired.

a) Sample Configuration for fixed angle magnetoresistance and high field Hall effect measurement

b) Equipment schematic used in the measurement of magnetoresistance and Hall effect

c) Sample configuration for rotational magnetoresistance
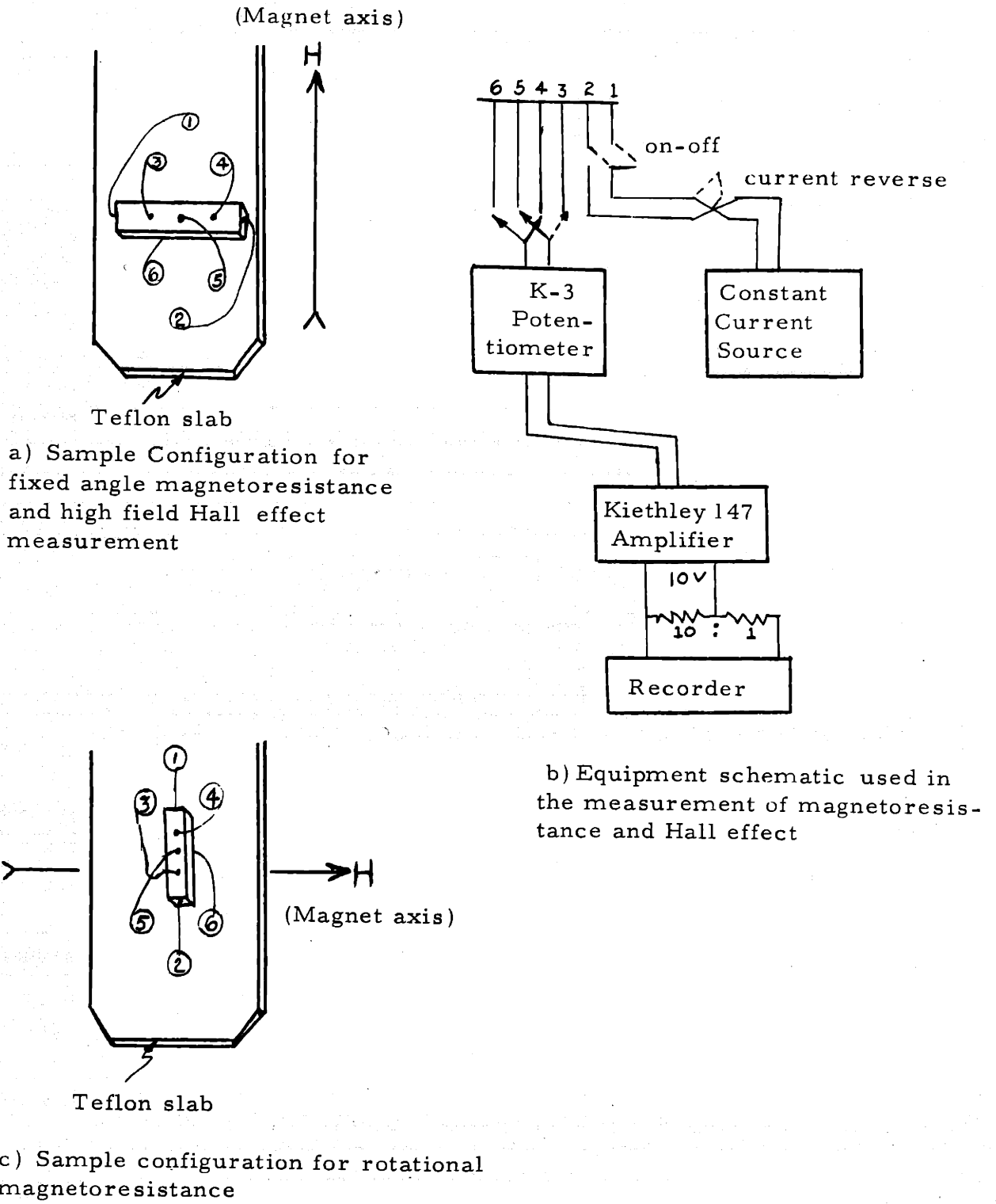
Figure 21   Sample configurations and equipment block diagram for magnetoresistance and Hall effect measurements

3.   Optical Measurements

Room temperature reflectance measurements at near normal incidence were made on three different types of samples: 1) an as-grown (100) facet; 2) a cut and polished (111) surface; and 3) a (100) cleaved surface.   The crystals were grown by a new crystal growth technique described in Section II A, and all were near the stoichiometric composition.   The reflectivity was determined over two energy ranges, 0. 05 to 3. 5 eV, and 2. 7 to 12 eV.

Several difficulties are encountered when making measurements of the absolute optical reflectance on small crystals.   Three of the main problems are: 1) obtaining identical incident and reflected beam paths; 2) obtaining absolute reflectance by avoiding an intermediate reflection standard; and 3) providing a suitable mask in the reflected beam to exclude reflections other than those from the sample, and still obtain identical masking in the incident beam.   The first of these problems requires that the optical path for reflected and incident beams enter and exit the sample compartment windows on identical paths and that the beam splitting occur inside the compartment. The path lengths must also be identical, and only one extra reflection, that from the sample, should occur between reflected and incident beams to obtain an absolute measurement without a comparison standard.   The third problem is ideally solved by using the same mask in the incident and reflected beam.

The first experimental arrangement described here[43] has been used to measure the low energy range of absolute reflectivity of niobium monoxide single crystal samples at room temperature with an overall accuracy of about one percent, and a relative accuracy or reproducibility of about 0.1 percent, even in the range of 90 percent reflectivity. With a Perkin-Elmer (12C) prism monochromator using well regulated tungsten and globar sources and with photomultiplier, lead sulfide and thermocouple detectors, the spectral range from 0.05 to 3.5 eV was covered.

Figure 22 is a schematic of the optical system used. The reflectivity spectrum is obtained by making two serial scans over the same spectral region and recording the incident and reflected signals. The monochromatic light from the exit slits is focused on diagonal mirror D and directed into the sample compartment by a second concave mirror. This portion of the light path is unchanged for the incident and reflected measurements. Mounted in the sample chamber are a fixed mirror C, and a rotatable post with two small mirrors attached to it as shown in the figure inset.

With this construction, measurements are made by rotating the flip mirror to position 1 for the incident beam and position 2 for the reflected beam. In position 1, light is reflected from mirror A to mirror C which is at a focal point. The light from mirror C passes through the exit window of the compartment to the detector focusing

mirror. In position 2, light from mirror A is incident on the sample

which is also at a focal point. The sample reflects light onto mirror B

and the light then follows the same path as for the incident beam through

the exit window to the detector. Thus, the optical paths differ only

by the single extra reflection from the sample. While this system

results in a reflectivity measurement without a comparison standard,

it should be noted that different mirrors are used in the two beam

positions: mirror B is used in the reflectance position and mirror C

in the incident position. To minimize errors in absolute reflectance

introduced by differences in these mirrors the mirrors were

aluminized simultaneously. The angle of mirror A relative to mirror

B and the position of mirror C are permanently adjusted so that the

path lengths for the two beams are identical. This allows the use of

small area detectors, such as a thermocouple, without any refocusing

of the detector mirror. With positive spring pressure stops, one can

readily switch between incident and reflected beams with good

reproducibility by rotation of the flip mirror post.

Accurate masking of the light beam so that all reflected light

exclusively from the sample reaches the detector is essential for

absolute measurements. Masking was accomplished by making use

of the fact that both mirror D and the sample are at focal points.

The mask consists of two brass cylinders that screw up and down

the post to which mirror D is attached (see Figure 22 inset). This

mask is adjusted at mirror D so that the light image at the sample

just fills the desired reflecting surface area. Since the masking is done at D, both the incident and reflected beams are identically attenuated and no other masking is required.

For the second spectral range, 2.7 to 12 eV, a McPherson monochrometer (aluminized concave replica of a ruled grating, 600 lines per cm.) in a commercial UV spectrometer was used (Figure 23). The total system has been described by Scouler [44]. Since the McPherson monochromator unit could be used down to about 2.5 eV, the data from 2.7 to 3.5 eV were normalized to the absolute data obtained with the lower energy monochromator described before. The data below about 6eV were taken using a tungsten filament lamp as a source; above 6 eV to about 10 eV, a hot cathode light source containing hydrogen gas was used; and from 10 to 12 eV, helium and neon gasses were substituted for hydrogen. The exciting source was of a type described by Hartman [45].

The reflectivity spectrum was limited to below 12 eV because of the use of LiF as the window material in the sample chamber (LiF transmission limit ~ 1050 $\overset{o}{A}$). A sodium salicylate coated quartz window converted the reflected UV light to visible light which was then detected by a conventional photomultiplier. The photomultiplier signals were fed into a Keithley 610A electrometer which drove a strip chart recorder. Serial scans over the same spectral region were made obtaining the incident and reflected light.

Sample

Detector

CaF$_2$
Window

1

A

B 2

c

D

Perkin-Elmer 12C
Light Source

Sample
Chamber

Mirror D

Mask for
Diagonal
Mirror D

B

A

Brass post
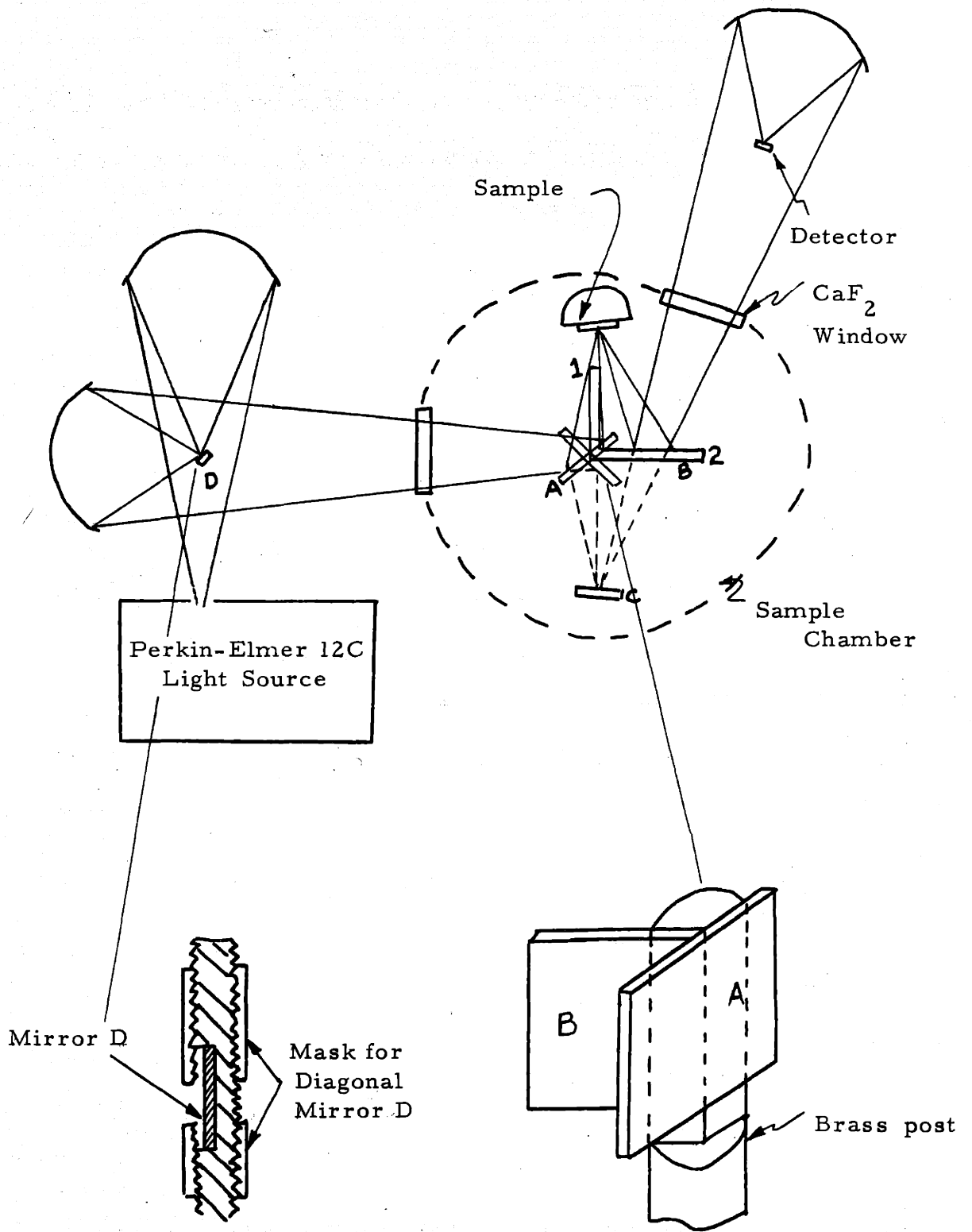
Figure 22   Optical light path in the Perkin-Elmer C12 unit with
inserts of the masking technique and the flip mirror
arrangement
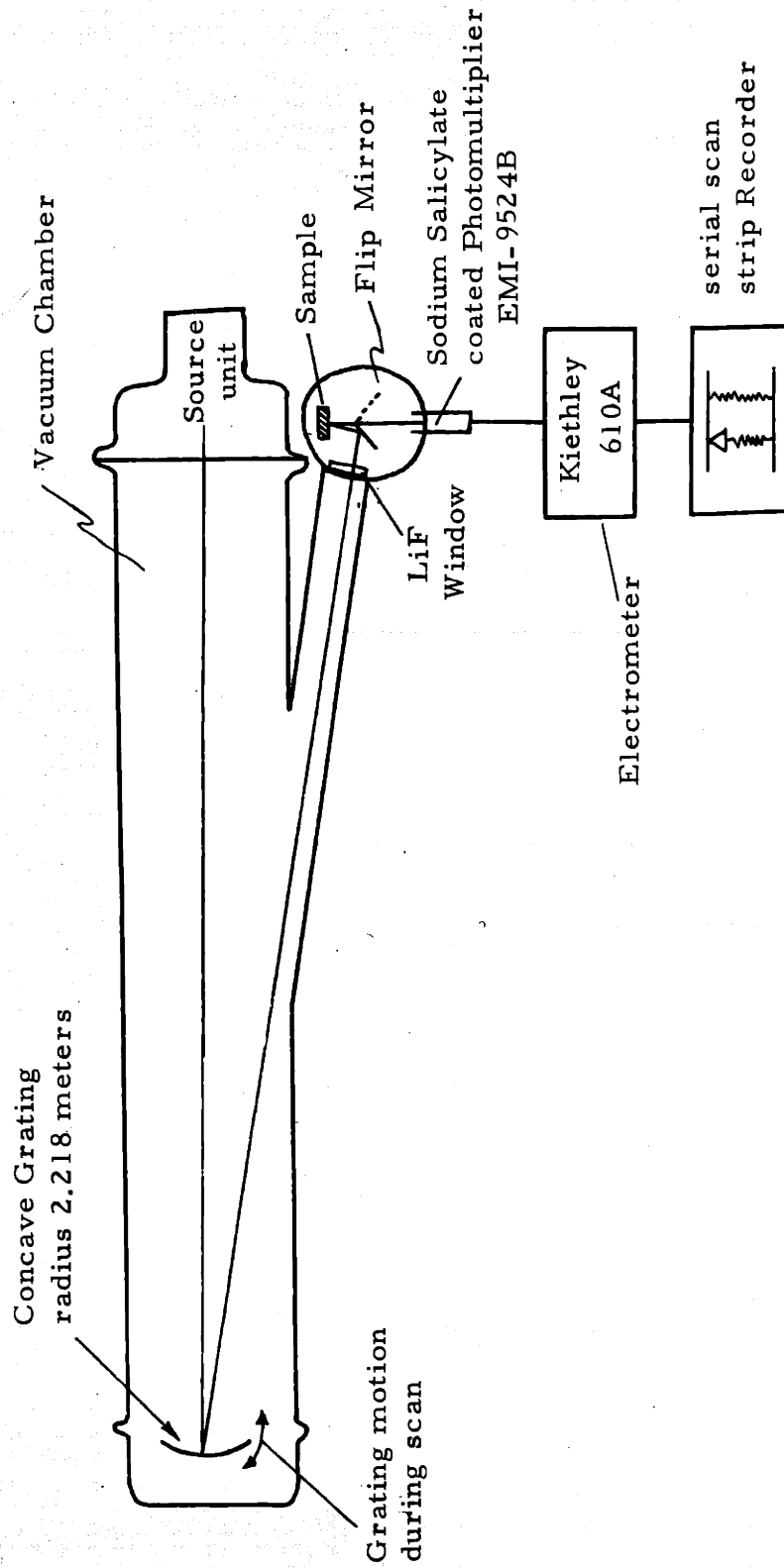
Figure 23 Schematic light path in the Ultra Violet spectrometer.

4. Magnetic Susceptibility

Two sets of apparatus were used in the determination of the magnetic susceptibility of niobium monoxide and its dependence on temperature and composition. A vibrating coil magnetometer, shown schematically in Figure 24, was used for fixed temperature measurements (4.2, 77, and 300°K). A powdered sample, approximately 500 mg in weight, was put into a Teflon cylinder that was attached to a phenolic resin rod. This assemblage was raised and lowered by hand to pull the sample out of or push it into the magnetic field sampling coils. The magnetic field used for the measurements was 10,000 gauss. A nickel standard with a moment of 9.215 emu was used for calibration. It was necessary to move the sample in and out of the vibrating coils due to the inherently small signals from the weak moment material. The vibrating coil apparatus can be adapted to continuous measurements as a function of temperature but generally only for large moment samples where any signal or noise drift in the associated electronics would be small compared to the sample signal.

Measurement of the magnetic moment of the samples as a function of temperature was accomplished in a vibrating sample apparatus (Figure 25). The sample was in powder form and encapsulated in a Teflon cylinder, which was then attached to a long quartz rod. Sample weights were about one half gram and a nickel standard was again used. The sample was immersed in a liquid

helium bath and its moment measured. As the bath warmed up, the moment was remeasured by the balancing of an attenuator on an oscilloscope. The signals that are matched on the scope are the reference signal from a small pick-up coil atop the apparatus near the loud speaker drive mechanism and the sample signal from a fixed coil mounted around the sample. The matching of the signals was tedious and not totally satisfactory due to temperature drift that occurred during the measurement and to extraneous noise in the associated circuitry. However, it is applicable up to about 20°K. The drift rate was too rapid above about 20°K to make meaningful measurements.
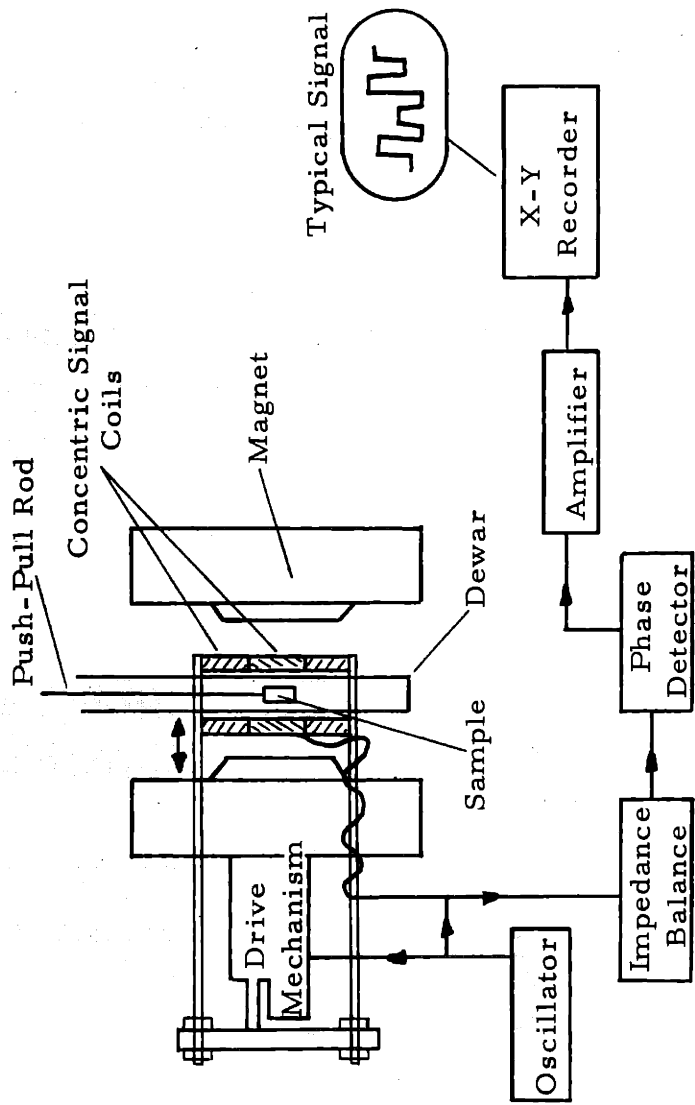
Figure 24   Fixed temperature, vibrating coil magnetometer
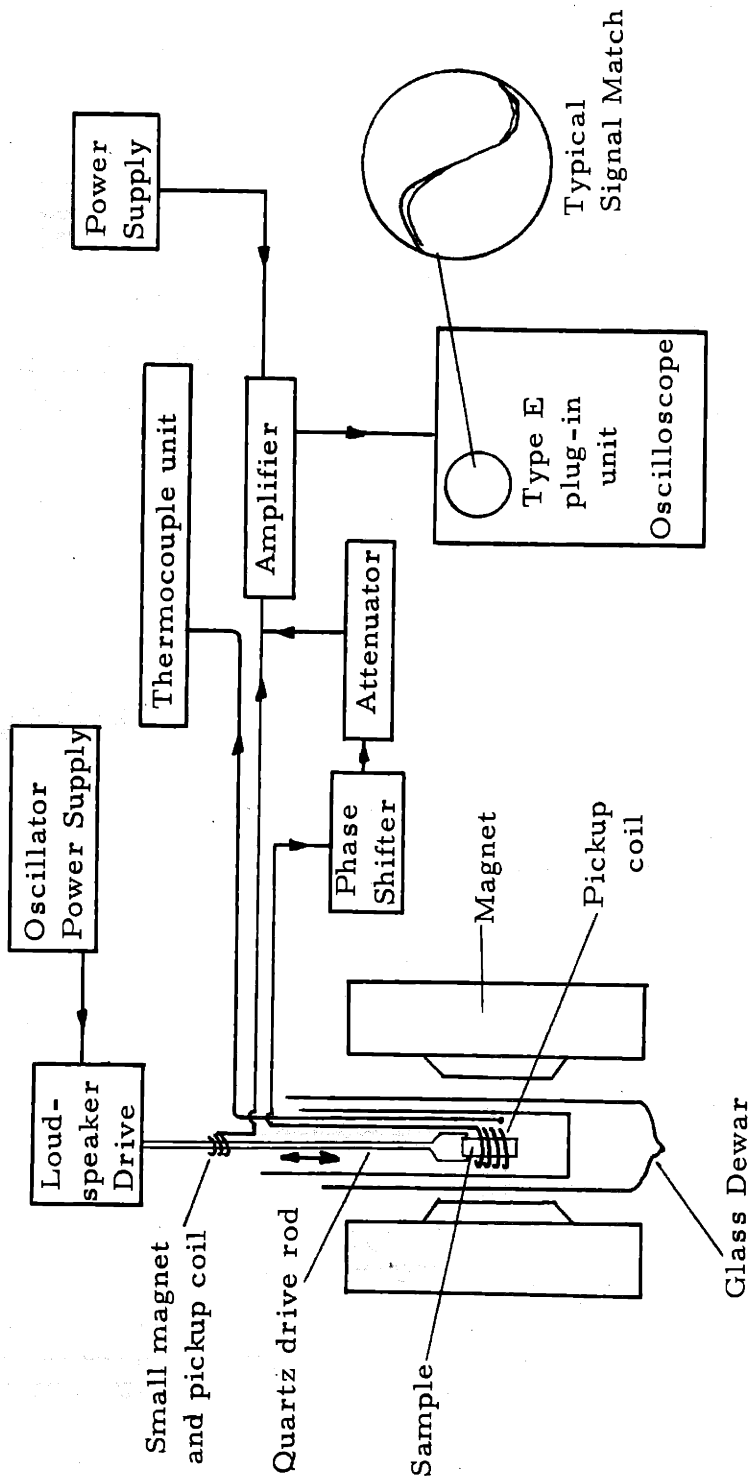
Figure 25   Temperature drift, vibrating sample magnetometer.

5.   Superconducting Transition Temperatures

A self-inductance technique was used to determine the super-
conducting transition temperature of the NbO_x crystals.   The technique
is similar to that described by Merriam and Von Herzen[46].

The inductance measurement technique makes use of the change
in magnetic susceptibility that occurs when a sample becomes
superconducting; for instance, a typical sample may change from a
possibly weak paramagnetic state to a perfect diamagnetic state.
A sample is placed inside of a simple inductance coil which is
connected into an oscillator circuit (for example, in a Colpitts
oscillator circuit).   The sample then is an integral part of the overall
inductance of the coil so when the sample susceptibility changes, the
inductance in the oscillator circuit changes, creating a shift in the
natural frequency of oscillation.   The inductance coil is driven by an
oscillator at about 1000 hertz and when the sample becomes
superconducting, the frequency of oscillation changes by 30 to 60
hertz.   The frequency shift is monitored by a commercially available
frequency meter.

Measurements were generally made over two temperature ranges,
above and below 4.2°K.   Measurements below 4.2°K were made
using a Wallace-Tiernan pressure gauge for the determination of
the pressure over a boiling helium bath in which the samples were
immersed.   Below the boiling point of helium, point by point

measurement is required: noting both the frequency and the vapor pressure. Above 4.2°K, continuous recording is feasible with the use of the output of a gold-cobalt, copper thermocouple in conjunction with the frequency meter output, both signals being recorded on a two channel pen recording instrument.

The use of the inductance technique has possibly a major disadvantage in the measurement of superconducting transition temperatures. If a sample exhibits superconductivity of a filamentary type, the transition temperature so determined would not be that of the bulk material due to the shielding by the super conducting filaments that would occur. This measurement is especially questionable if the material is not homogeneous or if it consists of two phases, both of which may exhibit superconductivity. However, the technique is simple and fast and the shielding problem from superconducting filaments can be eased by utilizing various frequencies and by using powdered samples thereby changing the sampling penetration depth.

6.   Precise Lattice Parameter Determination

The unit cell lattice parameter of NbO_x samples as a function

of composition was determined using a back reflection focusing

camera.   A regular powder pattern from a Debye-Scherrer camera

with careful measurement of line positions allows one an uncertainity

in the lattice parameter of about $\pm 0.001 \overset{o}{A}$.   The back reflection

focusing camera, by expanding the scale and thus the separation of

the $K\alpha_1$, $K\alpha_2$ lines as well as bringing in the primary $K\beta$ line, and

by focusing the diffracted beam thus increasing the sharpness of the

lines, allows almost an order of magnitude increase in the preciseness

of the measurements.

Pieces of single crystal samples were crushed to less than 325

mesh in a stainless steel motar and pestle.   A thin collodion film

was spread onto a rectangular sheet of unexposed,developed film

and a powder layer of the sample was poured onto the collodion.

Mounting clamps formed the sample and film around the circumference

of the 57. 3 mm radius camera.   The sample was oscillated around the

circumference about the beam axis.   On the circumference of the

camera were V-notches cut every ten angular degrees for use in

film shrinkage calculations.   A typical exposure time for the single-

sided emulsion film was three hours.   After development of the films,

they were allowed to drip dry.

The films were read on a light box incorporating a magnifying eyepiece and a vernier millimeter scale. The lines obtained, α_1, α_2, and β, were then used in a Cohen [47] extrapolation technique resulting in a precise parameter determination known to about ±0.0002 Å. With the present technique, this limit is about the best one can obtain without going to a thermostatted jacket for the camera.

7.   Determination of the Oxygen to Niobium Ratio

The oxygen/niobium molar ratios were determined by combustion analysis. Samples were crushed in a steel mortar and pestle to sizes less than 250 mesh (~ 0.06 mm) and spread loosely along the bottom of a fused silica boat. The boat and its contents were heated in air at 1000°C for four hours then at 750°C for 12 hours; the second heating was required to complete the reaction to the pure white 'popcorn' form of niobium pentoxide as the 1000°C treatment results in the yellow oxygen-deficient β - Nb_2O_{5-x}. X-ray diffraction powder patterns of the final white combustion product indicated only the low temperature, oxygen/niobium = 2.5, form.

Orginally the combustion analysis was carried out in high purity oxygen at a slightly positive pressure but comparison of air-heated versus oxygen-heated results on adjacent sections of the same samples of TiO and NbO indicated a maximum difference of only slightly less than 0.2 percent in the O/Nb molar ratio. As will be seen below, this procedure determined the limits to which the composition of the samples could be found.

The maximum error involved in combustion analysis of the composition of niobium monoxide samples was determined as follows: the reaction

$$NbO_x + \left(\frac{5}{2} - x\right) O_2 \rightarrow \frac{1}{2} Nb_2O_5$$ is assumed to occur,

from mass action, we get

$$\frac{w_i}{w_f} = \frac{A_{Nb} + xA_O}{\frac{1}{2}\left[2A_{Nb} + 5A_O\right]}$$

solving for x (the molar ratio)

$$x = \left(\frac{A_{Nb}}{A_O} + 2.5 \right) \frac{w_i}{w_f} - \frac{A_{Nb}}{A_O} \; ;$$

so

$$\Delta x = \frac{\partial x}{\partial w_i} \Delta w_i + \frac{\partial x}{\partial w_f} \Delta w_f + \frac{\partial x}{\partial A_{Nb}} \Delta A_{Nb} + \frac{\partial z}{\partial A_O} \Delta A_O,$$

$$= \frac{1}{w_f} \left(\frac{A_{Nb}}{A_O} + 2.5 \right) \left(\Delta w_i - \frac{w_i}{w_f} \Delta w_f \right) + \frac{1}{A_O} \left(1 - \frac{w_i}{w_f} \right)$$

$$\left(\frac{A_{Nb}}{A_O} \Delta A_O - \Delta A_{Nb} \right) .$$

Since the weighings on the balance used were reproducible to at least 20 milligrams, $\Delta w_i \approx \Delta w_f \approx 0.00020$, and the atomic weights of the elements involved are known to at least 0.01, especially oxygen, $\Delta A_{Nb} \approx 0.01 \approx \Delta A_O$. A typical sample used had a starting weight between one and two grams, so one may set $w_i \sim 1.50$ and $w_f \sim 2.00$ grams. Putting these values in the above equation results in a value of uncertainity for $\Delta x \approx 9.6 \times 10^{-4}$, or that the oxygen to niobium ratio could be determined to ± 0.001. It is noticed that this uncertainity is one half that seen in the difference between oxygen-heated and air-heated analyses. Combustion runs were made on three samplings of the same specimen as a rule, and the O/Nb ratios were generally within ± 0.002; this value then has been taken as the uncertainity in the compositions.

8.   Seebeck Coefficient Measurement

The thermoelectric power can be measured from the voltage pro-
duced in a thermocouple arrangement as in Figure 26. A small tem-
perature difference, ΔT, is put upon a sample (A) which has some mean
temperature $\overline{T}$. The voltage produced at the resulting junctions, T_1 and
T_2, is brought out to a reference junction, T_o, by wires of a reference
material, for instance iron or copper. The EMF around the circuit is
defined by the integral of the electrical field along the length of the wire:

$$V_{EMF} = \int_{x(T_o)}^{x(T_1)} E_B \, dx + \int_{x(T_1)}^{x(T_2)} E_A \, dx + \int_{x(T_2)}^{x(T_o)} E_B \, dx$$

$$= \int_{x(T_2)}^{x(T_1)} Q_B \frac{\partial T}{\partial x} \, dx + \int_{x(T_1)}^{x(T_2)} Q_A \frac{\partial T}{\partial x} \, dx$$

$$= \int_{T_1}^{T_2} (Q_A - Q_B) \, dT \approx (Q_A - Q_B) \, \Delta T$$

Thus the voltage generated is a function of the difference in temperature
of the two junctions and of the difference in the thermoelectric power,
Q, of the two metals.
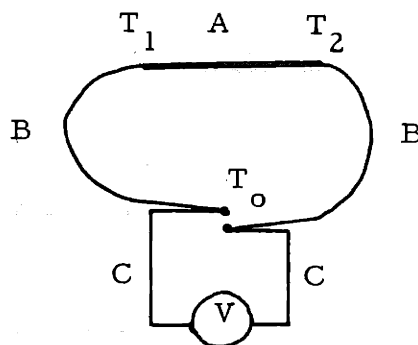
Figure 26. The Seebeck Effect

In line with the above discussion, two sets of apparatus were used in the determination of the Seebeck coefficient and were basically the same, differing only in the degree of sophistication. Figure 27 shows schematically the equipment used for the temperature dependence measurements. Figures 28a, b show the simple unit for room temperature measurements of the thermoelectric power.

When making measurements as a function of temperature down to 77°K, the dewar in Figure 27, which contains the sample and heater assemblage, is pumped down and back-filled with helium gas to some pressure less than one atmosphere. The outer chamber of the double dewar is filled with liquid nitrogen. Power is supplied to the two low-wattage heaters to establish a temperature gradient on the sample (usually of the order of two degrees per cm). Establishing a linear gradient along the sample was a matter of some trial and error attempts at varying one or both heater voltages, or turning one or both heaters off and watching the temperature drift, or by increasing or decreasing the transfer gas pressure. Usually a combination of these approaches

was required at each data point. When a linear gradient was obtained, the temperature at each of the four copper-constanin thermocouples was recorded as was the differential EMF generated between TC's 1 and 4, and 2 and 3. Generally no other ΔEMF combinations were measured since the time required was longer than the stable time of the linear temperature gradient.

Below liquid nitrogen temperature, the inner chamber of the double dewar was filled with liquid helium. Temperature control of the sample was more difficult in this region, but the procedure remained the same. A typical data point was calculated as follows:

Switch Position	Function	Mv Reading	Value
1	T_1	-5.3875	82.50°K
2	T_2	-5.3767	83.12°K
3	T_3	-5.3229	86.29°K
4	T_4	-5.3048	87.35°K
7	$\Delta_{EMF}(1-4)$	-0.0095	-1.96 μV/°K
8	$\Delta_{EMF}(2-3)$	-0.0063	-2.00 μV/°K

$$\alpha_{TEP}(Cu) = +1.20$$

thus:

$$\alpha_{TEP}(Abs) = +1.20 + (-1.98) = -0.78 \ \mu V/°K$$

These values were obtained relative to that of copper and so must be corrected by the thermoelectric power of copper. The work of Henry

and Schroeder[48] on copper and copper-alloys was chosen as the reference curve for this correction.

The room temperature apparatus (Figure 28) established a gradient of about 5°K/cm with a mean temperature of about 35°C (308°K). The sample was surrounded by styrofoam insulation and each end was against an iron-constanin thermocouple imbedded in an iron block. One block was fixed in position whereas the second was attached to a threaded screw mechanism allowing samples of varying length to be accommodated. The resulting coefficient measured was relative to that of the iron T.C. leads (+ 11. 0 μV/°K). A typical calculation was as follows:

Switch Position	Function	mv Reading
1	T_1, hot	1.540
2	T_2, cold	1.300
		$\Delta = 0.240$
3	Δ_{EMF} (iron)	-0.054
4	Δ_{EMF} (const)	0.186
		$\Delta = 0.240$

$$\alpha_{TEP} = + 11.00 + \frac{(0.052 \times 10^3)(-0.054)}{(0.240)} = -0.7$$

The Δ_{EMF} in position 4 was measured only as a check for thermal stability during the time that the measurements were being made. In the range of 30 to 40°C, the EMF output of the iron-constanin thermocouple is 0. 052 Mv/°C.

The reproducibility of the measurements of the Seebeck coefficient is quite good for the double dewar-heater apparatus of Figure 27 , approximately ±0. 05 μV/°K, whereas the room temperature equipment realizes only ±0. 5 μV/°K and as such, values around 0. 5 or less are to be suspect.

All specimens measured with these equipment were in the shape of a rectangular solid obtained from the single crystals grown during the course of this thesis. The ends of the samples were cleaved on the (100) planes and the sides were cut or planed within 1 degree of (100) by a spark cutting machine operating under kerosene. Typical sample dimensions were 2mm x 2mm x 12mm.
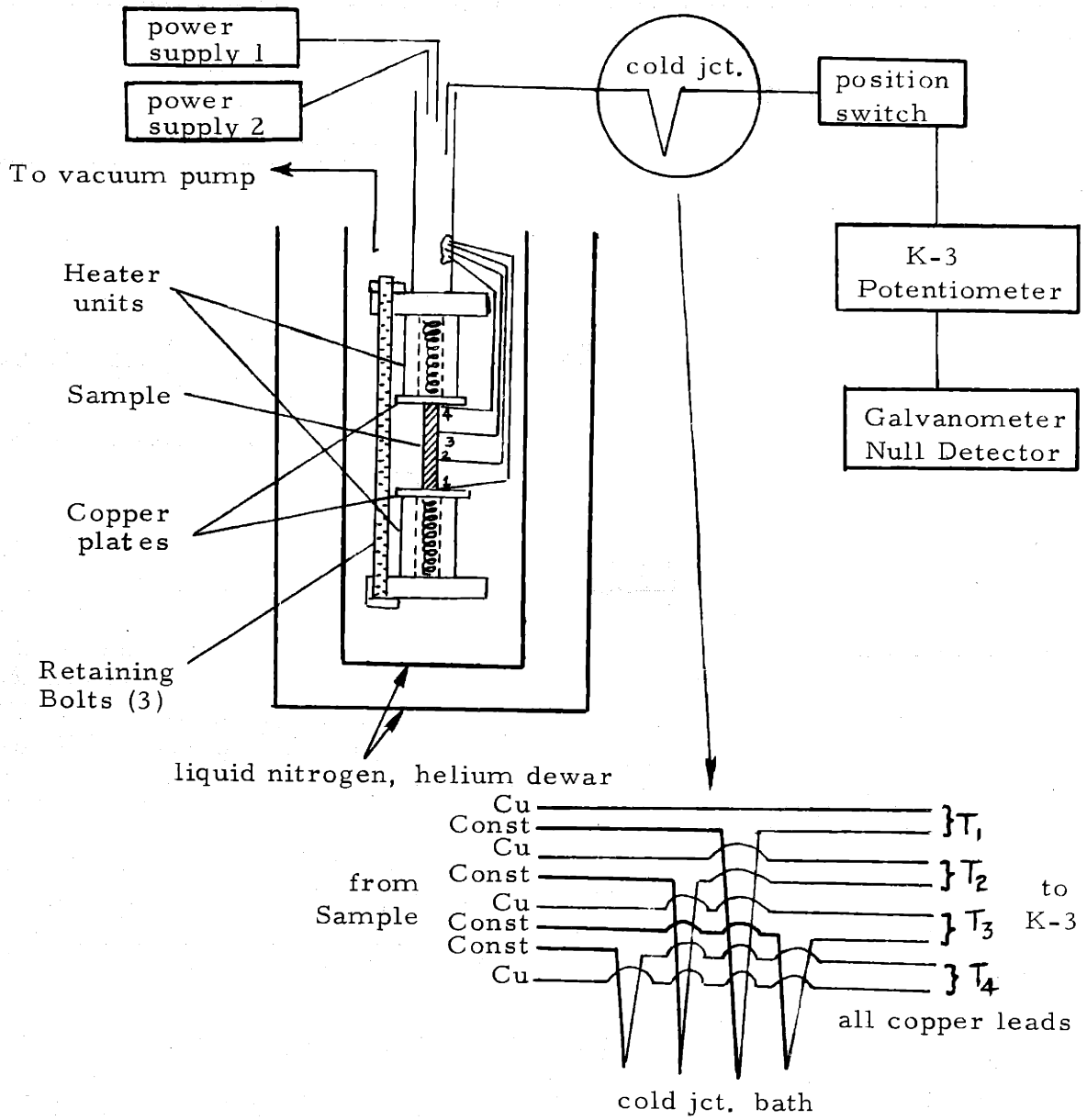
Figure 27   Equipment schematic of Seebeck apparatus used for the
temperature dependence measurements.
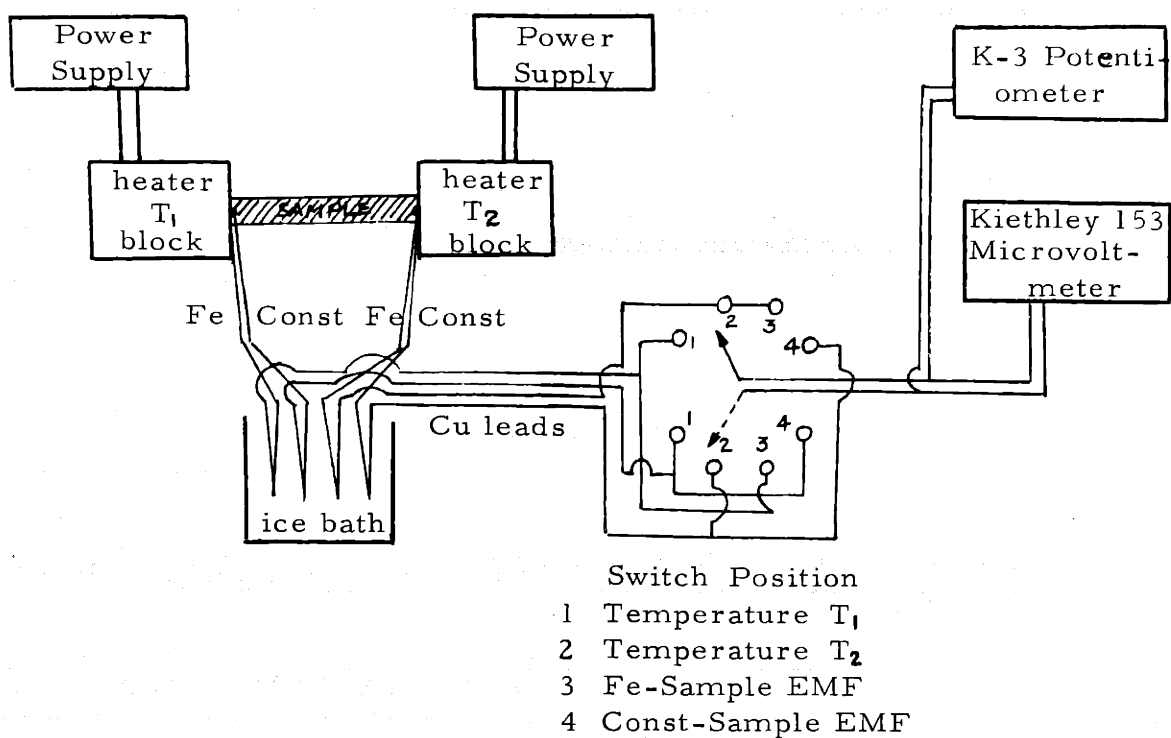
Figure 28a   Block schematic of room temperature Seebeck apparatus
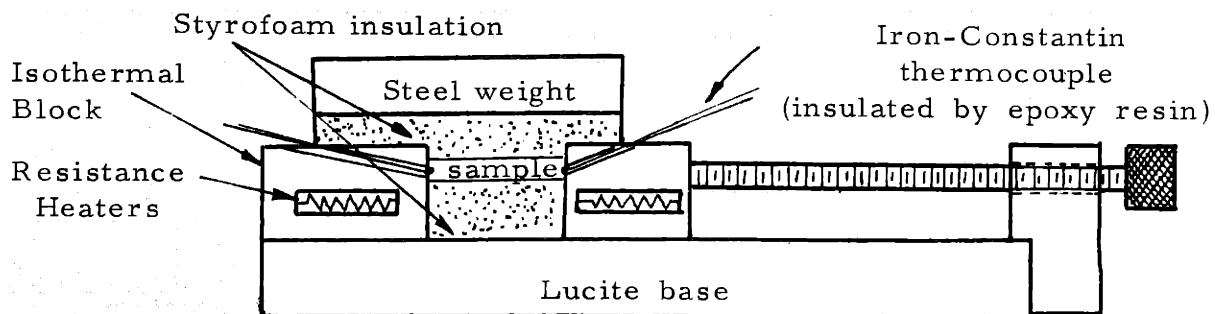
Figure 28b   Sample configuration in the room temperature Seebeck apparatus.

IV.   RESULTS AND DISCUSSION

A.   Resistivity, Magnetoresistivity, and High Field Hall Effect

1.   Electrical Resistivity

The electrical resistivity of NbO_x is shown in Figure 29 as a function of temperature and composition. The variation of resistivity with temperature was determined for only one composition, O/Nb = 0.982; the other samples are assumed to have the same functional variation. The room temperature conductivity is seen to be about 5 x 10^4 $(ohm\text{-}cm)^{-1}$ for the compositions measured. The numerical values of the conductivity of the monoxides of Ti, V, and Nb are of the same order as for solid solutions of oxygen in corresponding metals.[49] This fact has prompted some investigators to consider these oxides as ordered solid solutions or as "interstitial compounds".

The resistivity of NbO_x decreases to about 0.7 µohm-cm around $25°K$ and is constant from there down to 4.2 °K. Considering the sample analysis (see Table 1 for a typical mass spectrographic analysis of niobium monoxide samples) the residual resistivity is most likely due to the impurity content and not to any vacancy scattering mechanism. The resistivity at low temperature (to to $25°K$) exhibits an approximate T^5 dependence, analogous to the behavior of non-transition metal elements.

The resistivity was independent of current used in the measurement, up to 5 amperes.

The room temperature conductivity of NbO_x is an order of magnitude larger than that of TiO, and about thirty times larger than that of VO. One finds also that the resistivity of off-stoichiometric TiO[2] and of all compositions of VO[6] increases with decreasing temperature as though an activation process were involved. The resistivity of NbO_x and $TiO_{1.0}$, however, decreases with decreasing temperature, typical of a normal metal.

TABLE 1

TYPICAL MASS SPECTROGRAPHIC ANALYSIS OF NbO SAMPLES

NbO-641A

Element	ppm	Element	ppm
C	~300	Co	1
N	~400	Ni	—
O	major	Cu	~2
Si	—	Zn	<1
Cl	5	Zr	<2
Ti	—	Nb	major
V	10	Mo	40
Cr	—	Hf	1
Mn	—	Ta	200
Fe	90	W	1
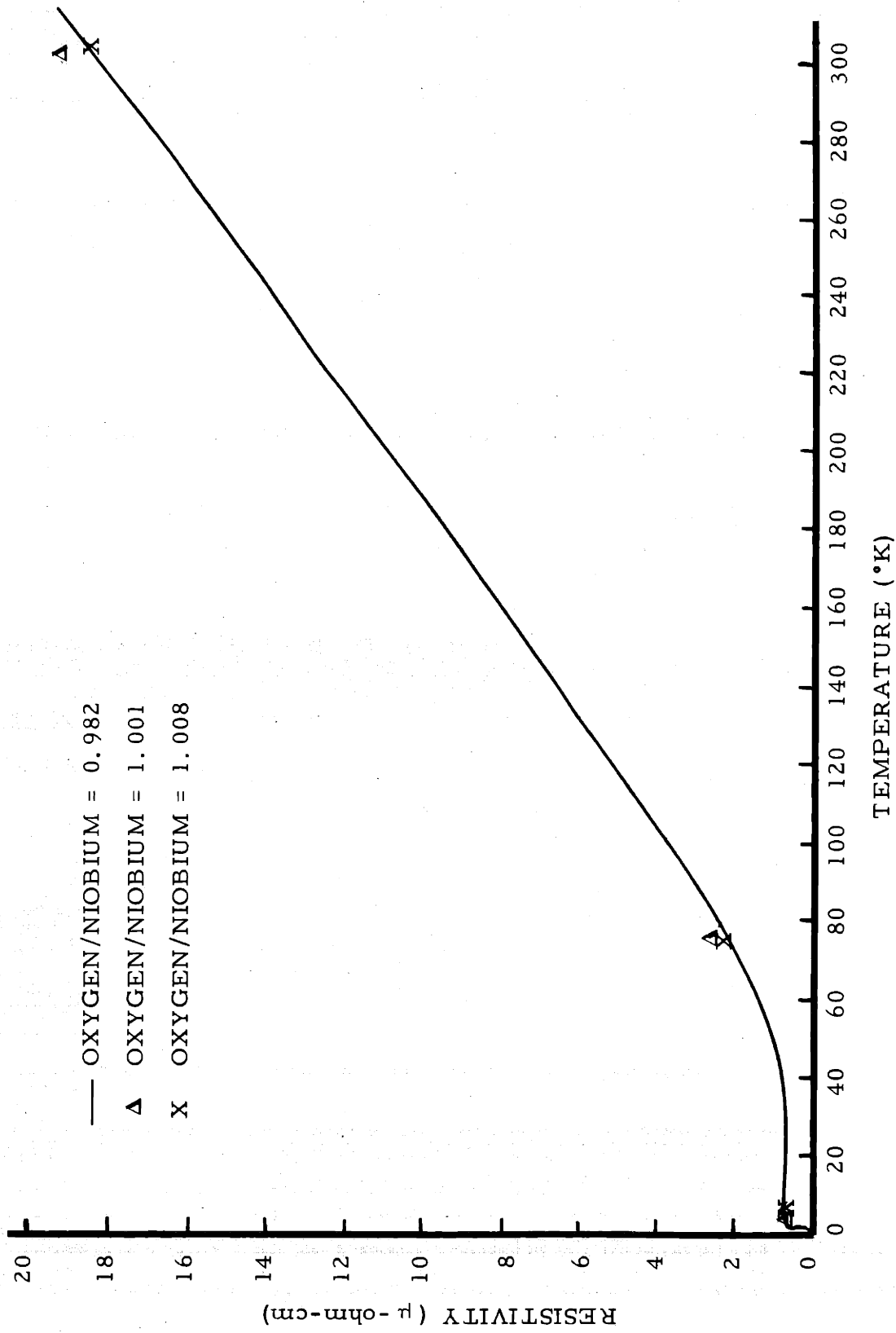
Figure 29   Temperature Dependence of the Electrical Resistivity of NbO_x

2. Magnetoresistivity

The variation of the resistivity with magnetic field (H) is shown in Figure 30 a, b, and c for hypo-, hyper- and stoichiometric samples. The current direction was coincident with the $\langle 100 \rangle$ direction and the magnetic field was oriented parallel to $\langle 010 \rangle$ and then the $\langle 011 \rangle$ directions. Shown in Figure 31 is the magnetic field effect in a general orientation for a O/Nb molar ratio of 0.982. Although in principle, one could map out the magnetoresistance stereogram with a single sample of such an orientation by suitable rotations of the sample [50], it is generally easier to make a series of samples with the desired orientations rather than a complicated rotation mechanism. In Figure 32 is shown the rotational magneto-resistance for the stoichiometric sample oriented with the current parallel to $\langle 100 \rangle$. Several rotation rates were used and due to slippage in the drive mechanism, the results are not as uniform as desirable. Included in the figure are points (designated as +) taken with fixed angles for the magnetic field. Lifshitz [51] states that the width of the maxima as the magnetic field traverses a one-dimensional region of open orbits is inversely proportional to $\overline{\omega_c \tau}$, where ω_c is the cyclotron resonance frequency equal to $\frac{eH}{mc}$ (for free electrons) and τ is the relaxation time. One expects then that the value of $\overline{\omega_c \tau}$ that can be obtained from the peaks in Figure 32 would not be much greater than one. A value of $\omega_c \tau \lesssim 1$ is an indication of not being in the high-field region of the magnetoresistance. With a field of 90 kOe and

a relaxation time of 3.4×10^{-13} sec. (section V), $\omega_c \tau$ is calculated to be ~ 0.7.

The general resistance behavior of a conductor in a transverse magnetic field is illustrated in Table 2. The terms compensated and uncompensated **refer** to whether or not the difference between the number of electrons and holes in the material is zero:

$$n_e - n_h = n.$$

If z_1 (z_2) is the number of electrons of atom 1 (2), and Z_1 (Z_2) is the number of atoms of type 1 (2) in the unit cell, then we may define

$$N_{tot} = (z_1 Z_1 + z_2 Z_2).$$

If N_{tot} is odd then the material is uncompensated, however, if N_{tot} is even, the material may or may not be compensated.

For NbO, we have three atoms of each kind in the unit cell so that N_{tot} (NbO) must be odd and the material should thus be uncompensated.

A summary of the general rules for the behavior of the magnetoresistivity when $\omega_c \tau \gg 1$ would be [50]:

(1) uncompensated; $\dfrac{\Delta \rho}{\rho}$ saturates for a general field direction and quadratic field dependence indicates the presence of open orbits perpendicular to H, but not perpendicular to I, the current flow.

(2) compensated; quadratic field dependence is the general rule with saturation occurring only when open orbits are perpendicular to I.

The type of behavior that was expected for NbO was saturation in most directions, but as can be seen from the figures, saturation did not obtain. Since the quadratic behavior generally seen in this instance is typical of the low field region where $\frac{\Delta\rho}{\rho} \sim H^2$ no matter the state of compensation and since $\overline{\omega_c \tau}$ would not be much greater than one, then an immediate conclusion is that we are not in the high field region.

When $\frac{\Delta\rho}{\rho}$ versus H is plotted in log coordinates, the slopes fall within the range of 1.85 to 2.0, close enough to be considered as an H^2 dependence when the size of the signals measured (a few μvolts) is considered.

Magnetic breakdown results in the appearance of open orbits in directions where normally the orbits would be closed. For O/Nb = 1, when the current vector, I, was parallel to $\langle 100 \rangle$ and the magnetic field was aligned with $\langle 010 \rangle$, there appeared behavior analogous to magnetic breakdown; the same behavior occurred when H was parallel to $\langle 011 \rangle$ for the 1.008 composition (Figures 30b, c). With an estimation of the Fermi energy of about two to four electron volts, we may calculate an approximate energy gap for magnetic breakdown using Blount's equation[52],

$$H_o = \frac{\pi \epsilon_g^2 mc}{2 \hbar e \epsilon_F}$$

where H_o is the apparent magnetic breakdown field ($\sim 10^4$ gauss),

m is the electron mass (assumed to be that of a free electron), and

ϵ_F is the Fermi energy (2 to 4 eV, calculated from the Sommerfeld

FEM using 0.4 electrons/Nb atom obtained from Hall measurements).

Blount's equation results in a calculated gap of between 0.03 and

0.06 eV. The appearance of 'magnetic breakdown' for compositions

greater than the stoichiometric amount would indicate an increasing

number electrons in the compound with a corresponding increase in

the Fermi energy.

However, one of the conditions for the appearance of magnetic break-

down is that $\omega_c \tau \gg 1$, i.e., in the high field region, thus magnetic break-

down must possibly be ruled out in this instance. Although magnetic

breakdown may occur in some materials at the low fields found for the

anomolous behavior of NbO_x, the resistivity ratio $(\rho_{300}/\rho_{4.2})$ is gener-

ally several orders of magnitude larger than that measured here.

The structure of niobium monoxide is simple cubic with three

atoms of each kind in the unit cell, giving a total of eleven outer

electrons per molecule of NbO. A free electron model calculation

yields a Fermi radius of $\sim 0.86 \, |\vec{b}|$ and a Harrison construction [53]

of the Fermi surface leads to a completely filled first zone (electrons),

a centered (at Γ) concave cube hole surface in the second zone, and

rosette shaped ellipsoid (electrons) along the edges of the third

and fourth zones. Cross sections taken on the plane ΓXM (see

Figure 4 for Brillouin zone and point designations) are shown in

Figure 33 for the third and fourth zones. In Figure 34 are shown possible open orbits for magnetic breakdown in the $\langle 010 \rangle$ and $\langle 011 \rangle$ directions deduced from the free electron Fermi surface. The third and fourth zones of the free electron Fermi surface have gaps at the corners of about 0.008 $|\vec{b}|$ between the ends of the ellipsoids, which corresponds to about 0.02 - 0.04 eV, an energy not unlike that obtained from the Blount equation using the value of magnetic field at which the anomolous behavior occurs.

It has been suggested[85] that the type of behavior observed in some of these measurements (apparent magnetic breakdown) is typical of that seen when the voltage probes are attached through superconducting contacts. The copper lead wires were attached with 6-9's indium and the measurements were made at 4.2 °K, a temperature above the superconducting transition temperature of indium. It is also noticed that not all samples exhibited the anomolous behavior, even when the measurement was made with only a change in magnetic field orientation (from $\langle 100 \rangle$ to $\langle 110 \rangle$) on the sample, x = 1.001, that had exhibited the unusual behavior in the previous orientation (Figure 30 b). Further experiments on purer materials are needed for clarification of the behavior seen here.

From these magnetoresistivity measurements we must tentively conclude that we are in the low field region of magnetoresistivity and that increasing oxygen content possibly leads to a small increase in the electron concentration available for conduction.

TABLE 2

GENERAL BEHAVIOR SEEN IN TRANSVERSE
MAGNETORESISTANCE IN THE HIGH-FIELD LIMIT[50]

State of Compensation	Nature of Orbits	Magnetoresistance Behavior
uncompensated	all closed	saturates
compensated	all closed	H^2
either	open orbits in space making angle α with I	$H^2 \cos^2 \alpha$
either	nonintersecting open orbits in 2 different directions	saturates

The result of a magnetoresistance investigation is a stereogram showing directions of field for which the magnetoresistance saturates and for which it is quadratic in field.
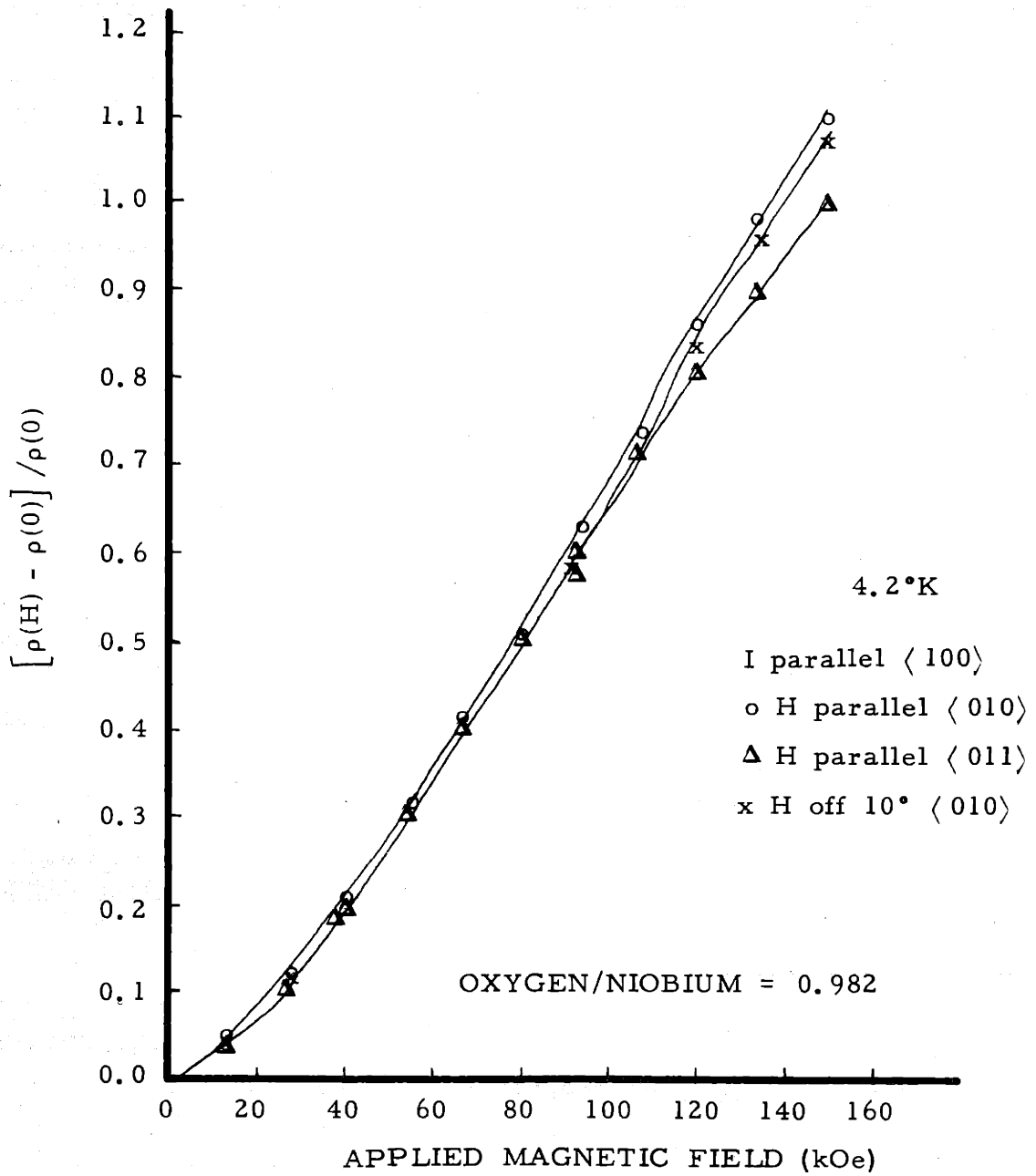
Figure 30a   Magnetoresistivity Behavior for NbO$_{0.982}$
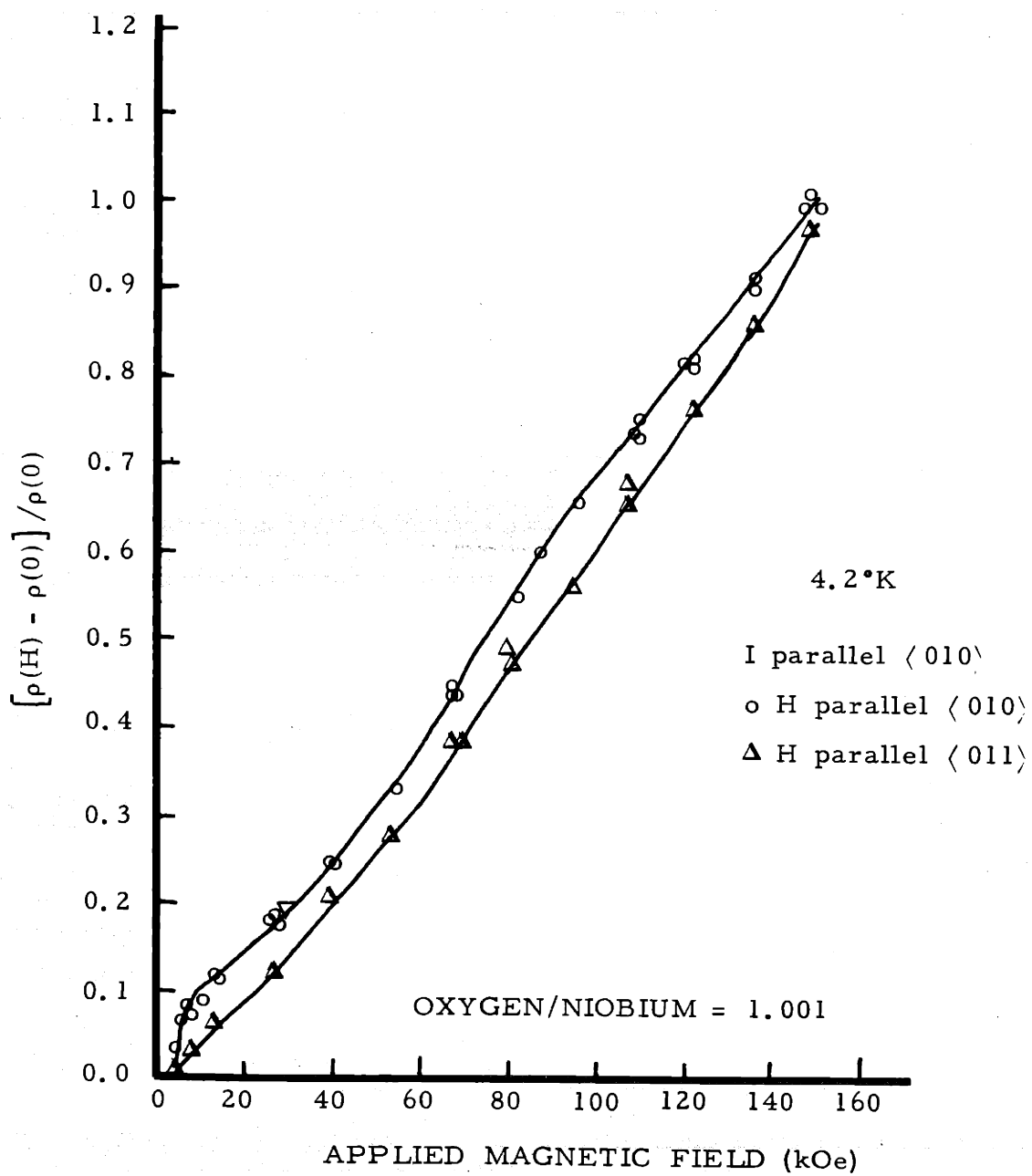
Figure 30b   Magnetoresistivity Behavior for $NbO_{1.001}$
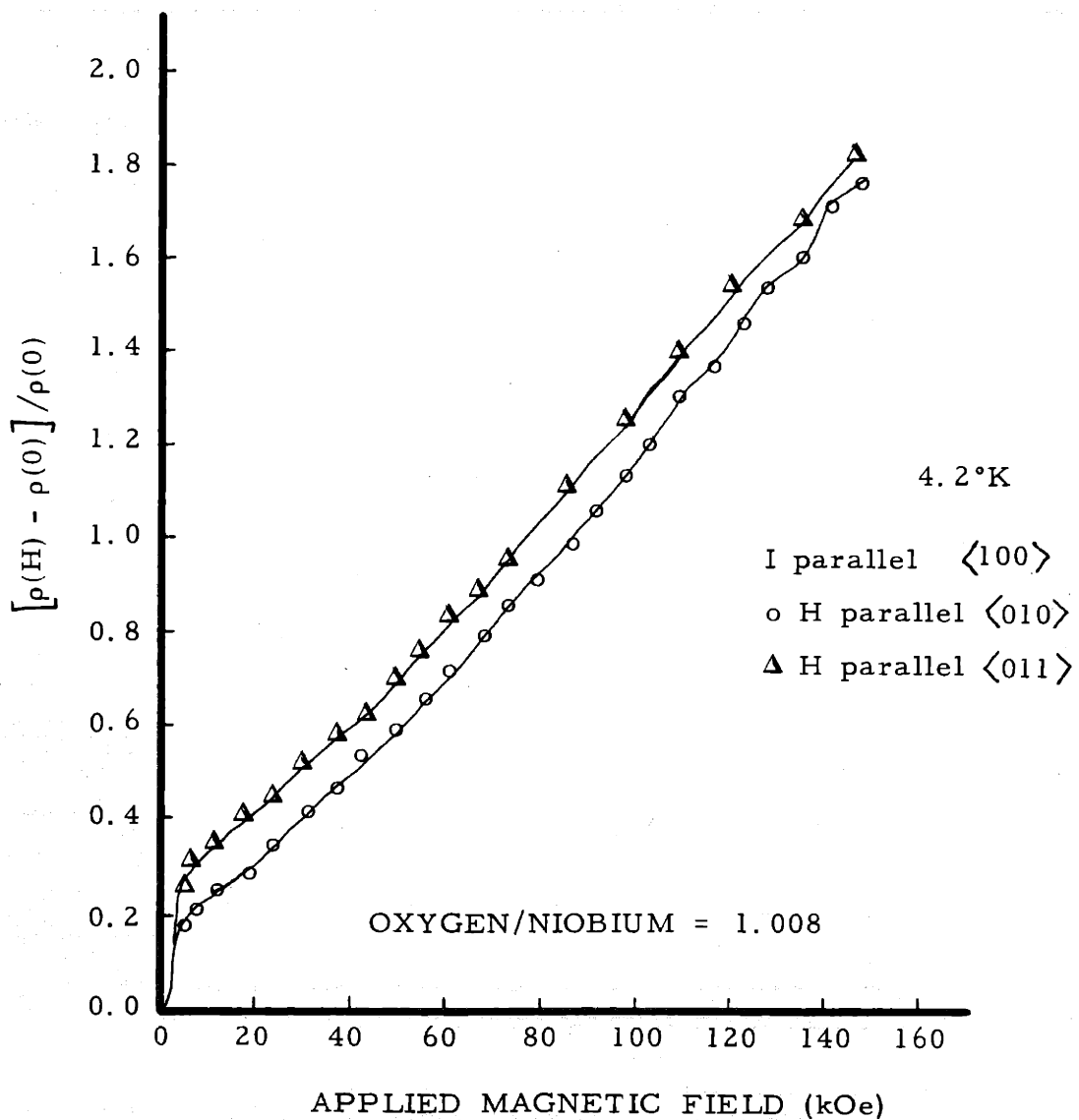
Figure 30c   Magnetoresistivity Behavior for NbO$_{1.008}$
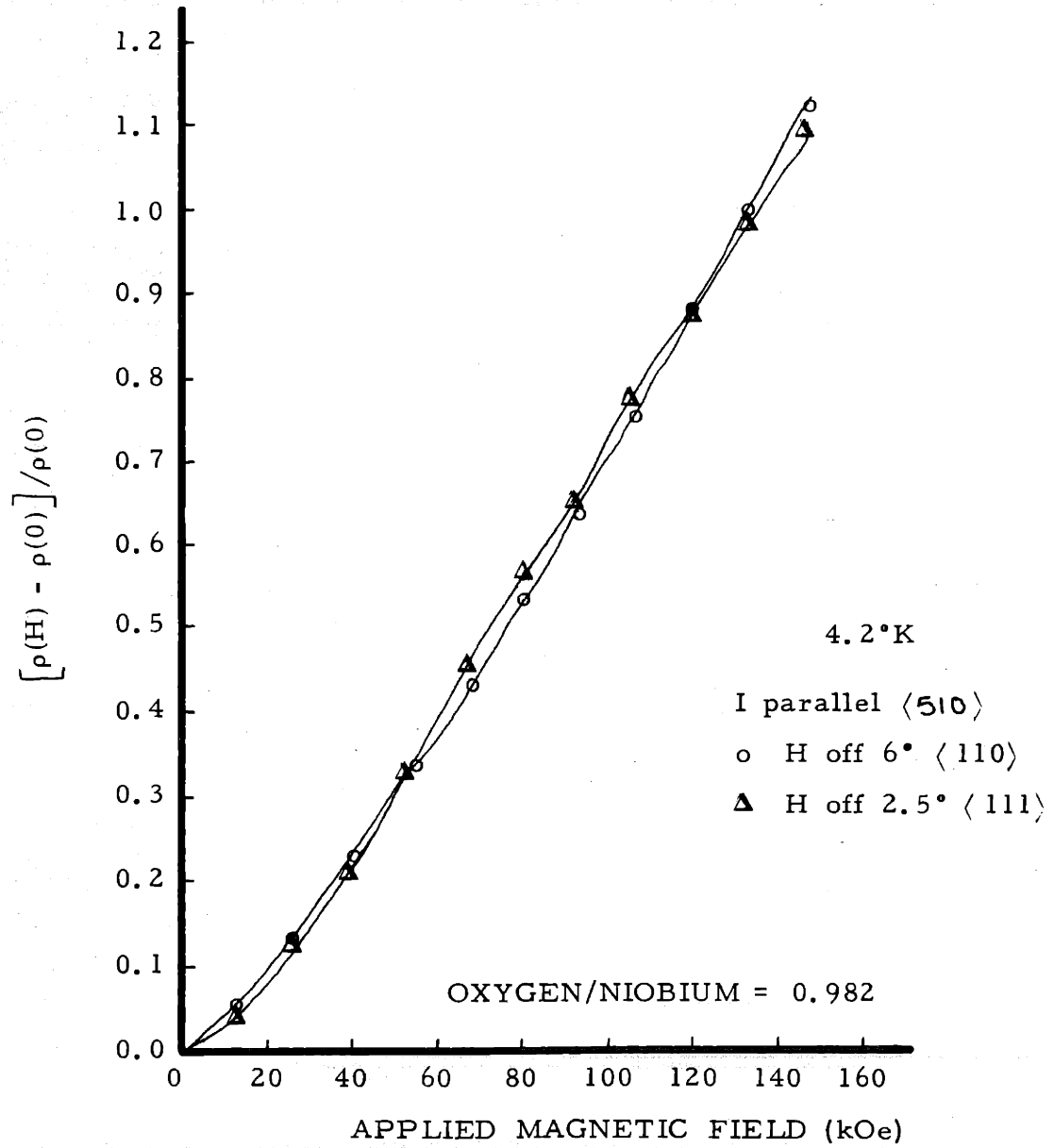
Figure 31   Magnetoresistivity Behavior for a General Direction in a Crystal of $NbO_{0.982}$
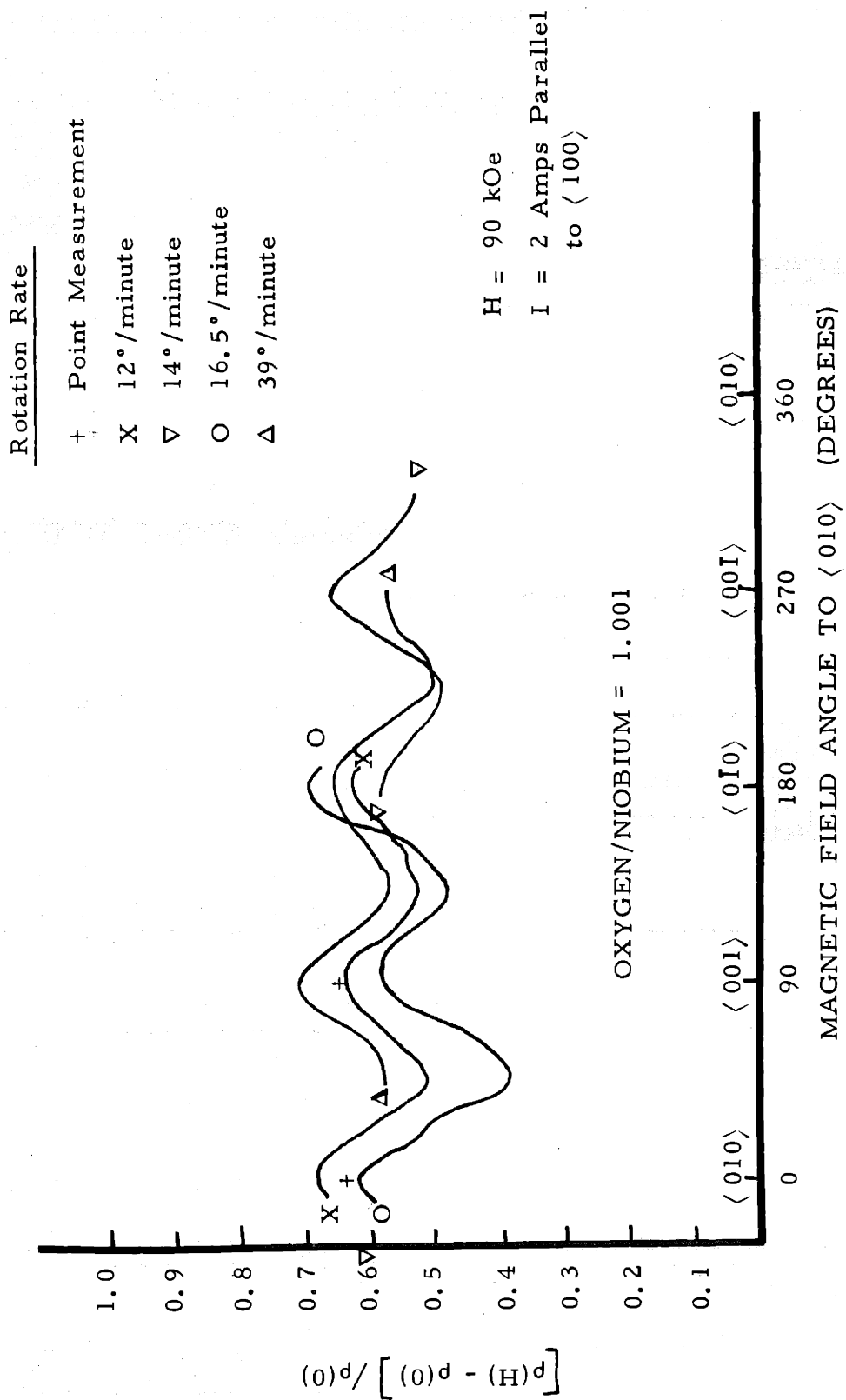
Figure 32   Rotational Dependence of the Magnetoresistance of NbO$_{1.001}$
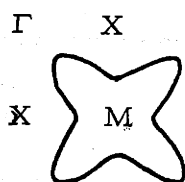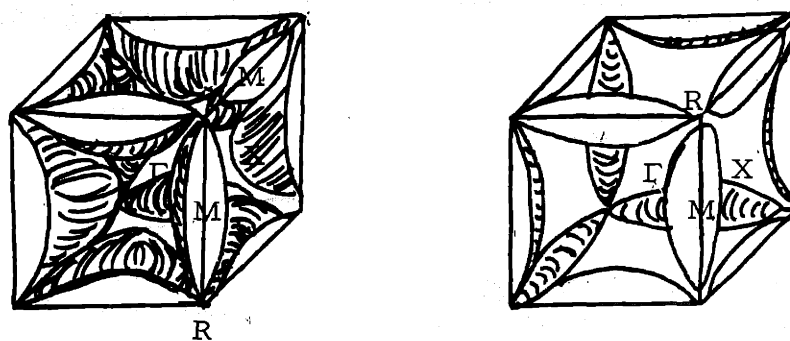
Third Zone Electrons
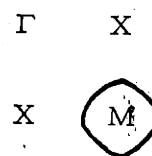
Fourth Zone Electrons

Figure 33   Cross sections of the third and fourth electron zones in the ΓXM plane for a free electron calculation.

(001) FACE OF SIMPLE CUBIC BRILLOUIN ZONE
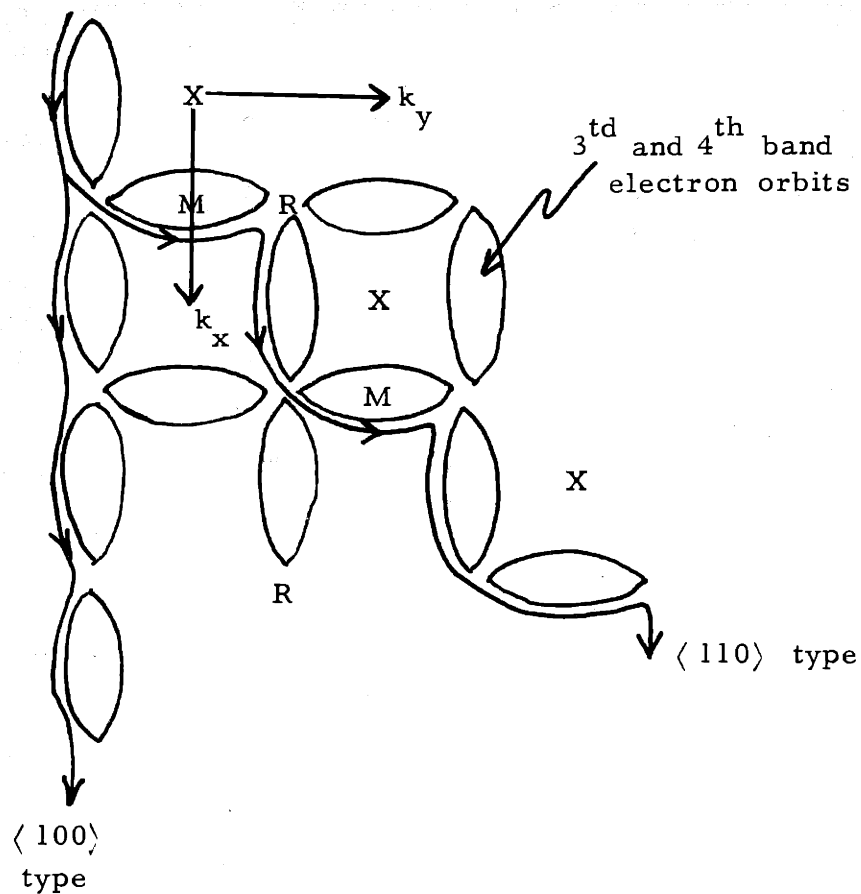
Figure 34   Possible Open Orbits Resulting from Magnetic Breakdown

3. Hall Effect

Hall effect measurements were made at 4.2°K for the stoichiometric compound (x=1.001). The Hall voltage was determined for each of the four combinations of field and current directions (H^+I^+, H^+I^-, H^-I^-, and H^-I^+) and was found to be very small, of the order 1 - 2 μvolts. The applied magnetic field and current were 135 kG and 0.750 amperes respectively. The sample thickness was 0.238 cm and the width was 0.140 cm. The Hall constant calculated from the measurement was therefore 3.9×10^{-4} cm^3/coulomb. The carrier concentration was calculated from the Hall constant and found to be 1.6×10^{22} electrons/cm^3 which is about 0.4 electrons per niobium atom. An effective number of conduction electrons of 0.4 per niobium atom is of the same order as other compounds in the transition metal carbide to oxide group. For instance, titanium carbide [54] has about 0.08 electrons per Ti atom (and $m^* \sim 3m_o$) while titanium monoxide [2] has about one electron per Ti atom (with $m^* \sim 2m_o$).

It is interesting to note from Figure 49 (n_{eff} versus incident photon energy), that two eV is sufficient to create a total particle excitation of 0.4 electrons per Nb atom. Two electron volts is not an unreasonable width for the filled portion of a d band density of states, however, a typical d band filled to this level would contain many more electrons than 0.4/atom and have a larger effective mass

for the electrons than that assumed thus far in the calculations

(assumed free electron mass). The apparent discrepancy in the

expected number and the effective mass of the conduction electrons

to that found in the measurements on NbO_x must be accounted for

in the development of a consistent one-electron energy band scheme

(Section IVG).

B.   Magnetic Susceptibility

The magnetic susceptibility of NbO_x as a function of temperature

and composition was measured by techniques described in Section III B.

The results for the various compositions obtained at three temperatures

(4.2, 77, and 300°K), are shown in Figure 35. The paramagnetic

susceptibility is seen to increase with increasing oxygen content. The

variation with temperature for the compositions shown in Figure 35 is

exhibited in Figure 36. It is seen that the susceptibility decreases with

increasing temperature; the enhancement in the susceptibility at very

low temperature is probably due to impurities with localized moments.

The small values for the paramagnetic susceptibility imply that the con-

duction band is nearly empty or that the effective mass is near to that

of the free-electron value.[2]

The total magnetic susceptibility of a material is made up of several

components:

(1)   A diamagnetic contribution to the ion cores of each type of

       atom present. The core contribution which is often numerically

       larger than that of the conduction electrons, is not easily esti-

       mated with accuracy, but it is temperature independent.

(2)   The outer valence or conduction electrons contribute both a

       diamagnetic and a paramagnetic temperature dependent sus-

       ceptibility. In the free electron case the diamagnetic component

       is one-third of the spin paramagnetism, but this relationship

is not even approximately valid if the effective mass of the

electrons in the lattice differs from that of a free electron.

(3) A temperature independent, Van Vleck, paramagnetic term

due to the mixing of excited state orbital moments with the

ground state moment.

(4) Numerous secondary contributions such as correlation and

exchange effects of the valence electrons.

From Mott,[55] a formulation for the spin paramagnetism is obtained

for a general shape of the density of states:

$$\chi_{Cond}^{Para} = 2\mu^2 \, n(\epsilon_F) \left\{ 1 + \frac{\pi^2}{6} \, k^2 \, T^2 \left(\frac{\partial^2 \ln n(\epsilon)}{\partial\epsilon^2} \right)_{\epsilon = \epsilon_F} \right\} \quad (1)$$

Where μ is the electronic magnetic moment, $n(\epsilon_F)$ is the state density

of the Fermi level, k is the Boltzman constant, and T is the absolute

temperature. This equation may be put into a more convenient form.

$$\chi_{Cond}^{Para} = 2\mu^2 \, n(\epsilon_F) \left\{ 1 + \frac{\pi^2}{6} \, k^2 \, T^2 \left[\frac{1}{n(\epsilon)} \frac{\partial^2 n(\epsilon)}{\partial\epsilon^2} \right. \right. -$$

$$\left. \left. - \left(\frac{1}{n(\epsilon)} \frac{\partial n(\epsilon)}{\partial\epsilon} \right)^2 \right]_{\epsilon = \epsilon_F} \right\} \quad (2)$$

If the assumption is made that the ion core diamagnetism is essentially

independent of temperature and that the conduction electron translational

diamagnetism has about the same functional dependence on temperature

as that of the spin paramagnetism, then the apparent temperature variation of the magnetic susceptibility of NbO_x places the Fermi energy at or near a maximum in the density of states. At a maximum in the density of states,

$$\left. \frac{\partial n(\epsilon)}{\partial \epsilon} \right|_{\epsilon_F} = 0,$$

and

$$\left. \frac{\partial^2 n(\epsilon)}{\partial \epsilon^2} \right|_{\epsilon_F} < 0$$

so that $\partial X/\partial T$ will be less than zero, assuming the validity of Equation (2) above. The interpretation of Mott's formula that $\partial X/\partial T < 0$ requires that little or no change occurs in the Fermi energy or density of states with temperature.

Kriessman and Callen[56] have correlated empirical data for the temperature dependence of the magnetic susceptibility of transition metals and their alloys and found that $\frac{\partial X}{\partial T} > 0$ (< 0, the NbO_x case) when the Fermi level lies at or close to a minimum (maximum) in the density of states. If $\epsilon_F (0)$, the Fermi energy at $T = 0$, occurs at a small depression in an overall maximum of $n(\epsilon)$, the susceptibility would show an increase initially at low temperature with the subsequent decrease due to the overall maximum. The susceptibility would then show a maximum at very low temperatures. If the niobium $d\text{-}t_{2g}$ band is truly symmetrical one might expect some separation of the anti-bonding from the bonding states. In the case of NbO, the two peaks in

the density of states expected from the bonding and antibonding portions

of the t_{2g} band are apparently merged.

A breakdown of the components of the magnetic susceptibility would

be as follows:

$$\chi_{obs} = \chi_{core}^{dia} + \chi_{Landau}^{dia} + \chi_{spin}^{para} + \chi_{Van\ Vleck}^{para} \tag{3}$$

An estimate of $\chi_{core}^{dia} \approx -20 \times 10^{-6}$ emu/mole of Nb atoms is provided

by Geballe et al.[57] By using a free electron formulation,[55] the con-

duction electron spin paramagnetism may be calculated:

$$\chi_{cond}^{para}\ (F.E.M.) = 1.88 \times 10^{-6}\ n^{1/3}\ \left(\frac{A}{\rho}\right)^{2/3}\ \text{emu/mole}$$

where n is the number of conduction electrons per molecule, A is the

atomic weight of the molecule, and ρ is the density of the compound in

grams/cm^3. The measured density of $NbO_{1.0}$ is 7.24 gr/cc,[58] the

atomic weight is 108.91, and n should be between one and three electrons

per molecule (per niobium atom). Thus:

$$\chi_{cond}^{para}\ (F.E.M.) = +\ 11.5\ \text{to}\ +\ 16.5\ \times\ 10^{-6}\ \text{emu/mole}.$$

The diamagnetic contribution of the conduction electrons will then be

$-\frac{1}{3}\left(\frac{m}{m^*}\right)^2\ \chi_{cond}^{para}$; with the assumption that $m = m^*$, then:

$$\chi_{cond}^{dia}\ (F.E.M.) = -\ 3.8\ \text{to}\ -\ 5.5\ \times\ 10^{-6}\ \text{emu/mole}$$

The observed room temperature susceptibility for $NbO_{1.0}$ (Figure 35)
is about 98×10^{-6} emu/mole, thus we may calculate:

$$\chi_{Van\ Vleck}^{para} = +\ 110\ to\ 107 \times 10^{-6}\ emu/mole.$$

From the value of the Van Vleck paramagnetism we should be able to

estimate the amount of 'd' electrons involved per niobium atom in the

conduction band.

In the case of niobium nitride, Geballe et al[57] estimate that 1/3

to 1/2 4d electrons in the conduction band per niobium atom gives rise

to a Van Vleck term of about 40×10^{-6} emu/mole. Here then in the

case of NbO, we may have about one 4d electron per niobium atom to

account for an apparent Van Vleck paramagnetism of $\sim 100 \times 10^{-6}$ emu/

mole.

For comparison with the behavior of NbO_x, a short description of

the behavior of TiO_x and VO_x follows.

In Figure 37 is shown the composition dependence of the magnetic

susceptibility of TiO_x.[2] Included on the figure are the symbols

denoting the slope of χ vs T. Note that all the off-stoichiometry sam-

ples had a slightly increasing susceptibility with increasing temperature,

whereas the 1:1 molar ratio sample maintained an apparent zero slope.

If a free electron-like behavior is assumed for the conduction electrons,

then this result is fairly consistent with the APW calculations of Ern

and Switendick[28] and their placement of the Fermi level near a rela-

tive minimum (Figure 2).

The temperature dependence of $VO_x^{(5)}$ is shown in Figure 38 for several O/V molar ratios. Apparently VO_x goes antiferromagnetic with an increasing Neel temperature with increase in oxygen content for compositions above O/V = 1.0. Above 77°K, the samples obeyed a Curie-Weiss law with an increasing μ_{eff} with the decrease in vanadium content. The increase in μ_{eff} is probably due to an increase in the number of localized vanadium d electrons. Such a behavior is possibly explained by the assumption of a half-filled, split $d-t_{2g}$ conduction band in the one electron energy band picture.

All of the niobium monoxide samples contained up to 100 ppm atomic of Fe, Ta, and W and as such with their associated paramagnetic moment could exhibit a large influence on the overall susceptibility at very low temperatures. A rudimentary calculation using a Curie law for localized moments which gives rise to a paramagnetic susceptibility contribution of $\chi_{imp} = Ng^2 J (J + 1) \mu^2/3kT$, gives a value of approximately 3×10^{-6} emu/gram of NbO at 4°K, and about 1×10^{-6} at 10°K. The values used for the calculation were: 100 ppm atomic of iron yields $\sim 12 \times 10^{17}$ atoms Fe per gram of NbO; $g = 2$; $\mu = 2(9.27 \times 10^{-21})$; $J = 1$; and k is the Boltzman constant, 1.38×10^{-16}.

Though localized moments could account for most of the low temperature behavior, the effect is quenched very quickly and thus does not negate the overall decrease in magnetic susceptibility with temperature. The use of the Curie law implies that the measuring field (10 kG) is either sufficiently strong so that very long range interactions between the iron

atoms can occur or that the iron localized moment interacts weakly with the conduction electrons via some exchange interaction and polarizes the conduction electrons slightly.

Some general statements about the appearance of localized moments are appropriate here:[59]

(1) The localized spin moment appears when the intra-atomic exchange energy, or $(U + 4J)$, where U is the intra-atomic coulomb energy and J is the intra-atomic exchange energy, is sufficiently large compared with the width of the localized virtual level, Δ. A small density of states for the conduction band and small matrix elements for the s-d admixture make Δ small, thus favoring the appearance of the localized moment. When the conduction band is entirely d-like, then the virtual levels tend to be more spread out but a peak in the energy distribution of the levels still persists, the width of this peak must be small to obtain localized moments.

(2) The number of electrons in the localized states of the d-shell is an eminent factor for the presence or absence of the localized moment. A nearly half-filled d-shell is most favorable for the appearance of the moment, while nearly filled or nearly empty d-shells seldom have spin moments (for instance, dilute Ni impurity atoms in noble metals show no localized moment while Cr, Mn, and Fe impurity atoms show localized moments in all noble metals).

(3)   When the localized spin moment does appear, it usually has

a fairly large value, or a substantial fraction of its saturation

value.

The second and third points are perhaps of particular interest in rela-

tion to the magnetic behavior of NbO_x.   Were it not for the fact that

all compositions in the single phase field exhibited an increased sus-

ceptibility at very low temperatures, the introduction of niobium $(4d^4, 5s^1)$

into a niobium non-bonding site $(0, 0, 0)$ could be considered to create

localized levels in the conduction band and to cause the enhanced sus-

ceptibility but only for $O/Nb < 1$.   Perhaps the introduction of levels from

non-bonded niobium atoms do play a role in the properties of the low

oxygen content samples $(x < 1)$, at least to some extent.   The considera-

tion of isolated energy levels will be discussed in the development of

the one electron energy band scheme (Section IV^G).
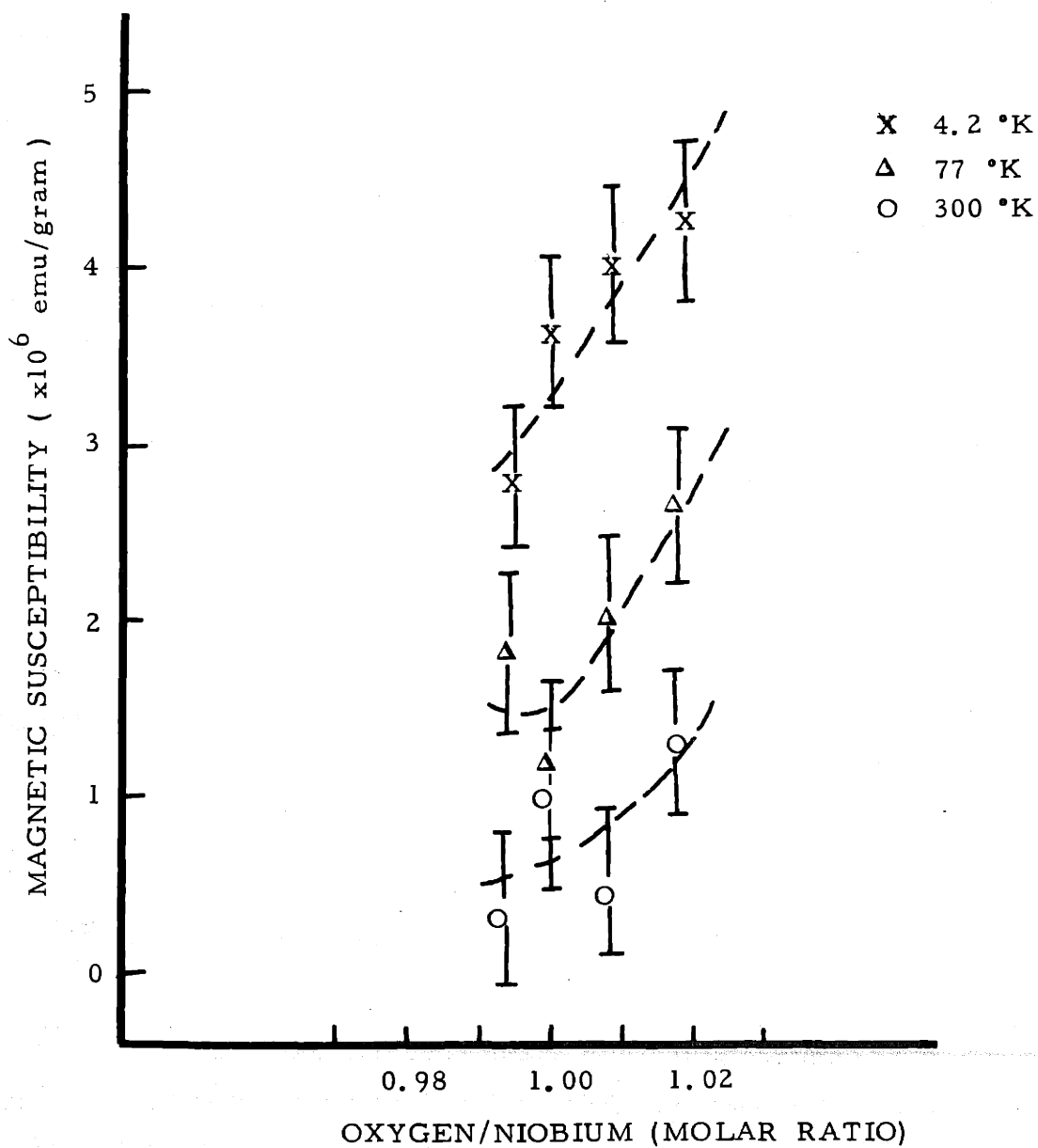
Figure 35 Compositional Dependence of the Magnetic
Susceptibility at Liquid Helium, Liquid Nitrogen,
and Room Temperature
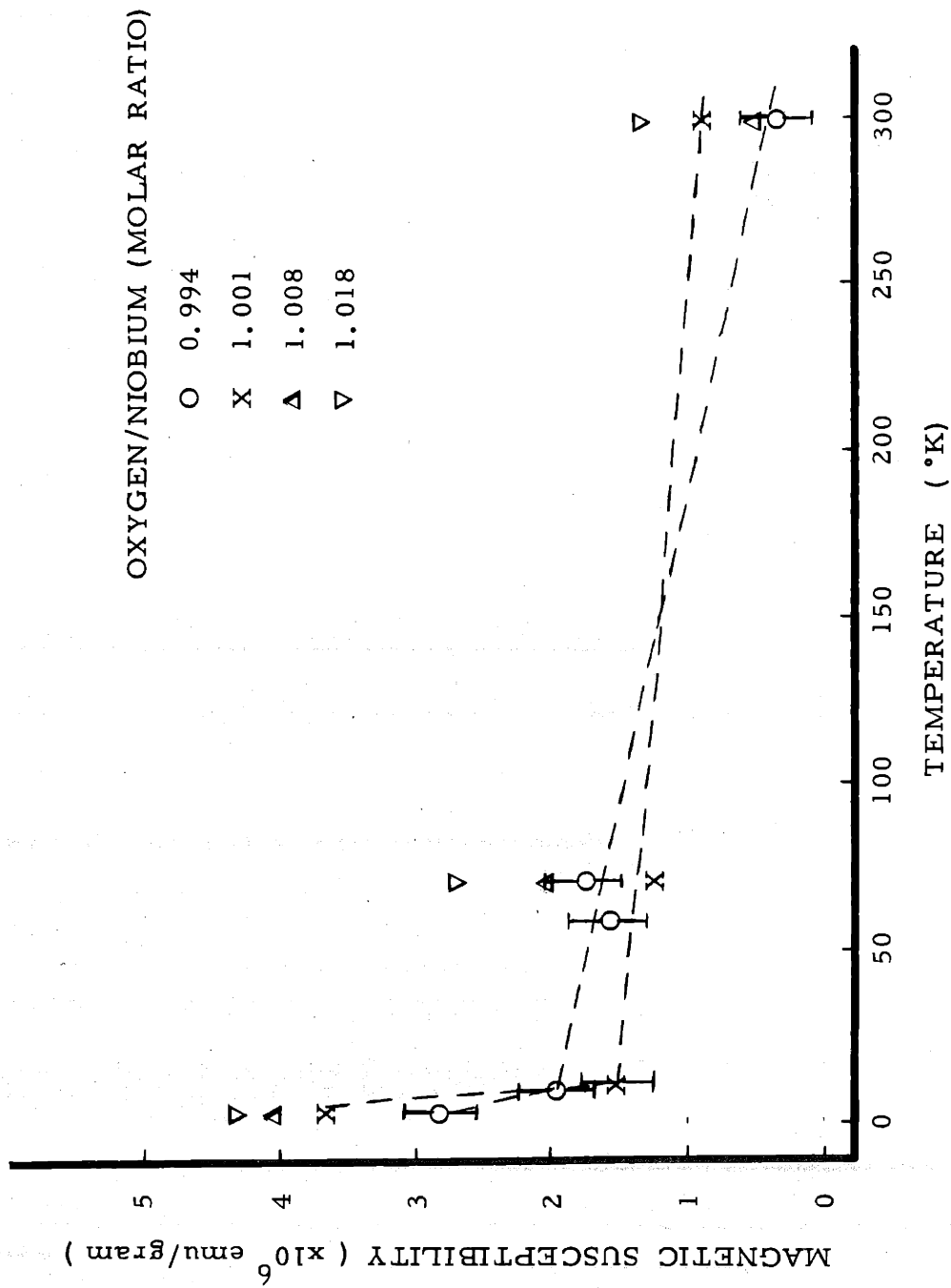
Figure 36   Temperature Dependence of the Magnetic
Susceptibility of NbO$_x$

C. Thermoelectric Power

The determination of the Seebeck coefficient as a function of composition in the niobium-oxygen equiatomic region has been accomplished, see Figure 39. The temperature dependence for the stoichiometric composition, $NbO_{1.001}$, has been determined from 25°K to 300°K (Figure 40).

The use of the Hall effect measurement in the characterization of electronic materials is well known, however, the importance of the thermoelectric power in the determination of material characteristics has often been overlooked. This in spite of the fact that formulations were derived early by Mott[55] and by Wilson,[60] and significant information could have been obtained about the position of the Fermi level, the mean free path dependence on energy, or even the density of states at the Fermi level. The problem seems to have been the paradoxical situation where the Hall effect exhibited particle characteristics whereas the Seebeck coefficient was measured to be positive, implying hole characteristics i. e., the cases of the noble metals Cu, Ag, and Au, and the alkali metal Li.[61] These metals were believed to be free electron-like and thus should have exhibited electron characteristics, i. e., negative values should obtain for both Hall and Seebeck measurements. The Seebeck value is very sensitive to "phonon drag" and impurity effects, as in the case of copper,[48] but these same effects show that the measurement involves the determination of the relaxation time-energy dependence, or the scattering mean free path. In a simple free

electron, single band, model, it is found that if the relaxation time $\tau(\epsilon)$ or mean free path, λ, decreases with increasing energy $(\partial\lambda/\partial\epsilon)_{\epsilon F} < 0$, the Seebeck coefficient is positive while the Hall constant may still be negative according to the dependence on energy of the ratio of the carrier concentrations and their respective mobilities.[55]

Referring to Figure 40 , which shows the temperature dependence of the Seebeck coefficient for the 1:1 molar ratio composition, one sees that there is a low temperature enhancement of the thermoelectric power due either to the presence of about 100 ppm iron impurity or to a negative phonon-drag component. The presence of 0.0001 atom percent (100 ppm) iron in copper is known to cause a decided change to more negative values of the diffusion thermopower.[48] Because of the difficulty in maintaining a stable temperature gradient in the NbO samples at temperatures near the helium boiling point, very low temperature data is lacking in quantity as well as quality. Insufficient data makes it unrealistic to attempt to calculate a phonon or impurity effect on the low temperature values.

A qualitative sketch one obtains of the temperature dependence of the components of the thermoelectric power of NbO is the following:
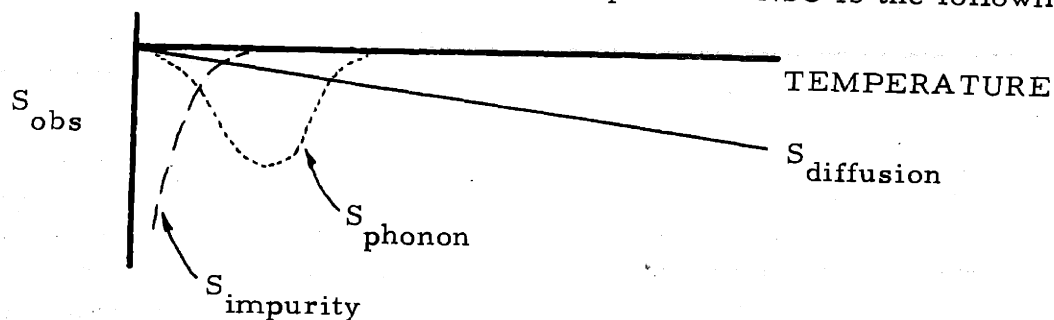
The assumed linear component of the Seebeck coefficient may be analysed using the free electron formula[55]

$$S_d = \frac{\pi^2 k^2 T}{3 e E_F} q = -\frac{2.45 \times 10^{-2} T \, (°K)}{E_F \, (eV)} q \quad (\mu V/°K) \qquad (1)$$

where q is determined by the energy dependence of conductivity; for free electrons, $n \sim E^{1/2}$, $v \sim E^{1/2}$, so

(a) $q = 1$ if $v\tau \, (= \lambda)$ is a constant independent of E,

(b) $q = 1 + x$ if $\lambda \sim E^x$,

(c) $q = \frac{3}{2} + y$ if $\tau \sim E^y$.

The room temperature (300°K) Seebeck coefficient is seen to be about -0.70 $\mu V/°K$ and this would indicate a Fermi energy of about + 10.5 (q) in electron volts. For any reasonable q, this value is anomolously large for a transition metal oxide and so such a simple description of the thermopower is inadequate. Since the oxygen 2s and 2p bands should be completely separated from the niobium d bands, the Fermi energy value that could be obtained from the thermoelectric power should be approximately one half the width of the lower d conduction band (the t_{2g} portion of a one-electron energy band scheme would contain three electrons in six states since the other valence electrons would be used in filling the lower oxygen s and p bands).

In Figure 41a and b, is shown the Seebeck coefficient of TiO_x and VO_x. The thermoelectric power of TiO_x measured at 300°K,[2] is seen to exhibit negative values at low oxygen to titanium ratios

(- 1 $\mu V/°K$ at O/Ti = 0.62) but increasing to low positive values in

the O/Ti range of 0.66 to 0.88 whereupon the Seebeck coefficient goes

negative again decreasing to -12 $\mu V/°K$ at O/Ti = 1.25. The thermo-

electric power of VO_x was measured by Steinitz[6] and was found to

start at -8 $\mu V/°K$ at low O/V ratio (~ 0.8) going through zero near the

1:1 ratio and increasing in positive value to + 30 $\mu V/°K$ at O/V = 1.28.

A qualitative comparison of the Seebeck coefficients for TiO_x, VO_x,

and NbO_x as a function of oxygen/transition metal ratio is shown below.
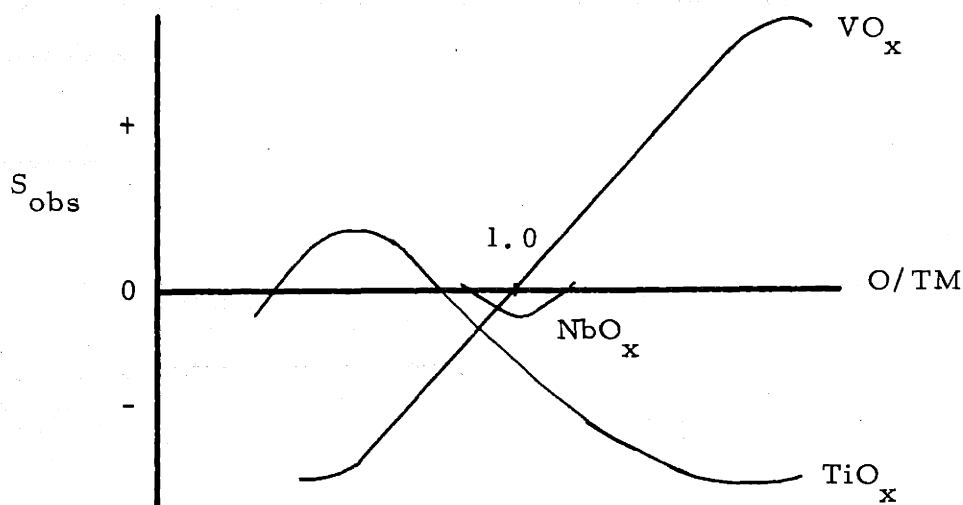
Steinitz,[6] and Goodenough[62] believe that the positive Seebeck

coefficient at high O/V ratios is definitely connected with the anti-

ferromagnetic behavior of VO_x, for $x \geq 1.0$.[5] The antiferromagnetic

behavior for x > 1 and the zero Seebeck coefficient at x = 1, may be

understood by the assumption of a deep minimum, almost a complete

splitting, in the metal-metal d-t_{2g} band i.e., the band has separated

into definitive bonding and antibonding portions.

Regarding the compositional dependence of the thermoelectric power of NbO_x, Figure 39 shows the results obtained at room temperature ($\overline{T}$ = 300°K). As noted in Section IIIB, the Seebeck coefficient measured in the room temperature apparatus is known to only ± 0.5 $\mu V/$°K, so it is questionable whether the high and low 0/Nb ratio samples have small positive values. Of primary importance is the qualitative result of a minimum in the Seebeck coefficient near to the stoichiometric ratio. Assuming that each of the compositions would have a similar temperature dependence of the thermopower excepting perhaps a perturbation expected from defect scattering effects, then we note that a simple free electron formula such as Equation (1) is not applicable for the calculation of the Fermi energy variance with composition. The use of such a formula would indicate an abnormally large change in the conduction band width for a small change in composition, an occurance which one would think to be incommensurate with the type of d-electron energy bands one expects to find in transition metal compounds. What may be said of the compositional dependence of the Seebeck coefficient is that the scattering mean free path is strongly affected by deviations from stoichiometry.

Lye[63] has considered the compositional dependence of the thermoelectric power in TiC_x making use of a suggestion by Mott[64] that in transition metals and transition metal alloys that the current is carried by s electrons but that the relaxation time is inversely proportional to the overlapping available d band density of states into which scattering

could occur. From Wilson[60] we obtain for single conduction band effects,

$$S = \frac{\pi^2 k^2 T}{3e} \left\{ \frac{\partial}{\partial \epsilon} \ln \left[n(\epsilon) v^2(\epsilon) \tau(\epsilon) \right] \Big|_{\epsilon = \epsilon_F} \right\} \tag{2}$$

If we assume $n_1(\epsilon) \sim \epsilon^{1/2}$, $v_1(\epsilon) \sim \epsilon^{1/2}$, and $\tau_1(\epsilon) \sim \dfrac{1}{n_2(\epsilon)}$, then this results in

$$S = -\frac{\pi^2 k^2 T}{3|e|\epsilon_F} \left[\frac{3}{2} - \frac{\epsilon}{n_2} \frac{\partial n_2}{\partial \epsilon} \Big|_{\epsilon_F} \right] \tag{3}$$

thus $S \lessgtr 0$, when

$$\frac{\partial n_2}{\partial \epsilon} \Big|_{\epsilon_F} \lessgtr \frac{3 n_2(\epsilon_F)}{2 \epsilon_F}$$

Looking at a qualitative picture of the d band (subscript 2 is to refer to a d band) density of states, we see
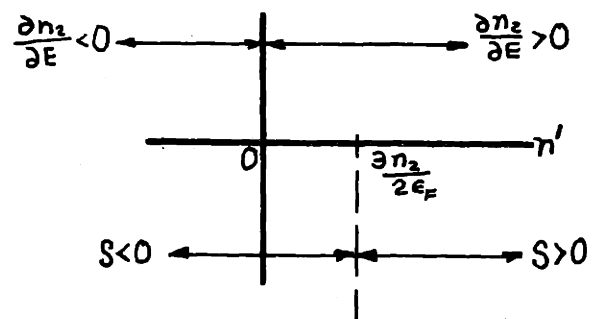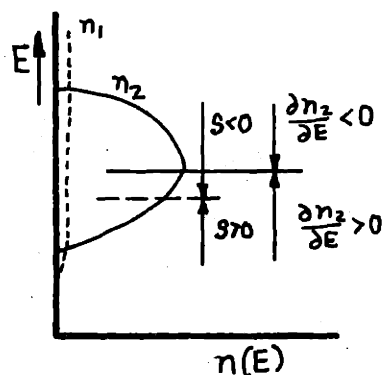
This picture is almost diametrically opposed to the conventional one for a _single_ band of that general shape; a band less than half-filled should have $S < 0$ whereas when more than half-filled, hole behavior should dominate. None the less, with the two overlapping bands, one with a low density of states and the other with a high density of states, that are considered here, the behavior is not improbable.

If we let x in this case (i.e., the case of $\tau_1 \sim 1/n_2$) be the X/TM ratio, then

$$\frac{\partial S}{\partial x} = \frac{\pi^2 k^2 T}{3e} \frac{\partial}{\partial x} \left[\frac{3}{2\epsilon} - \frac{1}{n_2(\epsilon)} \frac{\partial n_2(\epsilon)}{\partial \epsilon} \right]_{\epsilon = \epsilon_F}$$

$$= \frac{\pi^2 k^2 T}{3e} \left\{ -\frac{3}{2\epsilon^2} + \frac{1}{n_2^2(\epsilon)} \left[\frac{\partial n_2(\epsilon)}{\partial \epsilon} \right]^2 \right.$$

$$\left. - \frac{1}{n_2(\epsilon)} \frac{\partial^2 n_2(\epsilon)}{\partial \epsilon^2} \right\}_{\epsilon = \epsilon_F} \frac{\partial \epsilon_F}{\partial x}$$

$$= - \frac{\pi^2 k^2 T}{3|e|} \left\{ -\frac{3}{2\epsilon_F^2} + \left(\frac{n_2'}{n_2^2} - \frac{n_2''}{n_2} \right) \bigg|_{\epsilon_F} \right\} \frac{\partial \epsilon_F}{\partial x}$$

The primes denote the order of partial differentiation with respect to energy. Lye arrived at the same result but in another form:

$$\frac{\partial S}{\partial x} = - \frac{\pi^2 k^2 T}{3|e|} \left[- \frac{3}{2 \epsilon_F^2} - \frac{\partial^2 \ln n_2(\epsilon)}{\partial \epsilon^2} \Bigg|_{\epsilon_F} \right] \frac{\partial \epsilon_F}{\partial x}$$

This result though equivalent is less easy to visualize in a qualitative manner.

From Equation (4), if at or near a maxima (minima) in the density of states:

$$n_2' \approx 0$$

$$n_2'' \stackrel{<}{(>)} 0$$

$$\frac{\partial S}{\partial x} \approx \not\gtrless \frac{\pi^2 k^2 T}{3|e|} \left[\not\gtrless \frac{3}{2 \epsilon_F^2} \not\gtrless \frac{n_2''}{n_2} \Bigg|_{\epsilon_F} \right] \frac{\partial \epsilon_F}{\partial x}$$

if $\partial \epsilon_F / \partial x > 0$ (which is the situation in TiC_x, according to Lye), then

$$\frac{\partial S}{\partial x} \lessgtr 0$$

when

$$n_2'' \Bigg|_{\epsilon_F} \stackrel{<}{>} - \frac{3 n_2(\epsilon_F)}{2 \epsilon_F^2}$$

and we have the following qualitative behavior.
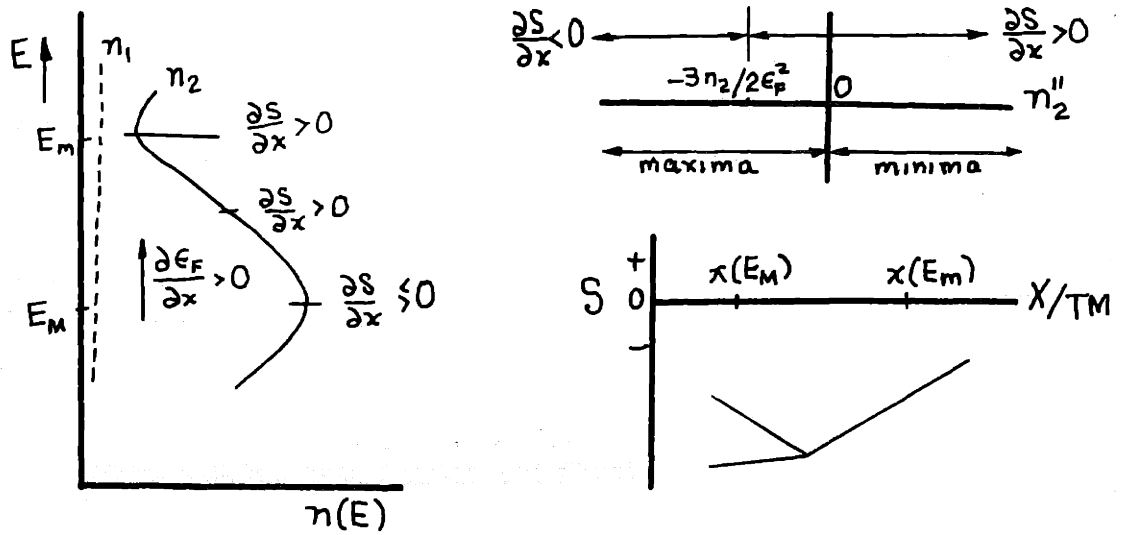
We see that near the maximum, $\partial S/\partial x$ may be greater or less than zero depending on the actual values of the derivatives. If we have the condition $\partial \epsilon_F/\partial x < 0$, then the qualitative picture is reversed:

$$\frac{\partial S}{\partial x} \lessgtr 0, \quad \text{when} \quad n_2'' \Big|_{\epsilon_F} \gtrless - \frac{3 n_2(\epsilon_F)}{2 \epsilon_F^2}$$
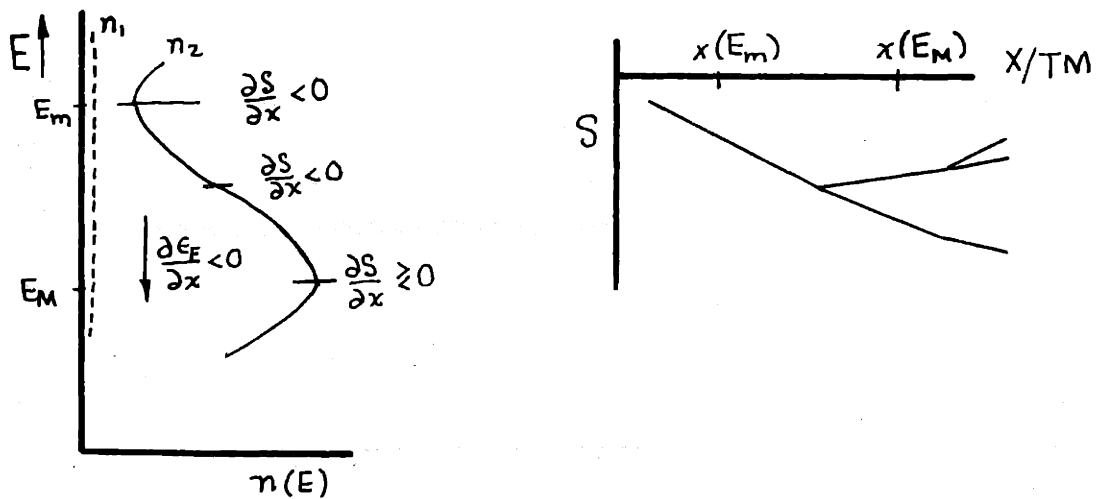
It must be kept in mind that these equations have been developed as if there were two overlapping bands, one of a high density of states, one with a low density of states but that single band conduction is considered to occur with nearly free electron characteristics. The scattering relaxation time in the low density band was assumed inversely proportional to the high density of states in the second band.

The use of these qualitative determinations is probably satisfactory for the transition metal carbides and perhaps even for the nitrides. However, due to the increased anti-bonding character of the d bands with respect to the oxygen p levels as pointed out in Section I any applicability to the oxides will rest on the possible increase in admixture of metal d-s-p bands due to the increase in anti-bonding character of the d bands.

If such formulations are to be applied to NbO_x, two alternatives present themselves. The first is that the Fermi energy must decrease (with $\partial S/\partial x < 0$ following) with increasing O/Nb ratios until 1:1 is reached at which point, the Fermi energy increases again (making $\partial S/\partial x > 0$). The reversal of the sign of the quantity $\partial E_f/\partial x$, however, does not resolve the problem as to whether the Fermi level at $x = 1.0$ is at a minimum or at a maximum in the density of states. Alternatively, if the Fermi level is considered to increase with increasing x through the whole of the single phase field, then the only consistent qualitative picture on this Mott-type model is that the Fermi level is near a maximum in the density of states.
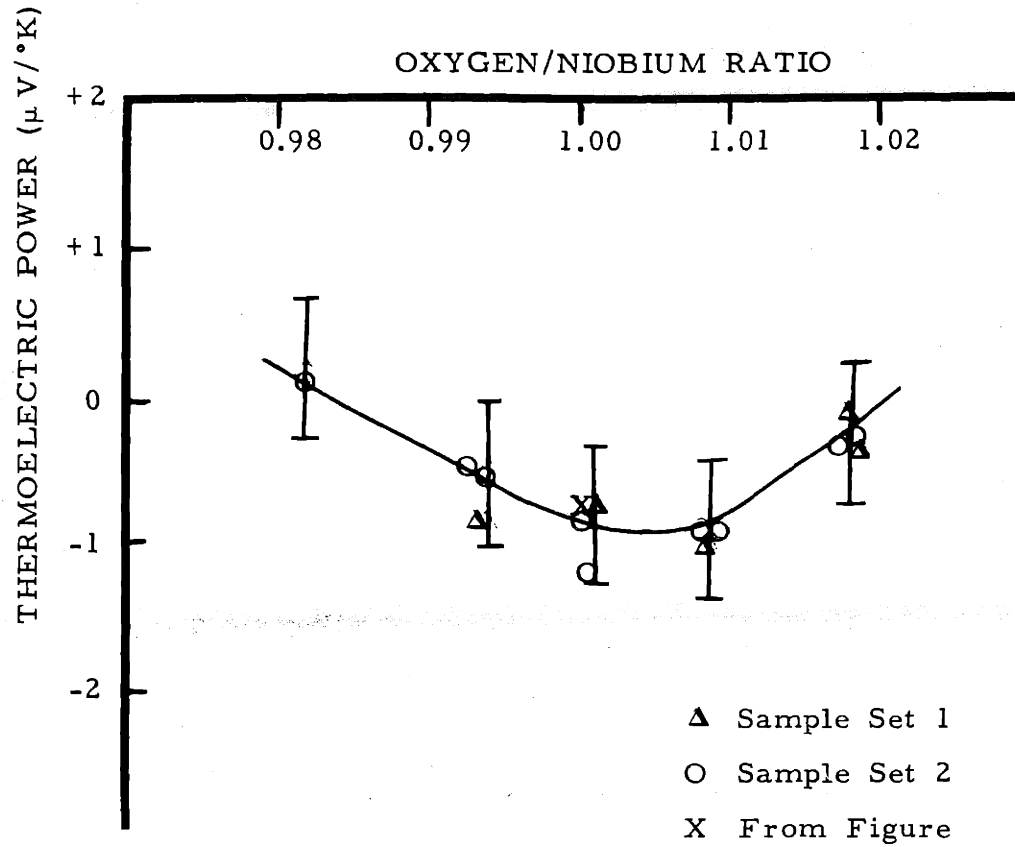
Figure 39 Room Temperature Thermoelectric Power of NbO_x
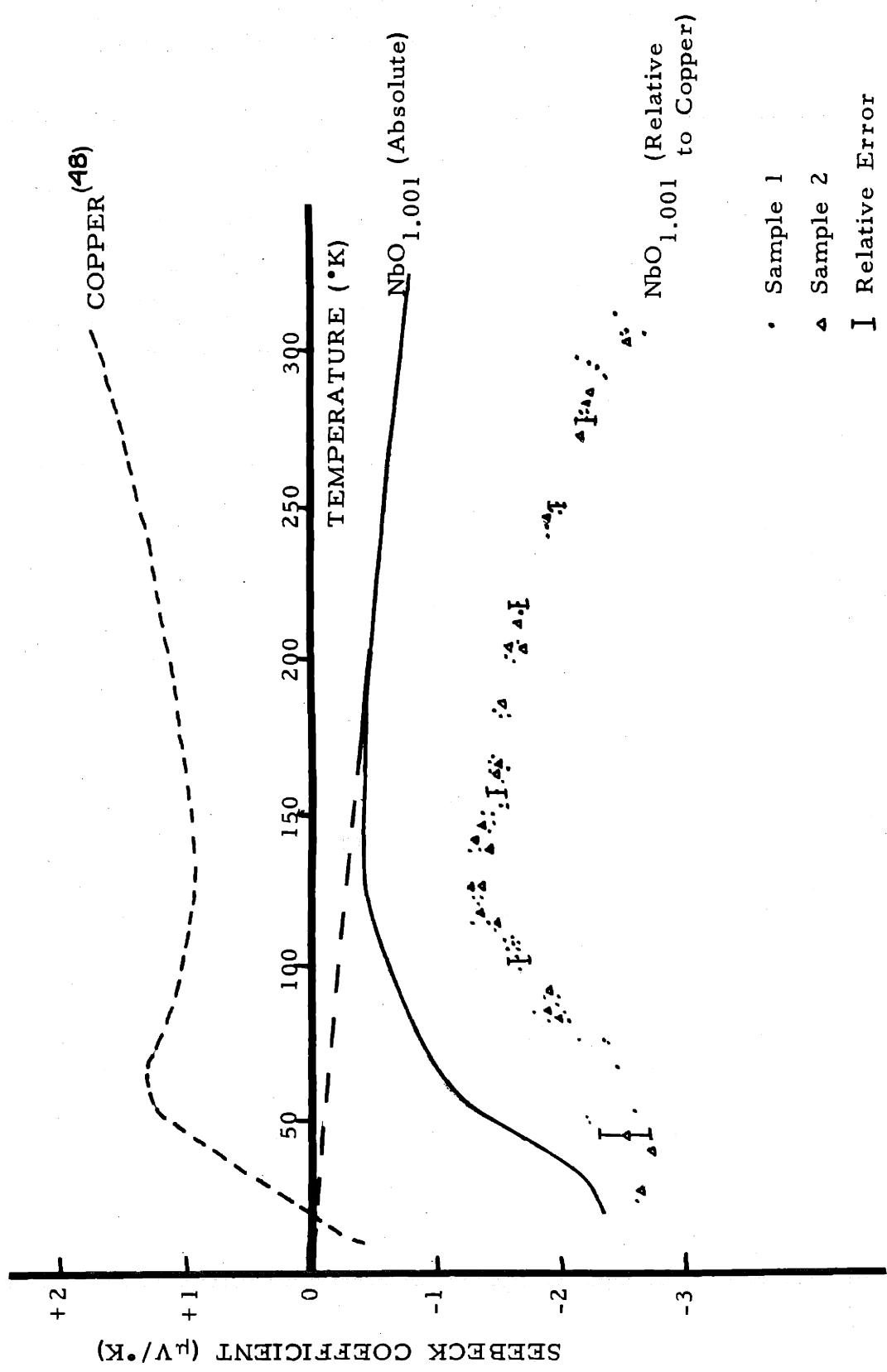
Figure 40 Absolute Thermoelectric Power of $NbO_{1.001}$ as a Function of Temperature
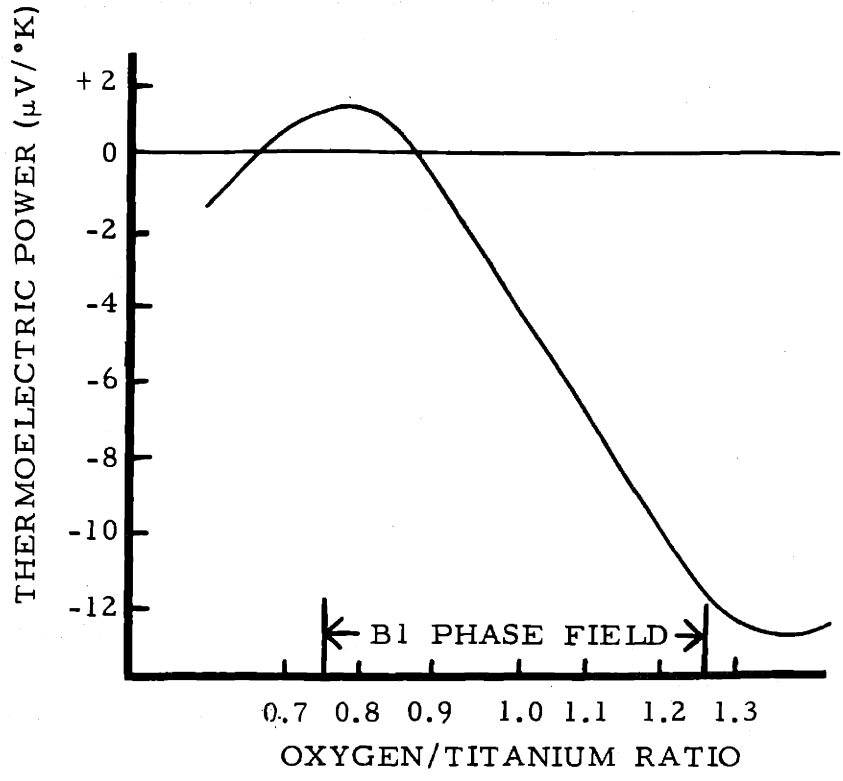
Figure 41a Room Temperature Thermoelectric Power of TiO_x (2)
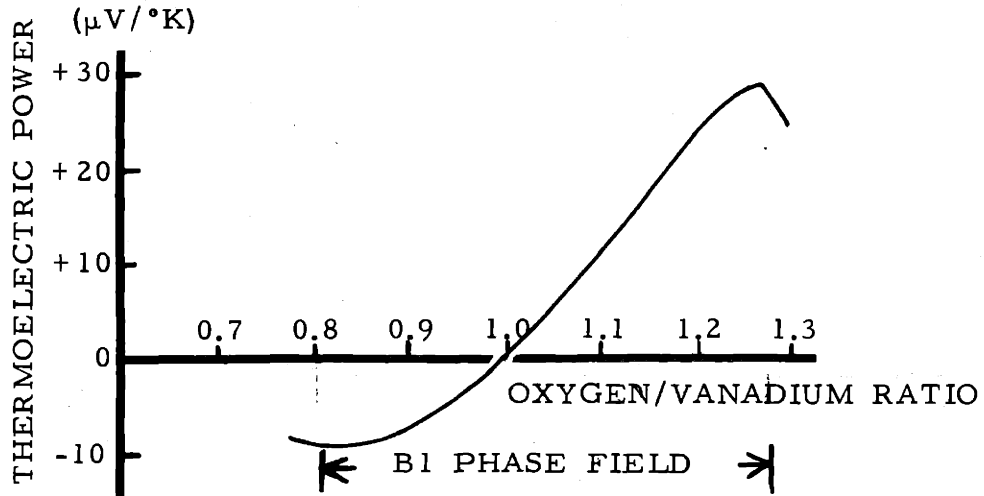
Figure 41b Room Temperature Thermoelectric Power of VO_x (6)

D. Superconductivity

The superconducting transition temperature, T_c, of niobium monoxide as a function of oxygen/niobium molar ratio is shown in Figure 42 . The transition temperature is seen to reach a maximum ($\sim 1.45°K$) at a slightly oxygen rich composition. Inspection of Figure 43 reveals that most of the transitions, as indicated by a relative frequency shift of a tuned oscillator circuit, were not ideally sharp but were spread over a 0.1°K interval. The transition temperature was taken as the temperature where one-half of the total frequency change had occurred.

From the Bardeen, Cooper, and Schrieffer[65](BCS) theory of super-conductivity, the superconductivity transition temperature is related to the product $N(0)V_{ph}$ in the following fashion

$$kT_c \sim \theta_D \exp(-1/N(0)V_{ph}),$$

where k is the Boltzman constant, θ_D is the Debye temperature, $N(0)$ is the density of states at the Fermi level, and V_{ph} is the attractive interaction potential resulting from electron-phonon correlations in the lattice. If the attractive interaction potential, V_{ph}, is assumed constant across the entire single phase field of NbO_x, then one may obtain a qualitative shape of the density of states curve. With this assumption, the Fermi level for the stoichiometric composition must be very near a maximum in the density of states curve.

McMillans' formula[66] for the strong-coupling case in the micro-scopic BCS theory is

$$\frac{1.45\ T_c}{\theta_D} = \exp \frac{-1.04\ (1 + N(0)\ V)}{N(0)\left[V - U_c\ (1 + 0.62\ N(0)\ V)\right]}$$

where

$N(0)$ = density of states at the Fermi level, for $T = 0$,

V = attractive phonon interaction potential,

U_c = coulomb pseudo-potential,

θ_D = Debye temperature.

Geballe et al[57] assumed a value of 0.1 for $N(0)\ U_c$ for all the inter-stitial compounds. The value 0.1 was obtained from McMillan who had used it in describing lead, another case of strong phonon coupling, which prompted Matthias to call the transition metal carbides and nitrides "stiff lead".

We have

$$\ln \frac{1.45\ T_c}{\theta_D} = \frac{-1.04 - 1.04\ NV}{0.938\ NV - 0.1} ,$$

so

$$NV = \frac{-1.04 + 0.1\ \ln \dfrac{1.45\ T_c}{\theta_D}}{1.04 + 0.938\ \ln \dfrac{1.45\ T_c}{\theta_d}} > 0$$

NV must be greater than zero, otherwise superconductivity would not occur.

So, either $\ln 1.45 \, T_c/\theta_D > 10.4$ or $\ln 1.45 \, T_c/\theta_D < -1.11$ where we see that the first case is untenable, requiring $T_c > \theta_D$. Thus $(1.45 \, T_c/\theta_D) < 0.330$ and so $T_c < 0.228 \, \theta_D$. This result is not particularly meaningful since θ_D for NbO is about $600\,°K$ and thus T_c should be less than $137\,°K$. The point of this calculation is that it shows that we are certainly within the limits presented in this formulation for the calculation of density of states.

The T_c for NbO_x is $\sim 1.45\,°K$:

$$\ln \frac{1.45 \, (1.45)}{600} = -5.665$$

$$N(0)\,V = \frac{-1.04 - 0.5665}{+1.04 - 5.32}$$

thus

$$N(0)\,V \leq 0.375$$

Whereas in the strong-coupling case, a $N(0)\,U_c$ value of 0.1 was considered small with respect to $N(0)\,V$, we have here an instance where the value of the coulomb pseudo-potential would be critical.

Geballe et al derived a range of values for V_{phonon} in their work on the niobium carbo-nitrides of 1.1 to 3.2, and this would indicate a range in $N(0) \leq 0.34$ to 0.12 states/eV/molecule for NbO_x, a $N(0)$ range not unlike that in the high T_c carbides and nitrides. APW calculations for TiC, TiN, and TiO[28] yield a density of states at the Fermi level

of 0.2 states/eV/molecule for TiC and about 0.5 states/eV/molecule

for TiN and TiO. The superconducting transition temperature of TiC

is much less than 1°K, of TiN about 5.5°K, and of TiO around 1°K.

Investigators have looked for high superconducting transition

temperature materials using various criteria notably the density of

states at the Fermi level. It would seem that another profitable direction

would be in the determination of the parameters underlying the electron-

phonon interaction potential, V_{phonon}, for it appears that the two

structure classes having the highest transition temperatures, A15, and

B1, do so for opposite reasons.

One notices that the N(0)V value for NbO_x is near that of the so-

called universal value of 0.4 found in most transition metal elements

and their compounds.[67]

Evidently NbC_x, NbN_x, and NbO_x have approximately the same

density of states value, the widely different superconducting transition

temperatures (shown in Figure 44, including values for most transition

metal carbides, nitrides and oxides) are due to V_{phonon}. Although the

density of states for these compounds are about the same, the makeup

of the conduction bands is very different. In NbC_x, we expect a mixture

of TM d, s, p with X p; in the nitride, due to increased ionicity there

will be less TM sp and X p involvement; we would expect no TM d and

X p admixture in the conduction band of NbO_x. From Ern and Switendick's

$APW^{[28]}$ calculations on TiC, TiN, and TiO, the charge analysis in the

APW spheres is seen to portray just such a behavior, although the Ti s

states are seen to remain mixed in the antibonding portions of the un-

filled conduction band in TiO.
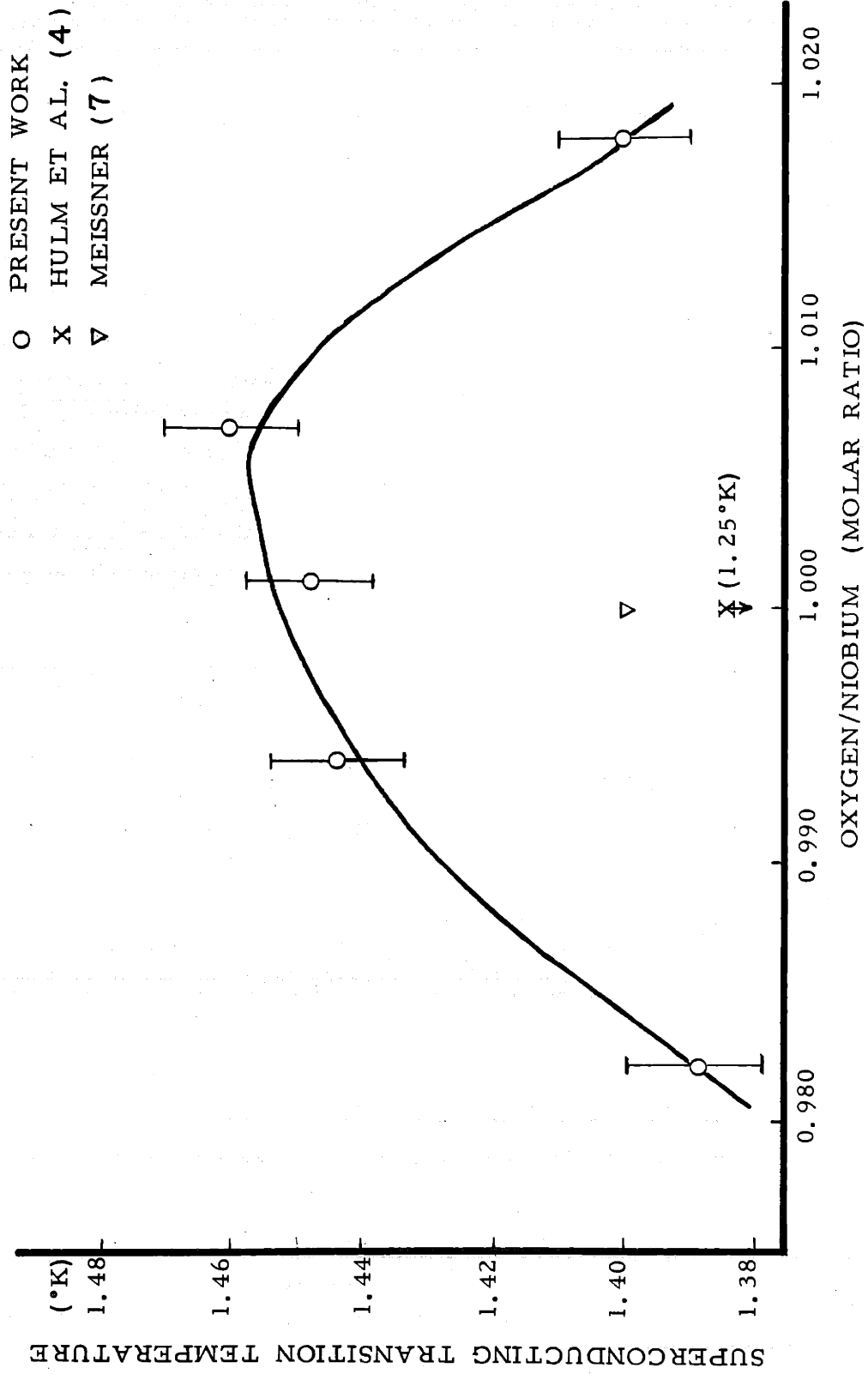
Figure 42   Superconducting transition temperature of NbO_x

SAMPLE	OXYGEN/NIOBIUM RATIO
A	0.982
B	0.994
C	1.001
D	1.008
E	1.018
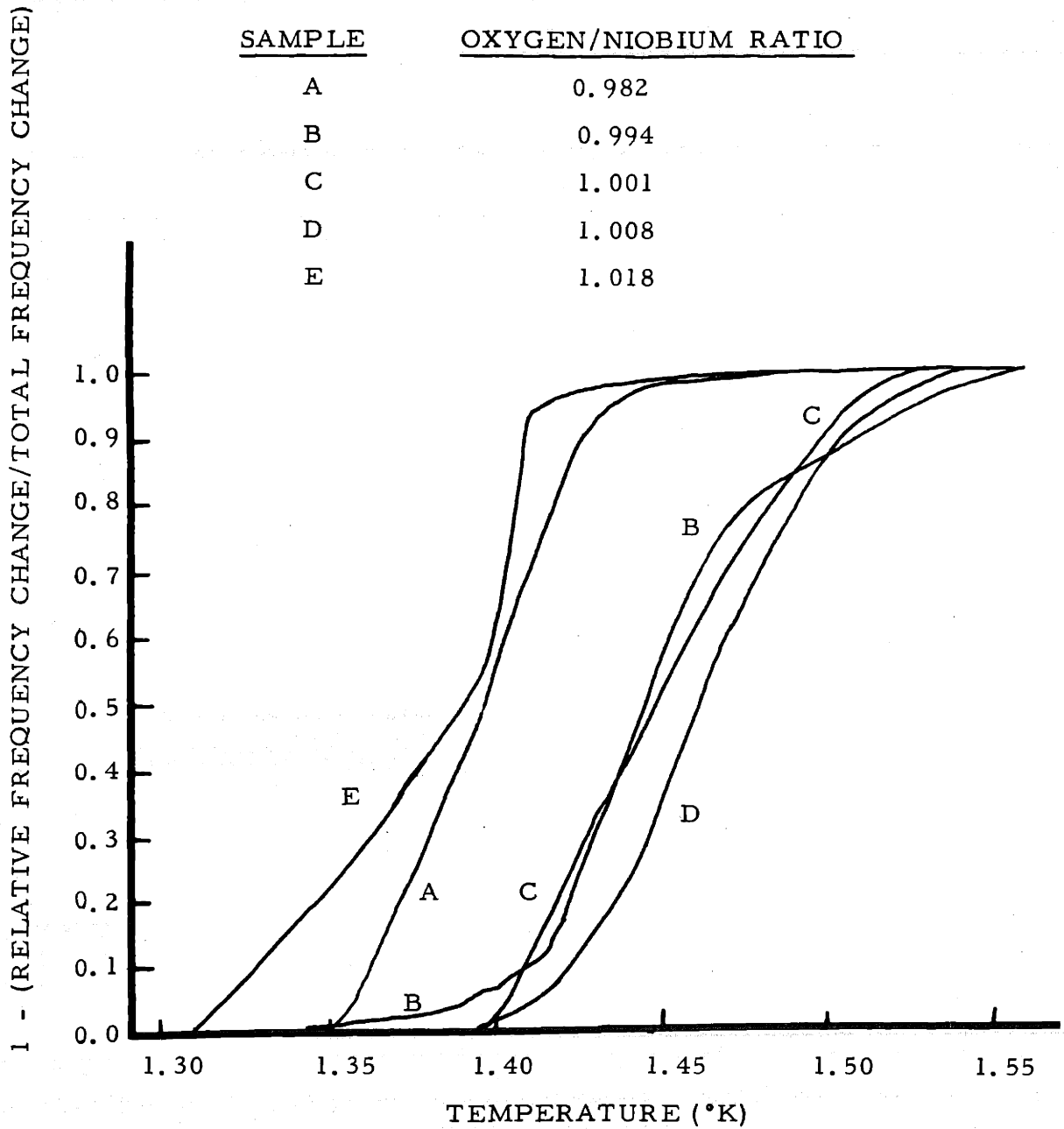
Figure 43. Relative Frequency Shifts for the Determination of the Superconducting Transition Temperature of NbO_x
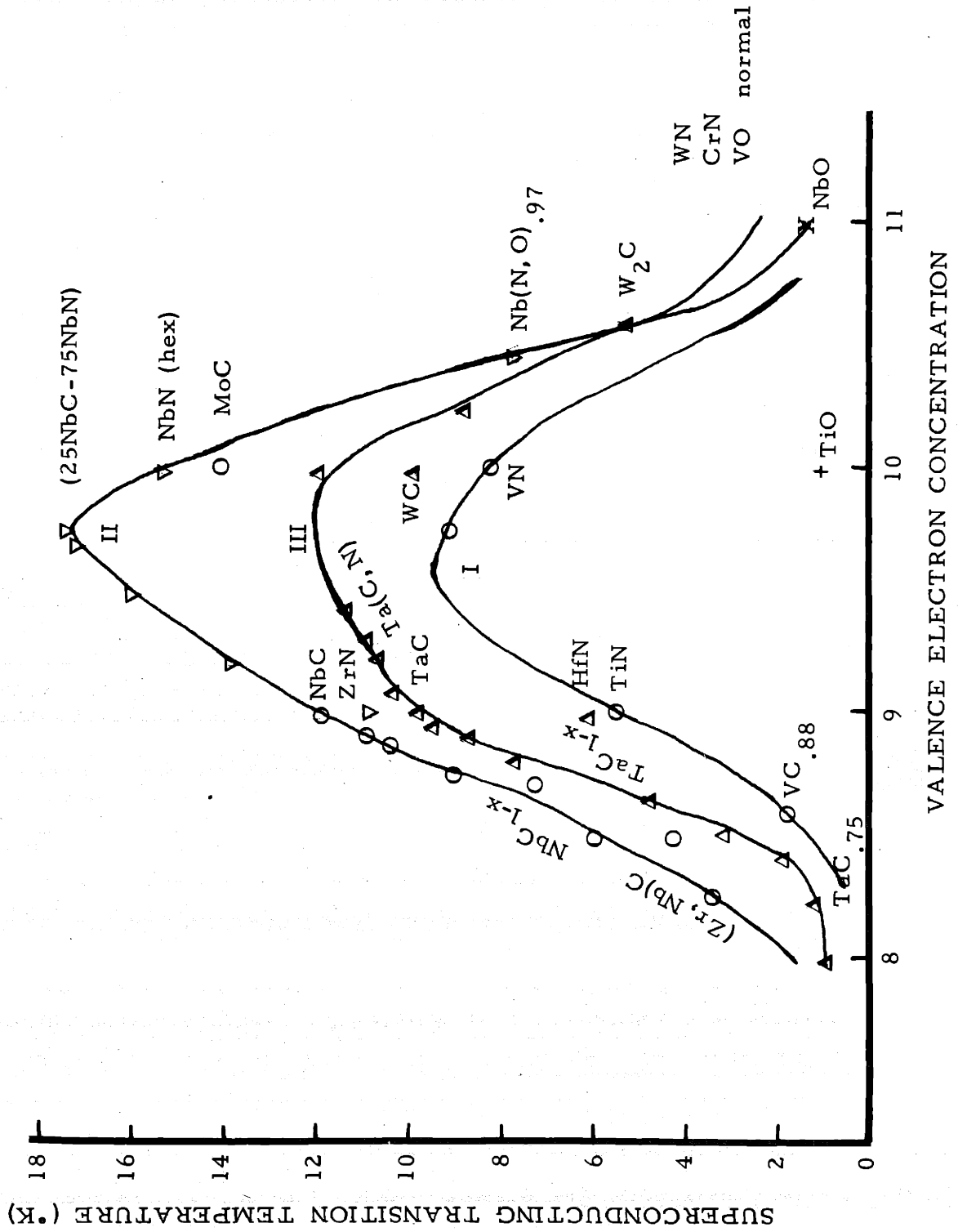
Figure 44 Superconducting Transition Temperature of some Transition
Metal Rocksalt Compounds [83]

E. Optical Reflectivity

As is well known, a Kramers-Kronig (KK) analysis[68] of the reflectivity data, R, can be used to calculate the optical and dielectric constants which are related as follows:

$$\frac{(n - 1 - ik)}{(n + 1 - ik)} = R^{\frac{1}{2}} e^{i\theta} \tag{1}$$

where:

n is the real part of the complex refractive index,

k is the imaginary part of the refractive index,

R is the absolute reflectivity (the square of the reflectance amplitude),

θ is the phase angle for the reversal of the electric field vector on reflection $\left[\theta \equiv \arctan 2k/(1 - n^2 - k^2)\right]$ which may be calculated from:[69]

$$\theta(E_o) = \frac{E_o}{\pi} \int_0^\infty \frac{\ln\left[R(E)/R(E_o)\right] dE}{E^2 - E_o^2} \tag{2}$$

The components of the refractive index are used to calculate the dielectric constant and its real and imaginary parts:

the dielectric constant, $\epsilon = \epsilon_1 - i\epsilon_2 = (n - ik)^2$,

the real part of the dielectric constant, $\epsilon_1 = n^2 - k^2$,

and the imaginary part, $\epsilon_2 = 2nk$.

By calculating Θ and by suitable algebraic manipulations, one can obtain the dielectric constants from the reflectance data.

If R is not known over the entire energy spectrum, it is necessary to extrapolate $R(E)$ to infinite energies, usually by a power law. One can use an extrapolation which will force the optical or dielectric constants to agree with some independent measurement at a particular energy. For example, ellipsometric measurements on metals will yield ϵ_1 and ϵ_2, or n and k directly, which could be used for a forced-fit calculation.

Since the data obtained in these measurements extends only to 12 eV, the integral in equation (2) is decomposed into an integral using the experimental data from 0 to 12 eV and an integral using $R = CE^{-A}$ from 12 eV to infinity, where C and A are adjustable parameters and E is the energy. The latter integral can be transformed into:[70]

$$\frac{E_o}{\pi} \int_{12}^{\infty} \frac{\ln\left[R(E)/R(E_o)\right] dE}{E^2 - E_o^2}$$

$$= \frac{1}{\pi}\left\{\frac{1}{2}\ln\left[R(12)/R(E_o)\right]\ln\left[(12 + E_o)/(12 - E_o)\right]\right. \quad (3)$$

$$\left. - A\sum_{\ell=0}^{\infty} \frac{1}{(2\ell + 1)^2}\left(\frac{E_o}{12}\right)^{2\ell + 1}\right\}$$

If an independent measurement of n or k were available for some E_o, A could be varied in order to give $\Theta(E_o)$ and, therefore, n, k, which would agree with the independently measured values.

The specular reflectivity of $NbO_{1.0}$ was determined over two overlapping energy regions: 1) 0.05 to 3.5 eV and 2) 2.7 to 12 eV. The second energy region was normalized to the first since over the first region, absolute reflectance measurements were obtained. The experimental setups were described in section III B . In Figure 45 is shown the absolute reflectivity versus incident photon energy for niobium monoxide. Also included in the figure is Denker's results on $TiO_{1.0}$[2] (these data were not absolute values).

In Figures 46 and 47 are plotted ϵ_1, and ϵ_2 which were obtained from the KK analysis of the reflectivity data (Figure 45). The computer program that was used was developed by Scouler[71] and was

a modification of one described by Phillips[72]. From ϵ_1 and ϵ_2, the energy loss function $\epsilon_2/(\epsilon_1^2 + \epsilon_2^2)$ is calculated and plotted in Figure 48.   The peaks in this curve are due to resonance effects as can be seen by comparing the curve with that of ϵ_2. In each figure, several curves are shown, each for a different value of the reflectivity decay exponent, A.

Another quantity of interest which can be obtained in this analysis is n_{eff}, the effective number of electrons per niobium atom contributing to the optical properties. This is calculated from the oscillator strength sum rule of the form:[73]

$$n_{eff}(E') = (m_o/2\pi^2\hbar^2 N e^2) \int_o^{E'} E \, \epsilon_2(E) \, dE \qquad (4)$$

where m_o is the free electron mass and N is the number of niobium atoms per cubic centimeter. The n_{eff} scale in Figure 49   has been multiplied by three to account for the three NbO molecules per unit cell. In this fashion, one can make a direct comparison of the number of optically active electrons in the unit cell with the number of states thought to be in each of the energy bands. Since the threshold for interband transitions is apparently so low, the first plateau observed in n_{eff} must be due to an admixture of a small free electron-like behavior of electrons near the Fermi level and possible collective

behavior of the upper filled valence band electrons, as well as to the first set of interband transitions. The curve for n_{eff} exhibits several near plateaus indicative of the emptying of energy bands. If all of the valence electrons of the three niobium atoms (15) and the three oxygen atoms (18) had been exhausted, n_{eff} should have saturated at 33, providing that still deeper lying levels were not being excited. The data does not extend far enough to show this saturation. Since only a fraction of the total valence electrons have been involved up to 12 eV, it is not surprising that the reflectivity is still rather high at that point.

The present work on NbO indicates that the onset of interband transitions occurs at very low energy, between 0.1 and 0.2 eV, or at least by 0.7 eV. At the lowest energy the reflectivity attains a value of about 99 percent. Although the reflectivity decreases fairly smoothly up to 1.5 eV, no true plasma edge or resonance is observed. Additional reflectivity shoulders and peaks, due to other electronic transitions, occur around 2.1, 3.5, 4.8, 6.2, 7.7, and 9 eV. Beyond 9 eV, the reflectivity slowly decreases. The reflectivity at 11.5 eV is still relatively high indicating that significant absorption processes are still occurring at higher energies.

While one would normally make assignments of structure in the reflectivity spectra with a known band calculation, we must depart from this procedure in this instance and try to piece together a plausible band structure for NbO from the data. To correlate peaks in the imaginary part of the dielectric constant, ϵ_2, with various energy bands

and their separations without extensive calculations, two assumptions
are necessary:

1) the resonances giving rise to peaks in ϵ_2 are not collective
(plasma) or hybrid resonances but only bound particle excitation
effects (interband transitions), and

2) these peaks can be attached to large joint density of states in
the energy band scheme.

The assignment then of a given transition is to be a single particle
excitation between two peaks in a qualitative density of states curve.
No symmetry or parity selection rules are to be considered.

The transitions that must be considered are obtained from Figure
47   and include:

1)   0.1 eV - possibly not real,

2)   0.7 eV,

3)   1.1 eV,

4)   1.8 eV,

5)   3.0 ± 0.1 eV,

6)   4.7 eV,

7)   5.9 eV,

8)   8.9 eV.

One will note that there are no transitions in the visible range (1.8 to
3.0 eV) of the spectrum for NbO and hence the bright silvery appearance
of the crystals. This is in constrast to the appearance of transitions in

the red and violet portions of the spectrum for TiO accounting for its dark gold coloring[2].

Discussion of a proposed one-electron energy band scheme is deferred to section III-G in which the ordered defect structure is considered. At that point, other property measurements will have been presented and discussed so that an understanding of the nature of NbO may be obtained.
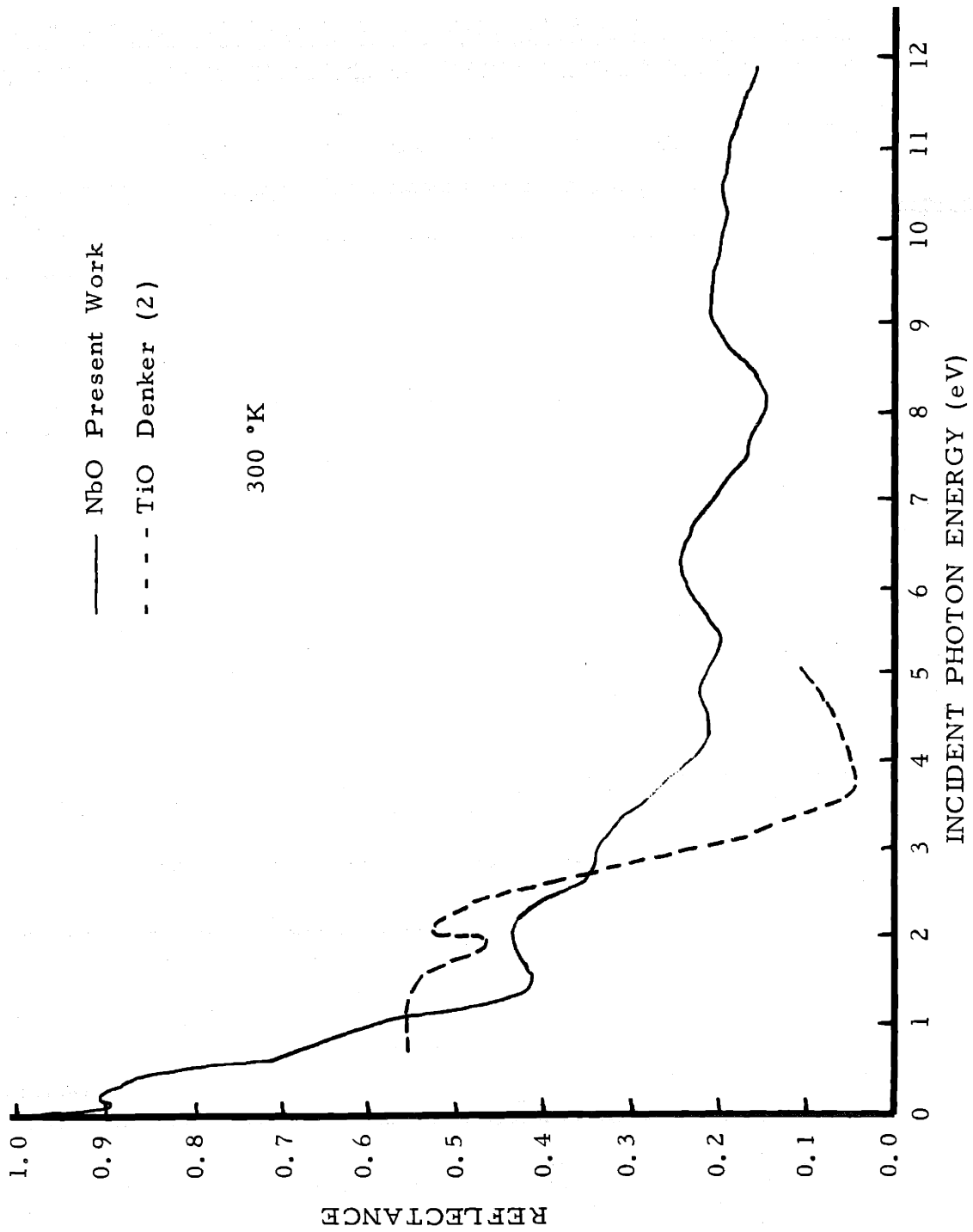
Figure 45   Room temperature reflectance of niobium monoxide,
included for comparison is the reflectance of TiO.
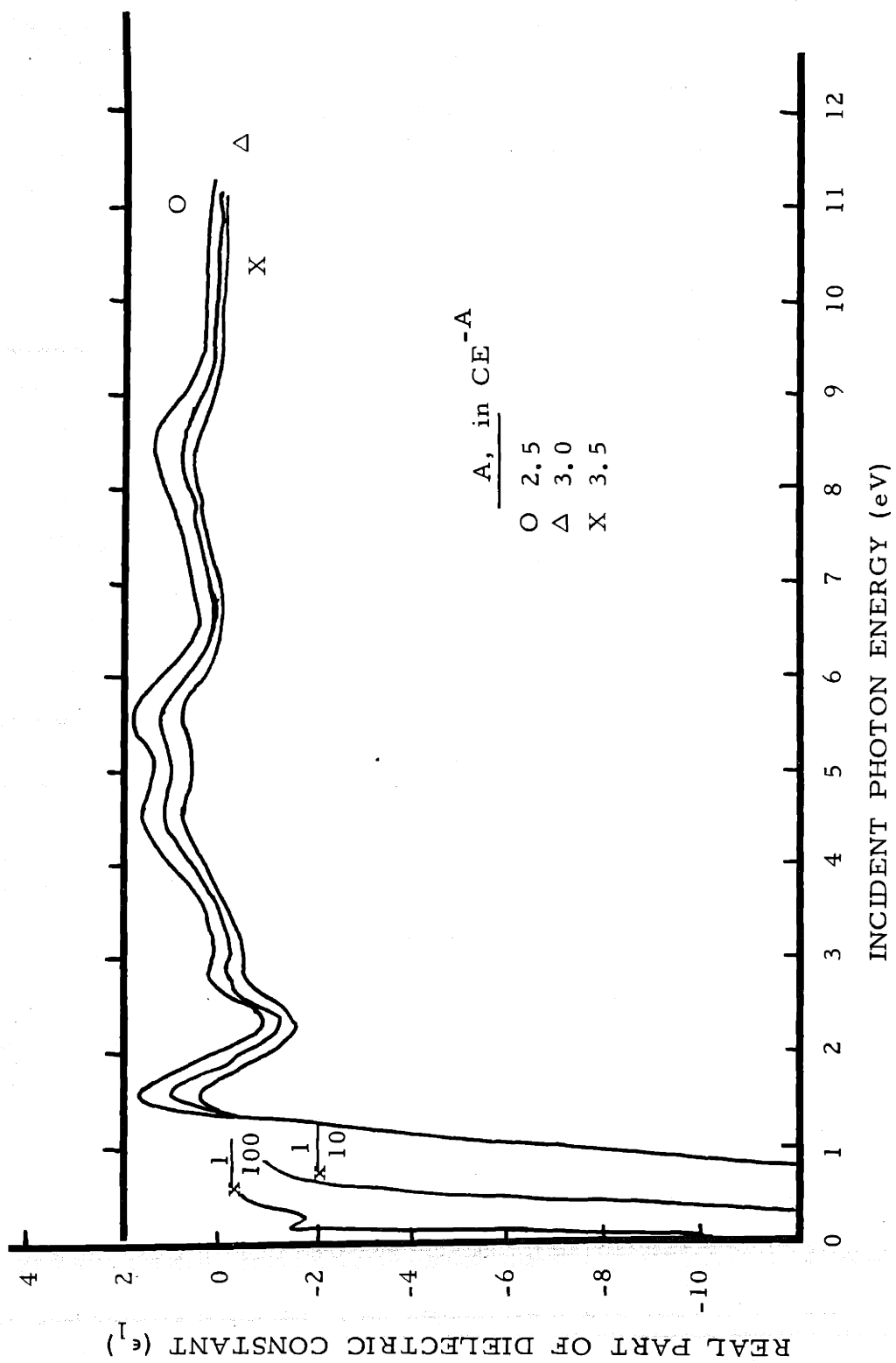
Figure 46   Real part of the complex dielectric constant of niobium monoxide
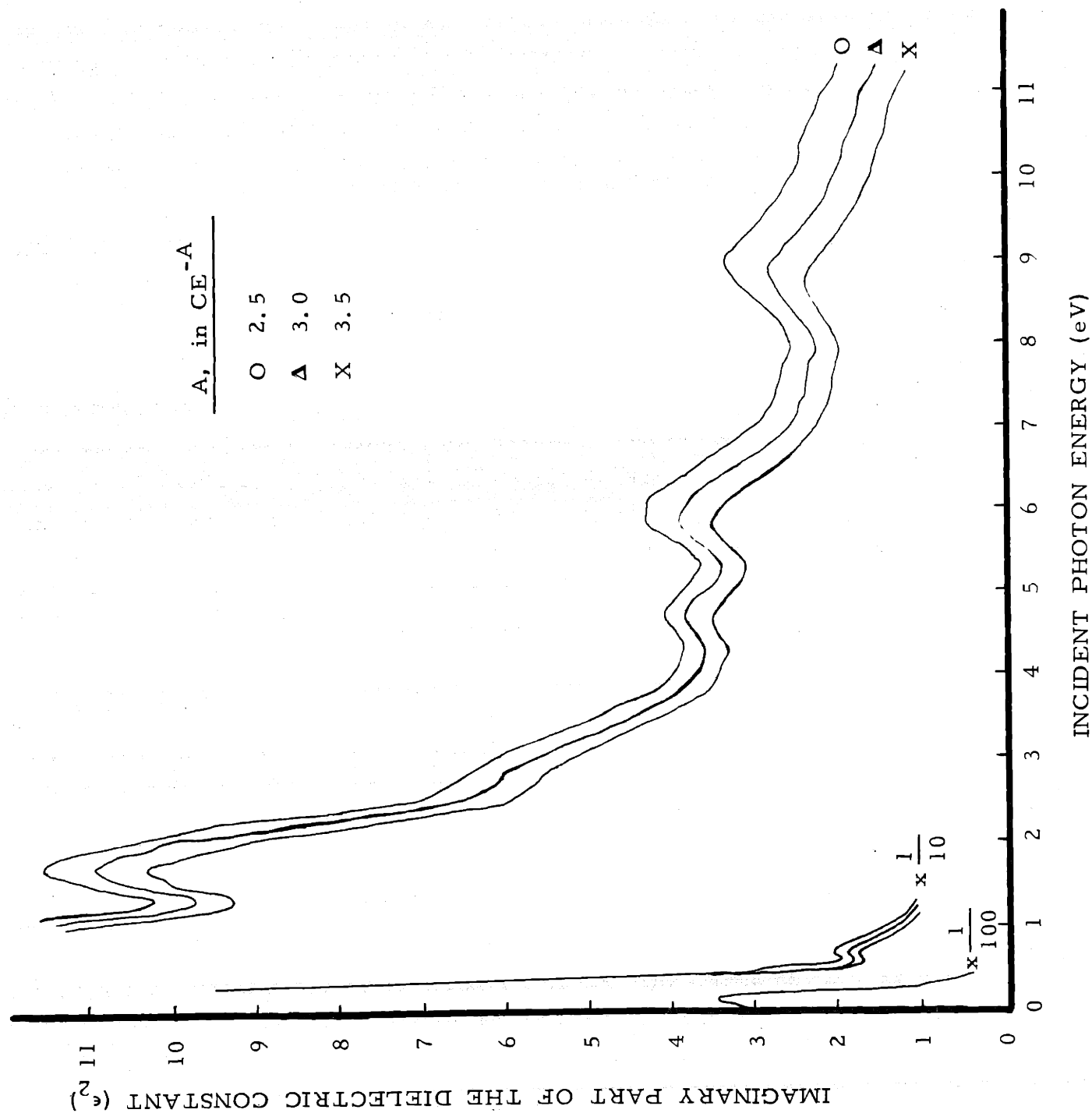
Figure   47   Imaginary part of the complex dielectric constant of
niobium monoxide
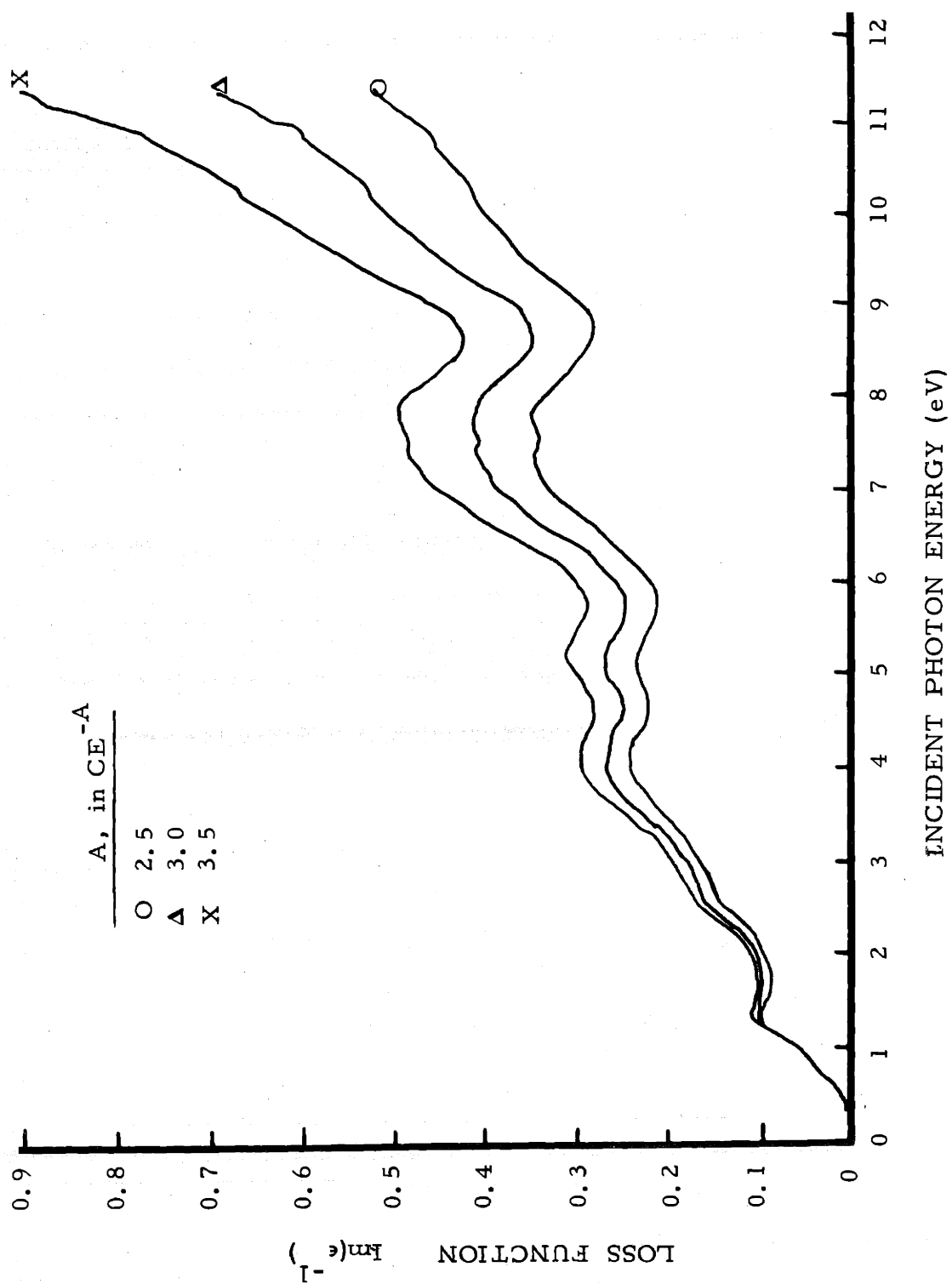
Figure 48   Optical Loss Function of NbO at Room Temperature
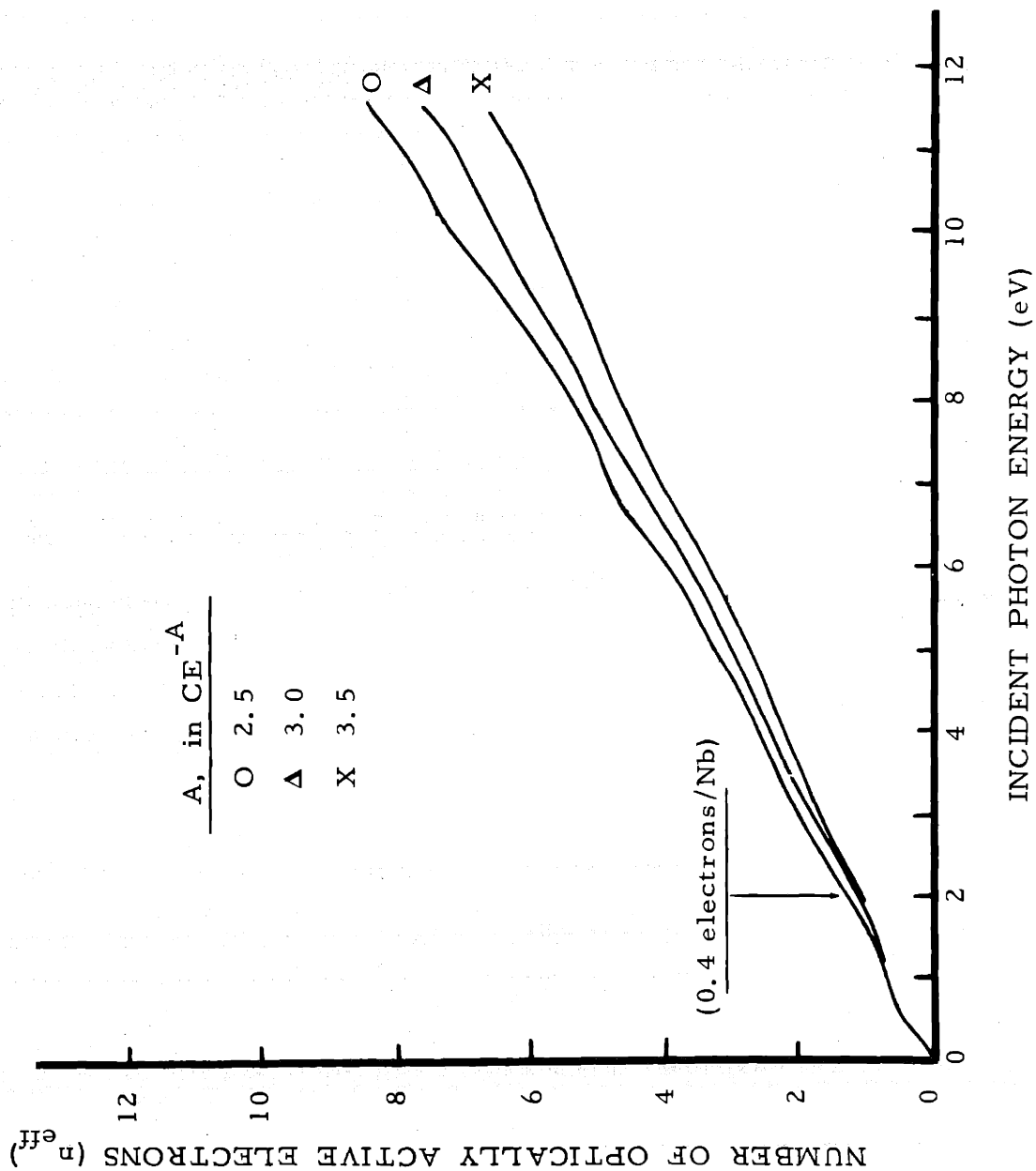
Figure 49   The number of optically active electrons in niobium
monoxide determined from reflectivity

F. Parameterized Band Structure Calculation

A Slater-Koster[23] L. C. A. O. approach was taken for a qualitative determination of the band structure in the vicinity of the conduction bands. Only the d-t_{2g} orbitals of the niobium atoms were considered. Three inequivalent niobium atoms were assumed to be in the unit cell.

The main purpose of the Slater-Koster technique is as an interpolation scheme rather than an analytical calculation. It affords a good description of the energy bands at points other than simple symmetry points and is to be used in conjunction with more accurate calculations (such as by the Augmented Plane Waves technique) made at specific symmetry points. In Appendix A is given the development of the Slater-Koster scheme for TiO where Augmented Plane Wave calculations are available.

The Slater-Koster procedure treats the transfer integrals

$$H_{ij} = \int \psi_i (\vec{r}) \, H \, \psi_j (\vec{r} - pa\vec{i} - qa\vec{j} - ra\vec{k}) \, d\tau$$

(where $\vec{r}$ is the position vector of atom i, and p, q, r are the coodinates of atom j with atom i considered as the origin, a is the cell side) as adjustable parameters, the integral vanishing whenever the orbital overlap integral vanishes, $\int \psi_i \, \psi_j \, d\tau = 0$.

The case of three niobium atoms in the simple cubic cell of NbO, each with three t_{2g} type functions, requires the solving of a 9 x 9 secular determinant, the elements of which are the transfer integrals between various niobium atoms as the origin and its near neighbor niobium atoms. An important aid in the reduction of the 9 x 9 determinant is the utilization of required degeneracies from group theory at particular points in the simple cubic Brillouin zone. Thus at Γ (000), the center of the zone, one knows that the 9 x 9 matrix must reduce to three identical 3 x 3 submatrices from which three three-fold degenerate energy eigenvalues can be obtained (the $\Gamma_{25'}$ points). For the t_{2g} bands of NbO including only nearest Nb-Nb interactions, five adjustable parameters result, A_1, A_2, α, β, and γ. These are defined accordingly:

$$A_1 = \langle xy_1/xy_1 (000) \rangle = \int \phi_{xy_1} H \phi_{xy_1} d\tau \ ,$$

$$A_2 = \langle xz_1/xz_1 (000) \rangle = \int \phi_{xz_1} H \phi_{xz_1} d\tau \ ,$$

$$\alpha = 4 \langle xy_1/xy_3 (110) \rangle = \int \phi_{xy_1} H \phi_{xy_3} d\tau \ ,$$

$$\beta = 4 \langle xy_1/xy_2 (011) \rangle = \int \phi_{xy_1} H \phi_{xy_2} d\tau \ ,$$

$$-\gamma = 4 \langle xz_1/yz_3 (110) \rangle = \int \phi_{xz_1} H \phi_{yz_3} d\tau \ .$$

A_1 and A_2 are self-interaction integrals which will have different values because of their orientation with respect to the oxygen vacancy at $\left(\frac{1}{2} \frac{1}{2} \frac{1}{2} \right)$. For A_1, the vacancy is in the plane of the orbital function lobes, and out of the orbital lobes plane in the case of A_2.

The 9 x 9 matrix for a general point in the Brillouin zone for NbO is

	xy_1	xz_1	yz_1	xy_2	xz_2	yz_2	xy_3	yz_3	xz_3
xy_1	A_1			$\beta c\eta c\zeta$	$\gamma s\eta s\zeta$		$\alpha c\xi c\eta$		
xz_1		A_2		$\gamma s\eta s\zeta$	$\beta c\eta c\zeta$			$\gamma s\xi s\eta$	$\beta c\xi c\eta$
yz_1			A_1			$\alpha c\eta c\zeta$		$\beta c\xi c\eta$	$\gamma s\xi s\eta$
xy_2	$\beta c\eta c\zeta$	$\gamma s\eta s\zeta$		A_2			$\beta c\xi c\zeta$	$\gamma s\xi s\zeta$	
xz_2	$\gamma s\eta s\zeta$	$\beta c\eta c\zeta$			A_1				$\alpha c\xi c\zeta$
yz_2		$\alpha c\eta c\zeta$				A_1	$\gamma s\xi s\zeta$	$\beta c\xi c\zeta$	
xy_3	$\alpha c\xi c\eta$			$\beta c\xi c\zeta$		$\gamma s\xi s\zeta$	A_1		
yz_3		$\gamma s\xi s\eta$	$\beta c\xi c\eta$	$\gamma s\xi s\zeta$		$\beta c\xi c\zeta$		A_2	
xz_3		$\beta c\xi c\eta$	$\gamma s\xi s\eta$		$\alpha c\xi c\zeta$				A_1

where we have used the abbreviations for the arguments $\xi = ak_x$, $\eta = ak_y$, $\zeta = ak_z$, and c = cosine, s = sine (see Figure 3 for the atom number designation). The elements in the matrix may be determined and the resulting secular equation may be evaluated at any point, for instance at Δ ($\xi = 0, \eta = \frac{\pi}{4}, \zeta = 0$), at Γ (0, 0, 0) or at R ($\frac{\pi}{2}, \frac{\pi}{2}, \frac{\pi}{2}$). The ξ, η, ζ, values at the major symmetry points in the simple cubic Brillouin zone are

	ξ, η, ζ					ξ, η, ζ		
Γ	0	0	0	Σ	$\frac{\pi}{4}$	$\frac{\pi}{4}$	0
Δ	0	$\frac{\pi}{4}$	0	Λ	$\frac{\pi}{4}$	$\frac{\pi}{4}$	$\frac{\pi}{4}$
X	0	$\frac{\pi}{2}$	0	R	$\frac{\pi}{2}$	$\frac{\pi}{2}$	$\frac{\pi}{2}$
Z	$\frac{\pi}{4}$	$\frac{\pi}{2}$	0	S	$\frac{\pi}{4}$	$\frac{\pi}{2}$	$\frac{\pi}{4}$
M	$\frac{\pi}{2}$	$\frac{\pi}{2}$	0	T	$\frac{\pi}{2}$	$\frac{\pi}{2}$	$\frac{\pi}{4}$

At the point Γ (000) we have the three-fold degenerate secular equation

$$\begin{vmatrix} A_1 - \epsilon & \alpha & \beta \\ \alpha & A_1 - \epsilon & \beta \\ \beta & \beta & A_2 - \epsilon \end{vmatrix} = 0$$

with the resulting solutions

$$\epsilon = A_1 - \alpha$$

$$\epsilon = \frac{A_1 + A_2 + \alpha}{2} \pm \frac{1}{2} \sqrt{(A_1 - A_2 + \alpha)^2 + 8\beta^2}$$

In Figure 50 is shown the result of such qualitative calculations for the direction $\overline{\Gamma \Delta X}$. The scale values assumed for A_1, A_2, α, β are shown on the figure. The relative values of α, β, and γ were assumed on the basis of their overlap and the type of bonding they represent, i. e., α is a purely directed overlapping bond (σ type) whereas β or γ represent π bonds and should have small overlap integral values. The effect of changing α, β and or γ (in the direction $\overline{\Gamma \Delta X}$) is to change the amount of splitting between the calculated energies, i. e., increasing α while

decreasing β will increase the overlap in the lower portions of the bands while pushing the upper third of the bands to higher energy. The increase of the ratio A_2/A_1 has the effect of widening the total t_{2g} band.

The purpose of these calculations is not the determination of the actual d-t_{2g} bands in NbO but rather for a qualitative picture of the splitting in the t_{2g} bands by virtue of the unusual structure of niobium monoxide. The d-t_{2g} bands are seen to split into two portions, one of which contains two-thirds of the energy states while the other portion has the remaining third. This proportional splitting is in good agreement with that which one would expect from a spin-orbit coupling calculation or from a one-electron energy band picture determined solely by the crystal structure (see other examples of such behavior in papers by Goodenough[1]). In the next section, a one-electron energy band scheme will be developed for the NbO structure.
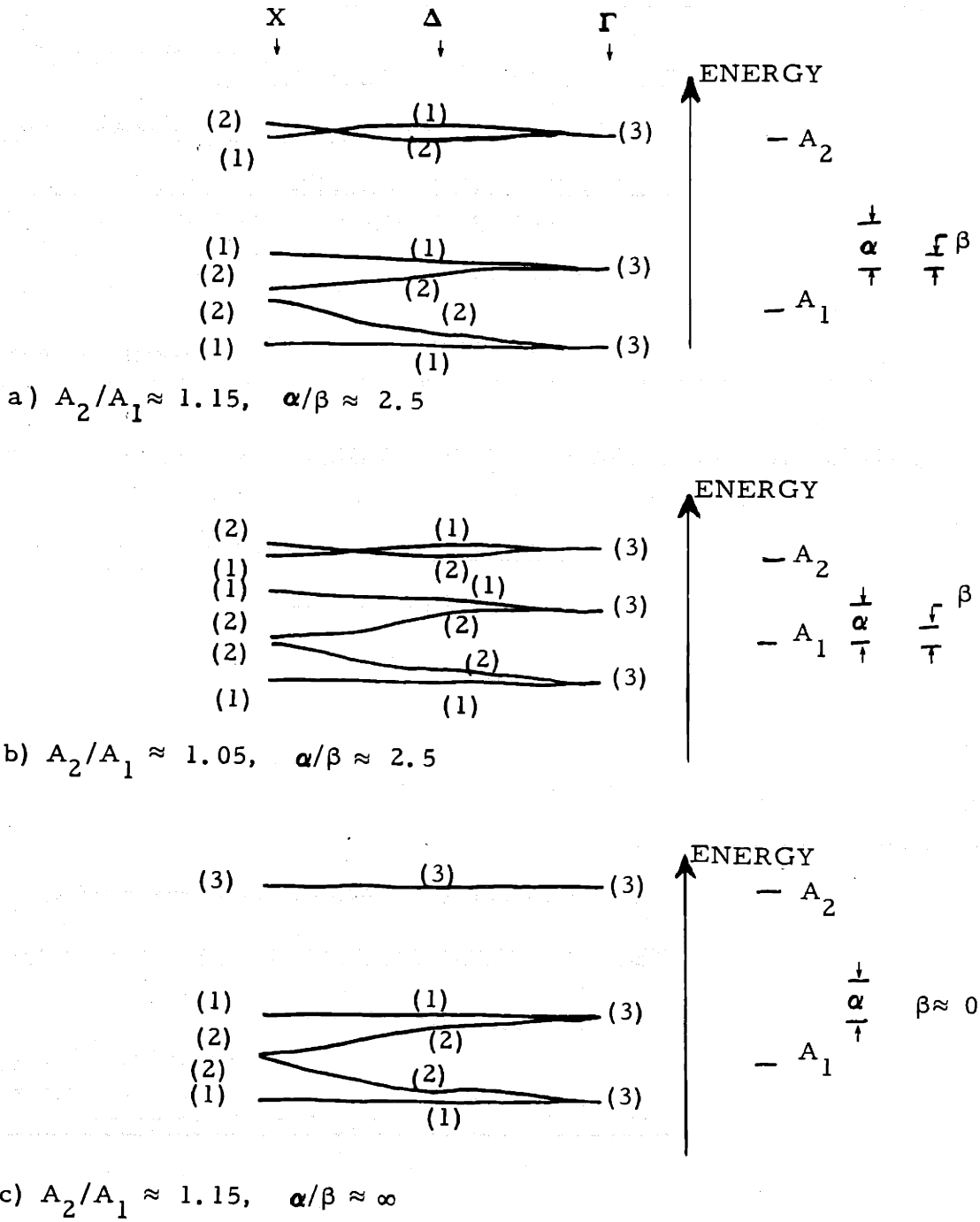
Figure 50   Slater-Koster Parameterized Scheme in the $\langle 100 \rangle$ Direction for NbO

G. Structural Features Of Niobium Monoxide

 1. Lattice Parameter

The lattice parameter of NbO_x was determined as described in Section IIIB. The results are shown in Figure 51 and indicate that the unit cell side increases with increasing oxygen/niobium ratio. The lattice parameter for presumed $NbO_{1.00}$ reported by Brauer [29], Elliott [33], and Bowman et al [31] are low compared to that determined presently. Their values of the lattice parameter correspond to that found on the low oxygen side of the homogeneity range and are probably due to the manner of preparation of the samples. The initial samples in the present work were prepared in the same way as the above previous work and the lattice parameters were found to group around 4.2104 Å no matter the initial nominal composition. Combustion analysis indicated that the compositions were all below 0.90 O/Nb molar ratio. X-ray analysis indicated a minute quantity of second phase, niobium.   The preparation technique used in all these instances was that of pressing mixtures of niobium and niobium pentoxide powders in the appropriate amounts followed by vacuum heat treatment, typically 1-2 hours at 1500 - 1600°C. This technique generally led to an incomplete reaction. Oxygen is also apparently lost from the pentoxide during the vacuum heat treatments.
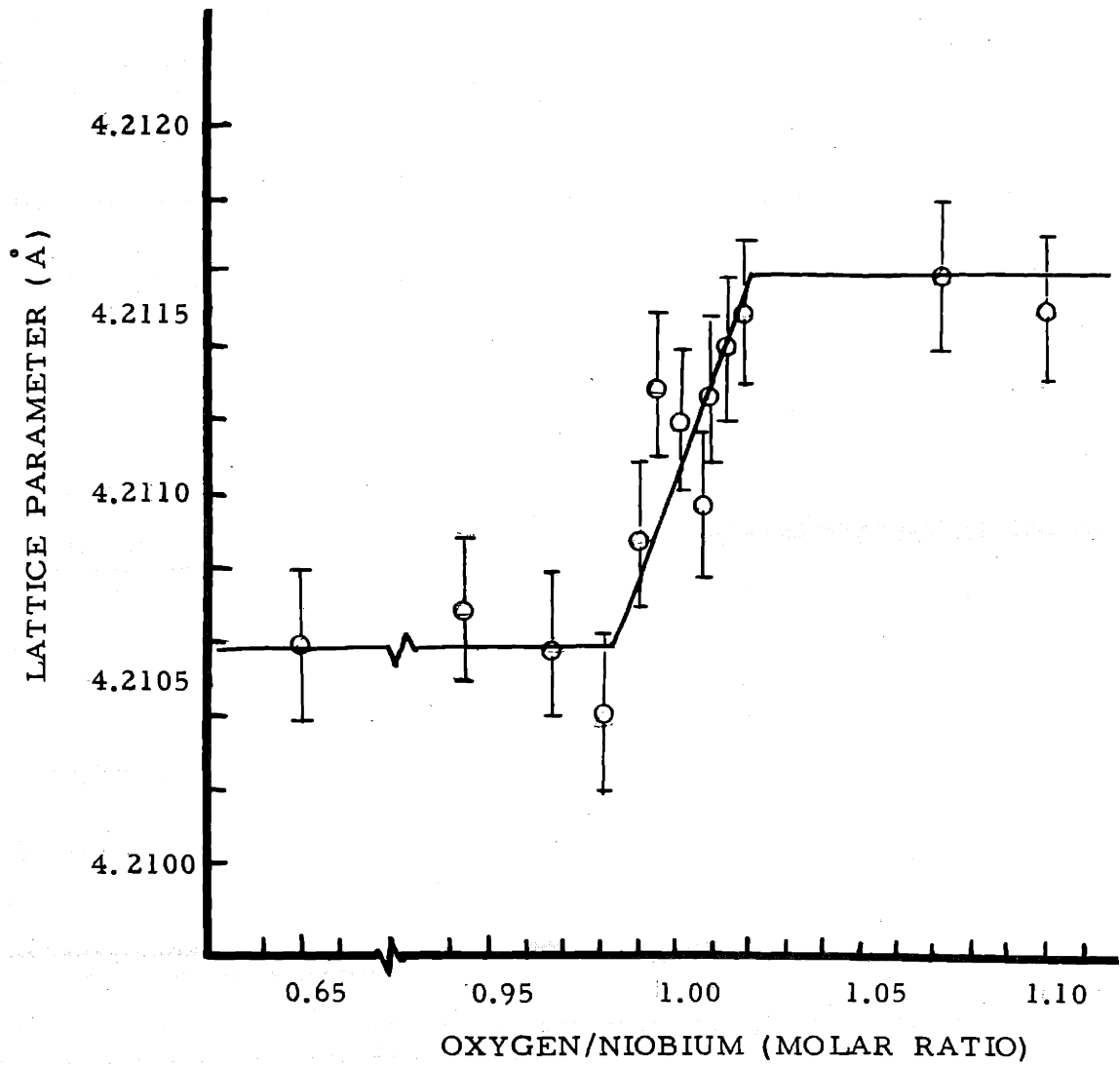
Figure 51 Unit Cell Lattice Parameter of NbO_x

2. Density

Pycnometric density measurements for either composition extreme have been measured by Banus [58] on samples prepared during this work and they showed very little change in value from that measured for the stoichiometric composition, i.e., 7.24 grams/cm^3. The densities were determined to only slightly better than one percent and, because of the narrow homogeneity range, were not of much aid in the determination of the vacancy filling mechanism (see Table 3).

The measured density of 7.24 grams/cm^3 for the 1:1 molar ratio corresponds to three NbO molecules per unit cell, in excellent agreement with the assumed structure (Figure 3),

$$\rho = \frac{n\,W}{a_o^3\,N_o}$$

$$n = \frac{7.24 \left(4.2111 \times 10^{-8}\right)^3 \left(6.023 \times 10^{23}\right)}{(92.91 + 16.00)}$$

$$n = 2.99 \text{ molecules per unit cell}$$

3. Vacancy Model

The lattice filling proposed in this work differs from that usually
assumed in the TiO_x system. In TiO_x, the total content of lattice site
vacancies remains approximately constant at some fifteen percent from
0.75 to 1.25 oxygen to titanium molar ratio. As one proceeds to higher
oxygen content, the percentage of titanium vacant sites increases from
7.7 to 22.7 percent, while that of oxygen vacant sites decreases from
25.8 to 3.4 percent [82]. The titanium vacancy content appears to follow
a linear law while the oxygen vacancy content versus composition is
parabolic or higher. While this seems odd, it is relatively easy to see:
assume $v_{Ti} = a + bx$ where $x = n_{Ti}/n_O$ (per unit cell); the vacancy
fractions are defined as $v_{Ti} = 1 - (n_{Ti}/4)$ and $v_O = 1 - (n_O/4)$, then
$x = (1 - v_O)/(1 - v_{Ti})$; we have then that $v_O = 1 - (1 - v_{Ti})x$ and from
the linear assumption for v_{Ti}, we get $v_O = 1 - (1 - a)x + bx^2$.
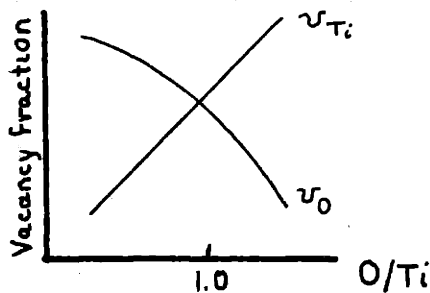
A linear variation for one type of vacancy gives rise to a quadratic
behavior for the second type.

The vacancy concentration in VO_x has been determined [74], and it was found that at stoichiometry ($x = 1$), there are about sixteen percent of the atoms missing from either sublattice. The vacancy concentration for each species decreases with increasing atom content as in the case of TiO_x and never reaches zero.

In NbO_x, it is proposed that the vacancy content of a given type of site never exceeds 25 percent, the value that both sublattices have in the ordered defect rocksalt structure at the 1:1 molar ratio. As the oxygen/niobium molar ratio is decreased from 1.00, the excess niobium atoms go into vacant niobium sites (randomly) while maintaining the ordered 25 percent oxygen vacancies. At the high oxygen composition limit, the excess oxygen atoms randomly fill the $\left(\frac{1}{2} \; \frac{1}{2} \; \frac{1}{2}\right)$ vacant oxygen sites. The niobium sublattice remains ordered and intact. Table 3 contains calculated vacancy fractions, a simple total valence electron concentration, and calculated and observed densities. The valence electron concentration was calculated as V.E.C. $= 4(5f_{Nb} + 6f_O)/3$.

The representation then of NbO_x is not that of an ordered defect structure but rather that of a structure class of its own (defined as B1') with compositional variation due to the addition of the excess atoms randomly onto the proper type site. Other known structurally similar compounds such as W_3N_4 may be merely the extension of the NbO structure.

Although the total number of valence electrons per unit cell is calculated to go through a minimum at the stoichiometric composition, the number of active electrons (n_{eff}) will depend on the relative positions of the localized levels introduced with the excess atoms.

Table 3

Site Filling Model For NbO

$x = \dfrac{n_O}{n_{Nb}}$	$v_{Nb} = (1 - f_{Nb})$	$v_O = (1 - f_O)$	V. E. C.	$a_o \times 10^8$	ρ_{calc}	ρ_{obs} [58]
0.980	0.234	0.250	11.10	4.2105	7.39	
0.985	0.238	0.250	11.08			
0.990	0.242	0.250	11.05	4.2108	7.33	
0.995	0.246	0.250	11.02			7.29
1.000	0.250	0.250	11.00	4.2111	7.24	7.24
1.005	0.250	0.247	11.02			7.24
1.010	0.250	0.243	11.05	4.2113	7.26	
1.015	0.250	0.239	11.08			
1.020	0.250	0.235	11.12	4.2116	7.27	7.29

4. Congruent Melting Point

The congruent melting composition in the NbO_x single phase region was found to be at a 1.006 ± 0.002 oxygen to niobium molar ratio. The congruent point was determined by comparison of the compositions across the crystal-melt interface. A charge of some given composition was melted and a crystal was grown. The crystal pulling process was stopped during the crystal growth, the arc power turned off, and the crystal-melt allowed to freeze. Sections were taken from both sides of the crystal-melt juncture; combustion analysis was performed on the bottom of the grown crystal and on the region of the melt underneath the crystal. Crystals grown with compositions to the low O/Nb side of the congruent point have an O/Nb ratio larger than that of the residual melt. The opposite relation obtains for the high side of the congruent point, for example:

Sample	$x_{Crystal}$	x_{Melt}	
A	0.984	0.960	
B	0.994	0.986	
C	1.001	0.999	
D	1.006	1.006	$\Longleftarrow$ Congruent Point
E	1.010	1.020	
F	1.018	1.038	

A two-color optical pyrometer was used to measure the crystal-melt interface temperature for sample C and the temperature was found to be $1940 \pm 10°C$. No other sample interface temperatures were measured. If one carries out this crystal-melt analysis and utilizes pyrometry, then a rapid determination of the liquid-solidus lines is possible.

5.   One-Electron Energy Band Schemes

Niobium monoxide although structurally similar to rocksalt, has a

fourfold planar coordination around each niobium or oxygen atom instead

of the octahedral surroundings found in the complete rocksalt lattice.

All of the orbitals normally used in octahedral (TM-X) bonding or in

TM-TM (12-fold coordination) bonding are obviously not being used in the

same fashion as they might be used in, for instance, TiO. The three

d-t_{2g} type orbitals (d_{xy}, d_{xz}, d_{yz}), normally considered the metal-metal

bonding orbitals, that are associated with each niobium atom are not all

going to participate in metal-metal bonding as there are only eight near-

neighbor niobium atoms. For this same reason, some of the niobium

d-e_g, d-t_{2g}, and p orbitals as well as the oxygen p orbitals will not be

utilized in niobium-oxygen bonding. Since the rocksalt structure of the

TM carbides, nitrides, and oxides is apparently, highly stabilized by the

covalent π-bonding of metal t_{2g}-nonmetal p orbitals, the loss of some

of this bonding must be at least compensated by some mechanisms for

stabilization of NbO.

It might be appropriate to look first at a hypothetical TM-O compound

with the rocksalt structure, completely dense, and having the same

number of outer valence electrons as in NbO (11 electrons/molecule).

Figure 52 shows a schematic molecular orbital (MO) energy diagram

for this hypothetical material where only the cubic octahedral crystalline

field (Δ_{CF}) splitting has been considered. The cubic crystalline field

lifts the degeneracy of the five d-orbitals found in the free atom, splitting

the orbitals into two groups, one with a three-fold (t_{2g}) and the second with a two-fold degeneracy (e_g). The t_{2g} ligands are directed between the octahedral sites whereas the e_g ligands are directed at the octahedral sites and due to increased electrostatic repulsion have higher energy. When electrons are put into these orbitals, however, the levels may be reversed in energy depending on the number of d electrons in the metal origin atom, for example, with 1 d electron the levels stack t_{2g}, e_g with respect to energy but for 6 d electrons the levels invert[75]. The energy difference in the split d- levels is usually represented by 10 Dq and is determined from absorption spectroscopy. A range of 10 Dq for 2^+ ions in the iron transition series is available and is 7000 - 12000 cm^{-1} (~0.9 to 1.5 eV)[76]. The energies of the bonding (valence band) and antibonding (upper conduction band) σ-band orbitals of transition metal oxides are split by a 5-10 eV energy gap[1] with the TM d orbitals lying somewhere in between.

In the figure, $(E_M - E_I)$ represents the purely ionic stabilization, the Madelung energy minus the ionization energy for a given "effective charge" per ion. The numbers $[2]$ x $[n]$ refer to spin and orbital degeneracies per molecule. The level to which this scheme is filled (the Fermi energy) is dependent on the sum total number of outer valence electrons from the TM (d+s electrons) and from the oxygen (s+p electrons) atoms. The Fermi energy as drawn is for a total of eleven outer electrons and we see then that the first conduction band will be just half-occupied.

Transition metal compounds with exactly half-filled conduction bands, although the band may be antibonding with respect to the anion levels, tend to split into bonding and antibonding portions with a small energy gap leading then to a filled partial band. Such an occurrance results in a semi-conducting compound with possibilities of antiferromagnetic behavior. This may indeed be the case in the compounds vanadium monoxide [5] and chromium nitride [77].

The d-bands in Figure 52 are shown broadened indicating some t_{2g} orbital overlap between near neighbor TM cations. Optimum binding occurs for that configuration of t_{2g}-electron spins that permit the maximum amount of charge in the overlapping region midway between the positive cation cores [1]. If the electrons have parallel spins, they exclude one another from this region; therefore an antiferromagnetic correlation between electrons on neighboring cations stabilizes the binding. If the overlapping orbitals are half-or-less filled and if it is possible to propagate such order throughout the lattice, then antiferromagnetism should be expected. However, because of the large size of the double charged oxygen ions intervening between the TM neighbors and thus having its outer portion of the negative charge cloud in juxtaposition with the electrons in the overlapping TM t_{2g} orbitals, we should also expect some restriction on the amount of TM-TM binding. In effect, this would cause the d-levels to narrow into localized (nonbonding) levels creating a material with quite poor electrical conductivity due to the high mass of

the electrons and possibly strong magnetic behavior or crystal structure
distortions. The elimination of some of the intervening oxygen ions
(i.e. by the creation of oxygen vacancies) would then allow more metal-
metal bonding to occur. Tskhai and Gel'd [78] have calculated several of
the TM-TM overlap integrals for FeO, TiO, and VO and estimated that to
be found in NbO and have shown that the amount of metal-metal overlap
increases in this series almost proportionally to the percent of oxygen
vacancies present. The metallic character of the electrical conductivity
was shown to increase with the increase in oxygen vacancy content and a
low resistivity for NbO was deduced. Their deduction of the order of
magnitude of ρ (NbO) has been borne out by the present measurements.

Thus although we may conclude that a band scheme such as in
Figure 52 may lead to the creation of vacancies, it must also be
considered just as probable that unusual magnetic or electrical behavior
results. An interaction is also necessary to account for the apparent
t_{2g} band splitting that was seen to result from the parameterized S-K
scheme calculation of Section IVF.

If one now adds spin-orbit (SO) coupling to the MO-type scheme of
Figure 52 , then Figure 53 results. Spin-orbit coupling, in the d-orbitals
for instance, results from the unquenched angular momentum of the
electrons in various orbital configurations. What were originally (after
crystal-field effects) two groups of levels, the three-fold degenerate t_{2g}
orbitals and the two-fold e_g orbitals, now undergoes further splitting into

lower lying (in energy) two-fold degenerate t_{2g}-type orbitals (with

angular momentum $\ell = \pm 1$ leading to total angular momentum $J = 3/2$)

and three more-energetic individual levels (all with $\ell = 0$, $J = 1/2$)

including the remaining t_{2g} orbital and the two e_g orbitals. The energy

stacking of these three levels will depend on the relative magnitude of

the SO parameter, Δ_{S-O}, with respect to Δ_{CF}. Spin-orbit coupling does

not lower the overall center of gravity of the levels (as Δ_{CF} did not), but,

with metal-metal interactions that should be considered, the levels

broaden into bands albeit possibly narrow. The amount of broadening

and the possible eventual overlapping of the two parts of the band depends

on the magnitude of the cation orbital overlaps, and the size of Δ_{CF} and

Δ_{S-O}.

From Hermann and Skilman's tabulations [79], the SO splitting for V,

Nb, and Ta is estimated to be approximately 0.05, 0.3, and 1.0 plus eV,

respectively. These calculations were performed for the atomic level

splittings of the free atoms and so it is uncertain whether one can take

such calculations and apply them directly into a band scheme for a compound

since little is known of the true SO value in the type of compounds under

consideration here.

None-the-less, perhaps an important step towards understanding the

stabilization of the NbO structure can be seen in Figure 53 . We now

have the t_{2g} band separated into two parts indicating a different bonding

nature for one of the three t_{2g} type orbitals, a difference that one must

suspect on inspection of the odd structure of niobium monoxide. Three of

the four states in the lower portion of the split t_{2g} band (defined now as the $t_{3/2}$ band; the upper portion is to be called the $t_{1/2}$ band with two states) are filled when eleven electrons/molecule are considered. The comments previously made regarding oxygen vacancy formation for the easing of the possible screening of the metal-metal bonding still apply when Δ_{S-O} is brought into the model.

It is still questionable whether or not such a compound with the schematic band structure of Figure 53 will have the good metallic character evident in the measurements on NbO, nor is it clear whether sufficient motivation for TM-TM orbital overlap is present to create enough vacancies to approach that found in the NbO structure.

The question of metal-metal wave function overlap is apparently a critical point in the determination of the structure of niobium monoxide. The Nb-Nb intra-atomic distance in the stoichiometric compound is 2.977 Å. From Goodenough's work on collective vs localized electronic behavior in transition metal compounds [1], a so-called "critical distance", R_c, for niobium compounds of about 3.2 Å is obtained. If the TM-TM near neighbor distances are less than this R_c, then the metal-metal interactions are strong enough to form collective-electron d orbitals that belong to the entire transition metal array. We then expect there to be considerable overlap of the metal orbitals (of the t_{2g} type).

Thus with a large overlap of the niobium t_{2g} functions, we should expect numerous vacancies to be created in the lattice. The vacancies in the oxygen sublattice may be put to an additional use by the formulation of trap-mediated metal-metal bonding, a situation quite analogous to that found in $Pb_2Ru_2O_6 \square$ where an oxygen vacancy ($\square$) between four lead atoms traps 8 electrons[80] and uses them as binding electrons coupling the lead atoms. The introduction of oxygen vacancy trap levels into the NbO lattice enables electrons to be removed from the upper portion of the $t_{3/2}$ band leaving only the lower energy portion of the $t_{3/2}$ band occupied. The trap levels result then in an overall lowering of the total energy. The formation of a large number of ordered oxygen vacancies acting as electron traps should enhance the spin-orbit splitting since the ordered vacancy segregates the niobium d-functions in a manner similar to the S-O coupling. If the vacancy trap is located at $\left(\frac{1}{2} \ \frac{1}{2} \ \frac{1}{2}\right)$ in the crystal lattice, then it will have a complete octahedral surrounding of niobium atoms, all giving electrons to the trap levels and all bonded together through the electrons in the trap. Each of these octahedral complexes can then be coupled via Nb-O-Nb bonds that lie along the center of the faces of the unit cell (see Figure 3).

We are thus led to the postulation of trap-mediated bonding along with spin-orbit coupling as definitive mechanisms for stabilization of the NbO structure.

The one-electron energy band scheme for NbO deduced from these

considerations is shown in Figure 54 .   A diagram of the orientation of

the co-ordinate axes and of the orbital definitions used in Figure 54

are shown in Figure 55 .   Two alternative density of states curves that

may be obtained qualitatively from the MO-type schematic in Figure **54**

are shown in Figure 56 .   The shape of the density of states curve for

the valence π and σ bands (basically oxygen s and p type bands) is

deduced from the APW calculation of Ern and Switendick on TiO [28].

The 4d bands of niobium compounds are expected to be a little broader

than those of the 3d bands of titanium compounds because the d character

of the bands, which is strongest near the cores, is more highly screened

for the outer shells, and these therefore should be more free electron-

like.   An approximate energy scale has been attached to the energy axis

in Figure 56 using values of possible interband transitions obtained from

the Kramers-Kronig analysis of optical reflectivity data (Section IV E) and

subject to the assumptions stated there.

Figure 53 Schematic one-electron energy bands for hypothetical TMO rocksalt compound including crystalline field and spin-orbit interactions.
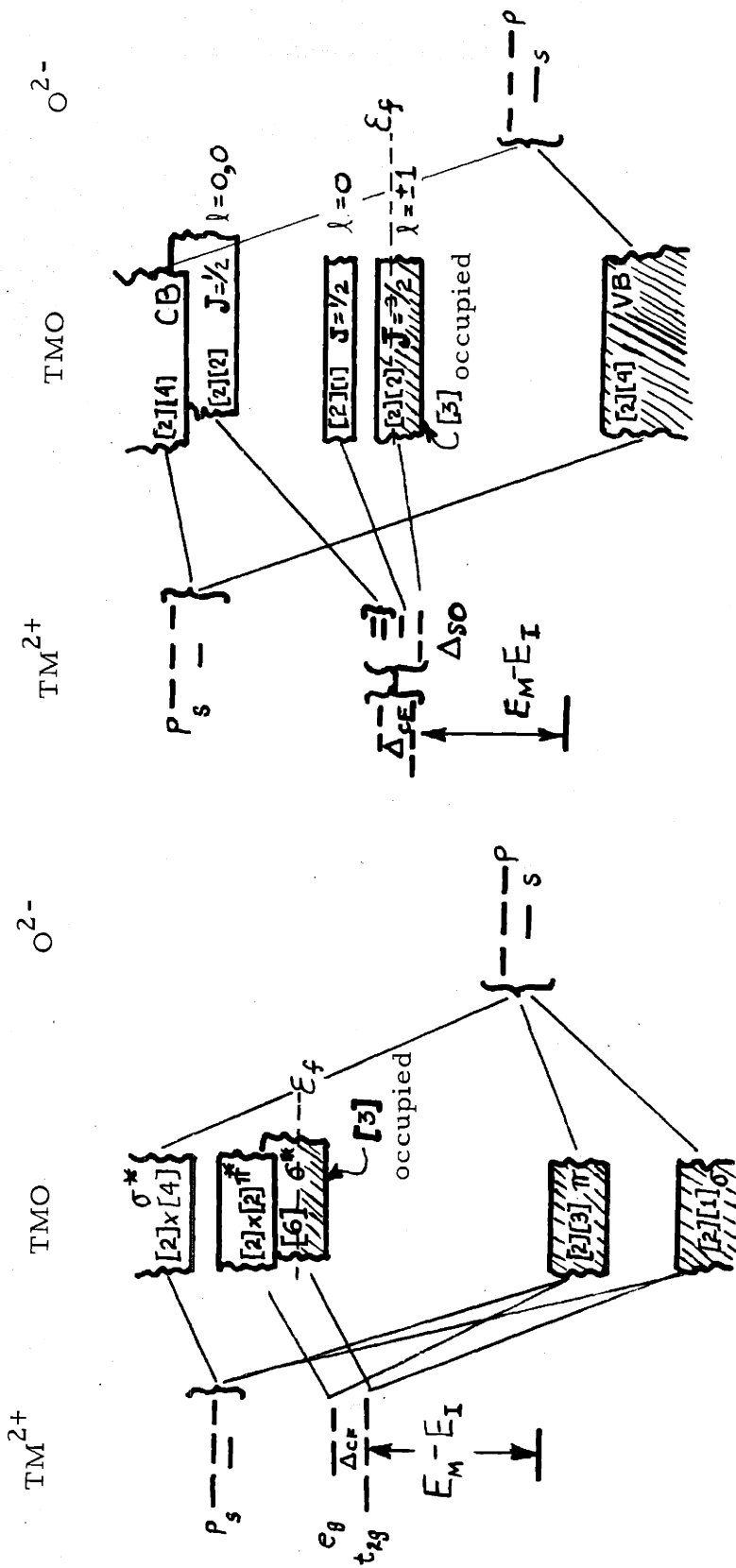
Figure 52 Schematic one-electron energy bands for hypothetical TMO rocksalt compound including crystalline field interactions only.
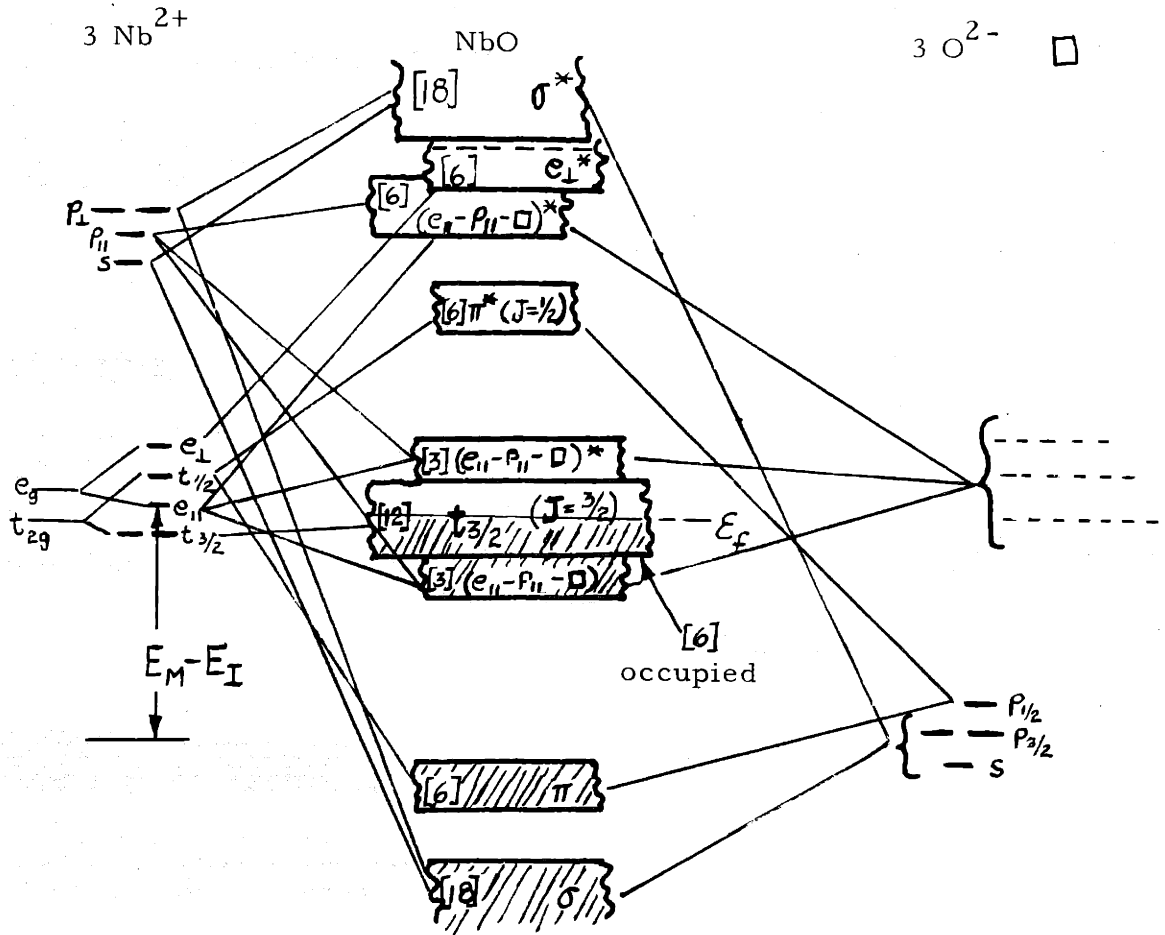
Figure 54   Proposed one-electron energy band scheme for niobium monoxide
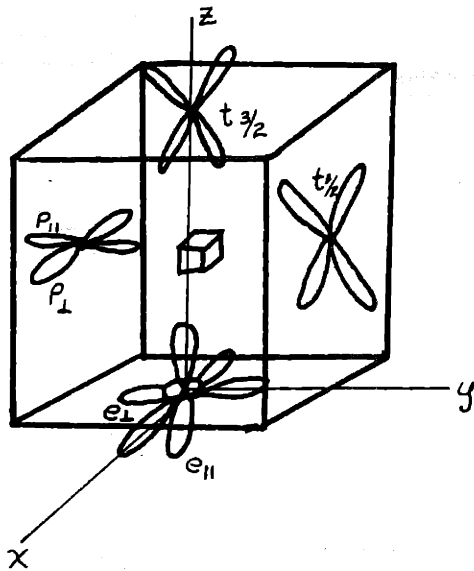
Figure 55   Co-ordinate orientation and orbital definition used in the determination of the one-electron energy band scheme for niobium monoxide
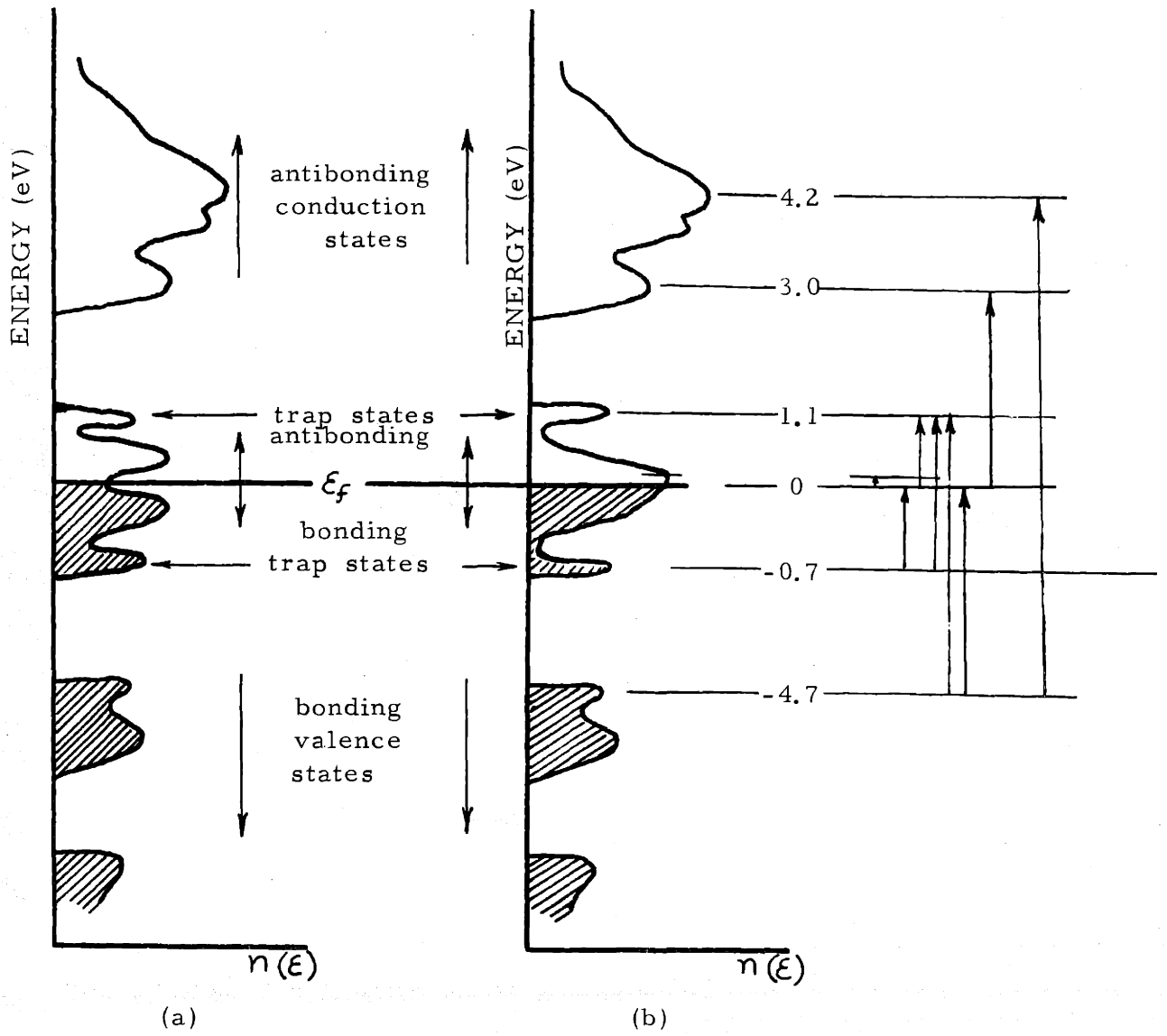
Figure 56   Alternative density of states curves deduced from the
proposed one-electron energy band scheme of niobium
monoxide. Part (a) depicts splitting of the half-filled
$t_{3/2}$ band whereas part (b) indicates no splitting. The
energy scale is obtained from the peaks in ϵ_2.

6.   Deviation From Stoichiometry

Oxygen Excess (x > 1). As the oxygen to niobium molar ratio is

increased beyond one, the stoichiometric ratio, the oxygen vacancy traps

will begin to be filled by O^{2-} ions. Each trap that is filled by an oxygen ion

will release about 1/6 electron per surrounding niobium atom into the

$t_{3/2}$ conduction band (a total of ~ one electron is released per O^{2-} added).

The Fermi level will be increased, but the binding energy must eventually

be decreased since the homogeneity range is not extensive. Although

there probably would be an initial enhancement of the binding energy due

to the increased number of partially ionic Nb-O bonds (borne out by the

fact that the congruent melting point is on the oxygen-rich side of

stoichiometry), the overall binding energy would be eventually decreased

by the loss of trap-mediated Nb-Nb bonds. At some point the filling of

trap sites, which leads to isolated, complete, TM_6X octahedra necessary

for the formation of numerous TMO_2 rutile phases, is sufficient to

cause the material to become a two-phase mixture. Thus, starting from

x = 1 and increasing the oxygen content results in an increasing number

of electrons free to participate in direct metal-metal or conduction

processes.

Niobium Excess (x < 1). On decreasing the molar ratio below one,

either more traps are created thereby removing electrons from the $t_{3/2}$

conduction band and lowering the Fermi energy, or some of the normally

vacant niobium sites are filled. The creation of more vacancy traps would

increase the oxygen vacancy content to above twenty-five percent violating

the proposed vacancy model. However, such an occurance should lead

to a rapid deterioration of the structure and a narrow single phase region

below $x = 1$. The introduction of one excess niobium atom into the

stoichiometric crystal brings the five outer (d+s) electrons into the crystal

as well as the ten d states of the niobium atom. The excess niobium d

states most likely become localized donor or acceptor levels. They will

be donors or acceptors depending on their energy positions relative to the

metal-metal t_{2g} bands (the $t_{3/2}$ and $t_{1/2}$ portions). It is unlikely that the

levels will be split by spin-orbit or crystal field interactions, but rather

will be strictly nonbonding levels. If the excess niobium atoms were to

participate in bonding with the surrounding oxygen atoms, then it is

difficult to see how the structure would become unstable at such a small

excess of niobium, and also one would expect an increase in the overall

binding energy due to the increased number of Nb-O bonds. It would be

anticipated that with such bonding, the homogeneity range would extend

down to at least Nb_4O_3 ($x = 0.75$).

In Table 3 , it was shown that with this type of proposed site filling

that the simple valence electron concentration as a function of composition

had a minimum at the stoichiometric ratio. If the excess niobium levels

are to be above the $t_{3/2}$ conduction band, the apparent number of effective

electrons across the full single phase field should also possess a minimum

at $x = 1$ as decreasing x below 1 leads to an increasing number of electrons.

If the isolated levels lie below the $x = 1$ Fermi level than one should

expect that the number of conduction electrons would increase continuously

from the low molar ratio end of the single phase field to the upper limit

of the homogeneity range.

V.   SUMMARY OF THE PROPERTIES OF NIOBIUM MONOXIDE

Single crystals of niobium monoxide as well as numerous other compounds were grown during the course of this work using a new type of crystal growing furnace, the Tri-Arc Czochralski Furnace (patent under process), especially developed by the author and Dr. T. B. Reed of Lincoln Laboratory for the growth of crystals of highly reactive materials. The furnace makes use of arc melting, a technique familiar to most metallurgists. The Tri-Arc unit is extremely small, very versatile, and inexpensive enough to be of great value to most any experimental solid state laboratory.

Some of the electronic and structural properties have been investigated for single phased compounds in the equi-atomic region of the niobium-oxygen equilibrium diagram.

The compound niobium monoxide was found to exist only in the narrow composition range of 0. 980 to 1. 020 ± 0. 002, oxygen to niobium molar ratio. The lattice parameter of the unit cell increased across the homogeneity range and had a value of 4.2111 ± 0.0002 Å at the stoichiometric composition. A congruent melting point was found to occur at the slightly oxygen-rich composition of 1. 006 oxygen/ niobium ratio at a temperature of 1940 ± 10°C. There is some evidence that the oxygen-rich congruent melting is an indication of a limited enhancement of the binding energy due to the increased number of (perhaps partially ionic) TM-X bonds expected with hyper-stoichiometric

compositions. The crystal structure of NbO was found to be in agreement with previous work and to have three niobium and three oxygen atoms arranged on face-centered sublattices in a simple cubic lattice, in analogy with an ordered 25 percent defected rocksalt lattice.

From the measured Hall voltage and electrical resistivity (4.2°K), the mobility was calculated:

$$\mu_H = \sigma R_H = (\frac{1}{7 \times 10^{-7}}) (3.9 \times 10^{-10} \times 10^6) = 5.46 \times 10^2 \frac{cm^2}{V-sec}.$$

The carrier concentration was determined from the Hall constant:

$$n = \left[(3.9 \times 10^{-4} \frac{cm^3}{coulomb}) (1.6 \times 10^{-19} \frac{coulomb}{electron}) \right]^{-1}$$

$$= 1.60 \times 10^{22} \text{ electrons per } cm^3.$$

The number of carrier electrons per niobium atom (effective) was then determined from the lattice parameter and the carrier concentration:

$$N = (3 \frac{Nb \text{ atoms}}{cell}) \quad (4.2110 \times 10^{-8})^3 \frac{cm^3}{cell} = 4.018 \times 10^{22} \frac{Nb \text{ atoms}}{cm^3};$$

$$n_{eff} = n/N = 0.40 \text{ electrons per niobium atom.}$$

The assumption was made that the effective mass of the carrier electrons was that of the free electron and so the relaxation time at 4.2°K was calculated from the number of effective carriers and the electrical conductivity:

$$\tau = \frac{m_o \sigma}{n e^2} = \frac{(9 \times 10^{-28})(1.4 \times 10^6 \times 10^{12})}{(1.6 \times 10^{22})(4.8 \times 10^{-10})^2} = 3.4 \times 10^{-12} \text{ sec.}$$

A comparison of the properties of $NbO_{1.0}$ and $TiO_{1.0}$ is made in Table 4.

TABLE 4

COMPARISON OF PROPERTIES OF $NbO_{1.0}$ AND $TiO_{1.0}$

PROPERTY	NbO	TiO [2]
σ (300°K)	5×10^4 (ohmcm)$^{-1}$	5.2×10^3 (ohmcm)$^{-1}$
σ (4.2°K)	1.4×10^6 (ohmcm)$^{-1}$	1.3×10^4 (ohmcm)$^{-1}$
R_H (4.2°K)	-3.9×10^{-4} cm^3/q	-1.5×10^{-4} cm^3/q
μ_H (4.2°K)	546 cm^2/V-sec	2 cm^2/V-sec
τ (4.2°K)	3.4×10^{-13} sec	2×10^{-15} sec
N	4.02×10^{22} $\frac{\text{Nb atoms}}{\text{cm}^3}$	4.75×10^{22} $\frac{\text{Ti atoms}}{\text{cm}^3}$
n	1.6×10^{22} elect./cm^3	4.2×10^{22} elect./cm^3
n_{eff}	0.4 elect./Nb atom	0.9 elect./Ti atom
m^*	assumed $= m_o$	$\sim 2\,m_o$
α_{TEP}	-0.7 μV/°K	-6.5 μV/°K
χ (300°K)	1.1×10^{-6} emu/gr	1.7×10^{-6} emu/gr
T_c	1.45 °K	< 1 °K
V_M, V_X	25 percent	15 percent
T_{mp}	1945°C	1750°C
color	silvery	dark gold

It is to be noticed from Table 4 that although the number of carriers is quite small in comparison to that found in other TM-X rocksalt compounds, the mobility (and the relaxation time) of the carriers is very large for a transition metal compound.

Spin-orbit coupling and oxygen vacancy-trap-mediated bonding were proposed as definitive mechanisms for the stabilization of the niobium monoxide structure. It was concluded that the presence of vacancy traps allowed electrons to be removed from more energetic upper portions of the conduction bands and put into lower lying trap levels. Vacancies in the oxygen sublattice effectively reduce the screening between near neighbor niobium atoms enabling orbital overlap (and thus metal-metal bonding) to increase. Spin-orbit coupling (splitting of the order 0.2 - 0.3 eV) lifted the 3-fold t_{2g} and the 2-fold e_g degeneracies in the niobium d levels giving rise to energy levels (a partially filled $t_{3/2}$ and an empty $t_{1/2}$ band) which were particularly appropriate for the NbO structure. A Slater-Koster L.C.A.O. calculation in the $\langle 100 \rangle$ direction of the simple cubic Brillouin zone, for the niobium t_{2g} orbitals only, resulted in the splitting of the t_{2g} levels in a fashion similar to that in spin-orbit coupling. A one-electron energy band scheme was deduced from the crystal structure keeping in mind the effects of spin-orbit coupling, of the Slater-Koster type of parameterized calculation, and of the vacancy-trap-mediated bonding model. The essential feature in this scheme that differs from that generally presented for the transition metal carbides and nitrides was the incorporation of vacancy trap levels which aided in emptying part of the lower conduction band. An approximate width of the $t_{3/2}$ conduction band

of 2 eV was inferred from optical reflectivity measurements and the ensuing Kramers-Kronig calculation from the reflectance data.

The Fermi level was deduced to be at or near a peak in the density of states curve. This deduction is based on the qualitative shape of the superconducting transition temperature versus composition curve, from the change in the slope of the curve of the Seebeck coefficient with composition, and from the negative slope of the magnetic susceptibility versus temperature curve. The Fermi level was considered to increase with an increase in oxygen/niobium molar ratio which led to an increased electron concentration in the niobium d-$t_{3/2}$ band. Evidence supporting this conclusion was obtained primarily from magnetoresistivity measurements which showed an increase in the occurrance of possible magnetic breakdown in the $\langle 100 \rangle$ and $\langle 110 \rangle$ directions of the Brillouin Zone with an increase in the oxygen/niobium ratio. Although the change in magnetic susceptibility (1 to 1.5×10^{-6} emu/gram) with composition for O/Nb > 1 indicated an increasing electron concentration with increasing oxygen content above the stoichiometric ratio, data below O/Nb = 1 were inconclusive. The electrical resistivity ($\sim 20 \times 10^{-6}$ ohm-cm), measured in a narrow composition range, exhibited no significant change.

A site filling model was presented whereby the hypo-stoichiometric lattice incorporated excess niobium atoms randomly onto niobium vacant sites and the accompanying Nb-d electronic energy levels were essentially nonbonding states below the Fermi level. Hyper-stoichiometry was

assumed to be accomplished by the filling up of the oxygen vacancy traps by oxygen ions and a subsequent release of electrons from the trap to the conduction band.

The non-existence of the monoxides of Hf, Ta, Mo, and W and the instability of the oxide ZrO[81] are most likely due to changes in the spin-orbit coupling parameter and the cubic crystal field splitting of the metal d orbitals. For instance, in comparison with Δ_{S-O} of Nb (0.2 to 0.3 eV), the spin-orbit splitting in Ta is approximately 1.1 eV; the Δ_{CF} in Ta is slightly smaller than in Nb so that the stacking of the d orbital energy levels in Ta (for oxide formation) will be highly mixed and unsuitable for a rocksalt structure. The extent of the d orbitals in proceeding from group IV (i.e. Zr) to group VI (i.e. Mo, W) increases slightly which would lead to increased overlapping in the metal-metal bonds. As pointed out in this thesis and in the work of Tskhai and Gel'd[78], the accommodation of increased metal orbital overlap is at the expense of creation of anion vacancies. A large decrease in the number of available oxygen atoms over that already found in NbO must lead to a decrease in the number of transition metal-oxygen bonds and a corresponding decrease in the stability of the compound.

VI. BIBLIOGRAPHY

1. J. B. Goodenough, Bull. Soc. Chim. France, p. 1200, 1965; see also Phys. Rev. 117, 1442 (1960).

2. S. P. Denker, J. Appl. Phys. 37, 142 (1966).

3. J. Stringer, J. Less Comm. Metals 8, 1 (1965).

4. G. F. Hardy and J. K. Hulm, Phys. Rev. 93, 1004 (1954); see also Bull. Am. Phy. Soc. 10, 44 (1965).

5. S. Kawano, K. Kosuge and S. Kachi, J. Phys. Soc. Japan 21, 2744 (1966).

6. R. Steinitz, to be published in the J. Phys. Chem. Solids.

7. W. Meissner, H. Franz and H. Westerhoff, Ann. Physik 13, 505 (1932).

8. H. Krebs, Acta Cryst. 9, 95 (1956).

9. P. W. Anderson, Phys. Rev. 115, 2 (1959).

10. R. E. Rundle, Acta Cryst. 1, 180 (1948).

11. L. Pauling, Nature of the Chemical Bond, third edition, Cornell Univ. Press, Ithaca, N.Y. (1960).

12. W. Hume-Rothery, Phil. Mag. 44, 1154 (1953).

13. P. Costa and R. R. Conte, Nuclear Metallurgy, ed. J. T. Waber and P. Chicotte, 10, 3 (AIME 1964).

14. E. Dempsey, Phil. Mag. 8, 225 (1963).

15. R. Kiessling, Acta Chem. Scand. 4, 209 and 146 (1950); see also Met. Rev. 2, 77 (1957).

16. D. A. Robins, Powder Met. 1/2, 172 (1958).

17. YU. N. Surovoi, L. A. Shvartzman and V. I. Alekseev, Fiz. Metal. Metalloved. 20, 251 (1965).

18. S. Nagakura, M. Kikuchi and S. Oketani, Acta Cryst. 21, 1009 (1966).

19. A. Z. Men'shikov and S. A. Nemnonov, Fiz. Metal. Metalloved. 19, 57 (1965).

20. D. W. Fischer and W. L. Baun, J. Chem. Phys. 43, 2075 (1965).

21. J. E. Holliday and J. Genin, International Symposium on X-Ray Spectra and Chemical Binding, Leipzig, 1965.

22. H. Bilz, Zeit. f. Phys. 153, 338 (1958).

23. J. C. Slater and G. F. Koster, Phys. Rev. 94, 1498 (1954).

24. G. C. Fletcher and E. P. Wohlfart, Phil. Mag. 42, 106 (1951); see also G. C. Fletcher, Proc. Phys. Soc. London A65, 192 (1952).

25. D. J. Howarth, Proc. Roy. Soc. London A220, 513 (1953).

26. W. Shockley, Phys. Rev. 50, 754 (1936).

27. D. H. Ewing and F. Seitz, Phys. Rev. 50, 760 (1936).

28. V. Ern and A. C. Switendick, Phys. Rev. 137, 1927 (1965).

29. G. Brauer, Z. Anorg. allgem. Chem. 248, 24 (1941).

30. S. Andersson, Acta Chem. Scand. 11, 1065 (1957).

31. A. L. Bowman, T. C. Wallace, J. L. Yarnell and R. G. Wenzel, Acta Cryst. 21, 843 (1966).

32. L. P. Bouckaert, R. Smoluchowski and E. Wigner, Phys. Rev. 50, 58 (1936).

33. R. P. Elliott, A.S.M. Trans. 52, 990 (1960).

34. S. P. Denker, to be published.

35. T. B. Reed and R. E. Fahey, Rev. Sci. Instr. 36, 289 (1965).

36. See C. A. Doremus, Trans. Amer. Electrochem. Soc. 13, 347 (1908) for early history of the electric arc.

37. C. A. Doremus, Trans. Amer. Electrochem. Soc. 13, 347 (1908).

38. H. Moissan, Comptes Rendues 116, 1225 (1893); see also 122, 1297 (1896).

39. W. Kroll, Trans. Electrochem. Soc. 78, 35 (1940).

40. S. Korman, International Science and Technology, p. 90, June 1964; see also C. Sheer, Plasma Technology, John Wiley and Sons, N. Y. (1966).

41. T. B. Reed, Advances in High Temperature Chemistry, Vol. I, ed. L. Eyring, Academic Press, N. Y. (1967).

42. T. B. Reed, to be published.

43. J. Feinleib and B. Feldman, Rev. Sci. Instr. 38, 32 (1967).

44. W. J. Scouler, Appl. Optics 3, 341 (1964).

45. P. L. Hartman, J. Opt. Soc. Am. 51, 113 (1961).

46. M. F. Merriam and M. Von Herzen, Phys. Rev. 131, 637 (1963).

47. B. D. Cullidy, Elements of X-Ray Diffraction, second edition, Addison-Wesley, Reading, Mass. (1959), p. 338.

48. W. G. Henry and P. A. Schroeder, Canad. J. Physics 41, 1076 (1963).

49. Thermophysical Properties of High Temperature Solid Materials, Vol. 1, ed. Y. S. Touloukian, McMillan Co. N. Y., (1967), pp. 724, 996, 1067.

50. D. J. Sellmyer, Rev. Sci. Instr. 38, 434 (1967); see also D. J. Sellmyer, J. Ahn and J.-P. Jan, Phys. Rev. 161, 618 (1967).

51. I. M. Lifshitz and V. G. Peschanski, Sov. Phys.-J.E.T.P. 8, 875 (1959) and 11, 137 (1960).

52. E. I. Blount, Phys. Rev. 126, 1636 (1962).

53. W. A. Harrison, Pseudo-Potentials in the Theory of Metals, W. A. Benjamin Inc., N. Y. (1966), p. 79.

54. W. S. Williams, Phys. Rev. 135, 505 (1964).

55. N. F. Mott and H. Jones, Theory of the Properties of Metals and Alloys, Dover Reprint (1958).

56. C. J. Kriessman and H. B. Callen, Phys. Rev. 94, 837 (1954).

57. T. H. Geballe, B. T. Matthias, J. P. Remeika, A. M. Clogston, V. B. Compton, J. P. Maita and H. J. Williams, Physics 2, 293 (1966).

58. M. D. Banus, personal communication.

59. T. Moriya, Enrico Fermi International School of Physics, Course XXXVII, Theory of Magnetism in Transition Metals, Academic Press, N.Y. (1967), p. 206.

60. A. H. Wilson, The Theory of Metals, Cambridge Univ. Press (1958).

61. N. F. Mott and H. Jones, Theory of the Properties of Metals and Alloys, Dover Reprint (1958), p. 312.

62. J. B. Goodenough, personal communication.

63. R. G. Lye, J. Phys. Chem. Solids 26, 407 (1965).

64. N. F. Mott, Proc. Roy. Soc. A153, 699 (1936).

65. J. Bardeen, L. N. Cooper and J. R. Schrieffer, Phys. Rev. 108, 1175 (1957).

66. W. L. McMillan and J. M. Rowell, Phys. Rev. Lett. 14, 108 (1965); also see (57).

67. F. J. Morin and J. P. Maita, Phys. Rev. 129, 1115 (1963).

68. J. C. Phillips, Solid State Physics, Vol. 18, Academic Press, N.Y. (1966), p. 55.

69. G. B. Wright, Appl. Optics 4, 366 (1964).

70. J. Feinleib, W. J. Scouler and A. Ferretti, to be published.

71. The Kramers-Kronig computer program was kindly loaned to the author by Dr. William Scouler of Lincoln Laboratory.

72. H. R. Philipp and E. A. Taft, Phys. Rev. 113, 1002 (1959); see also H. Ehrenreich, H. R. Philipp and B. Segall, Phys. Rev. 132, 1918 (1963).

73. J. Feinleib and W. Scouler, Lincoln Laboratory Solid State Division Quarterly Progress Report, 66-1, p. 33, (1966).

74. S. Westman and C. Nordmark, Acta Chem. Scand. 14, 465 (1960).

75. J. B. Goodenough, Magnetism and the Chemical Bond.

76. C. K. Jorgensen, Absorption Spectra and Chemical Bonding in Complexes, Pergamon Press (1962).

77. L. M. Corliss, N. Elliott and J. M. Hastings, The Antiferromagnetic Structure of CrN, Brookhaven National Laboratory Report BNL 4294.

78. V. A. Tskhai and P. V. Gel'd, J. of Struct. Chem. (USSR) 5, 278 (1964).

79. F. Herman and S. Skillman, Atomic Structure Calculations, Prentice-Hall, Inc., Englewood Cliffs, N. J., (1963).

80. P. Raccah, J. M. Longo and J. B. Goodenough, to be published.

81. R. P. Elliott, Constitution of Binary Alloys, first supplement, McGraw-Hill Co. (1965).

82. S. P. Denker, J. Phys. Chem. Solids 25, 1397 (1964).

83. S. A. Nemnonov and K. M. Kolobova, Fiz. Metal. Metalloved. 22, 680 (1966).

84. J. E. Robinson, Phys. Rev. 161, 533 (1967).

85. D. J. Sellmyer, personal communication.

VII. SUGGESTIONS FOR FURTHER WORK

A new Tri-Arc Czochralski Furnace has been constructed along with an improved purification train, thus, attempts at the growth of enhanced purity single crystals of NbO_x or other compounds in the transition metal rocksalt group should be made. The resistivity should be measured to see if there is any improvement in the resistivity ratio $(\rho_{300}/\rho_{4.2})$. The enhancement of the magnetic susceptibility at very low temperatures should then be measured. Since the superconducting transition temperature is very dependent on impurity content, for instance, 100 ppm of iron in molybdenum quenches the superconductivity, the values of T_c presented here should be remeasured.

With crystals of better quality, Fermi surface determinations should be attempted. There appears to be some oscillatory behavior in the magnetoresistance at the large fields used here.

Either extended Slater-Koster parameterized or an Augmented Plane Waves calculation should be performed. Attempts at establishing the potential that would be used in the APW method were made by the author with Dr. Peter DeCicco of the Solid State Physics Group of MIT, but the development of a potential for the vacant oxygen site in the center of the unit cell was not achieved. Careful X-ray integrated intensity measurements should be made to see how many (if any) electrons are involved in the hypothesized trap and as an aid in the development of the vacancy potential for use in APW calculations.

Finally, with improved purity crystals, low temperature reflectivity measurements should be made to see if any of the shoulders and merged peaks seen here can be resolved.

VIII.   APPENDIX

SLATER-KOSTER PARAMETERIZED CALCULATION FOR TITANIUM
MONOXIDE

The Slater-Koster (S-K) method[23] is particularly useful as an
interpolation scheme to develop analytical functions for the energy
dependence on wave vector for any direction in the Brillouin Zone or
at any given point in the zone whenever an accurate band structure
calculation (such as by A. P. W.) at several symmetry points has been
performed.

Ern and Switendick (E-S) have made an A. P. W. calculation for the
completely dense structures of TiC, TiN, and TiO[28].   The calcu-
lation was performed not only at the high symmetry points but also
at a few general points in the face center cubic Brillouin Zone requir-
ing approximately an hour of 7094 computer time per point.

Considering: 1) just nearest neighbors of like and unlike atoms,
2) only the five d-orbitals and the next higher s-orbital of titanium
and the s-p orbitals of oxygen, and 3) the transfer integrals to vanish
whenever the overlap integrals vanish, we obtain the following sets of
secular determinants and their associated equations.

At $\Gamma(000)$

$$\left.\begin{matrix} H_1 & H_{17} \\ H_{17} & H_7 \end{matrix}\right\} \Gamma_1$$

$$\left.\begin{matrix} H_8 & \\ & H_8 \\ & & H_8 \end{matrix}\right\} \Gamma_{15}$$

$$\left.\begin{matrix} H_2 & \\ & H_2 \\ & & H_2 \end{matrix}\right\} \Gamma_{2'5}$$

$$\left.\begin{matrix} H_5 & \\ & H_5 \end{matrix}\right\} \Gamma_{12}$$

where:

$$H_{11} = H_1 = s_1/s_1(000) + 12 s_1/s_1(110)$$

$$H_{77} = H_7 = s_2/s_2(000) + 12 s_2/s_2(110)$$

$$H_{17} = 6 s_1/s_2(100)$$

$$H_{88} = H_8 = x_2/x_2(000) + 8 x_2/x_2(110) + 4 x_2/x_2(011)$$

$$H_{22} = H_2 = xy/xy(000) + 4 xy/xy(110) + 8 xy/xy(011)$$

$$H_{55} = H_5 = z^2/z^2(000) + 6 z^2/z^2(110) + 6 x^2/x^2(110)$$

subscript 1 refers to a titanium atom and 2 refers to an oxygen atom; z^2 is used for $3z^2-r^2$ and x^2 for $(x^2 - y^2)$. From E-S, we get

$$\Gamma_{12} = 0.705, \quad \Gamma_{15} = 0.171, \quad \Gamma_{2'5} = 0.556, \quad \text{and } \Gamma_1 = \begin{Bmatrix} +0.708 \\ -1.073 \end{Bmatrix}.$$

Thus

1) $x_2/x_2(000) + 8x_2/x_2(110) + 4x_2/x_2(011) = +0.171$

2) $xy/xy(000) + 4xy/xy(110) + 8xy/xy(011) = +0.556$

3) $z^2/z^2(000) + 6z^2/z^2(110)\ 6x^2/x^2(110) = +0.705$

4) $\left[s_1/s_1(000) + 12s_1/s_1(110) - E_{\Gamma_1} \right]\left[s_2/s_2(000)\ 12s_2/s_2(110) - E_{\Gamma_1} \right]$

$$- 36\left[s_1/s_2(100) \right]^2 = 0.$$

At $X(0\pi 0)$ we have:

$$\left.\begin{array}{c} H_2 \\ H_2 \end{array}\right\} X_5$$

$$\left.\begin{array}{c} H_8 \\ H_8 \end{array}\right\} X_{5'}$$

$$H_3 - X_3$$

$$H_9 - X_{4'}$$

$$\frac{1}{4}\left[3H_6 + H_5 - 2\ 3\ H_{56} \right] - X_2$$

and

$$\begin{array}{ccc} H_1 & H_{17} & 2H_{16} \\ H_{17} & H_7 & 2H_{67} \\ 2H_{16} & 2H_{67} & \frac{1}{12}\left[12\ H_5 + 4\sqrt{3}\ H_{56} \right] \end{array}$$

where

$$H_1 = s_1/s_1(000) - 4s_1/s_1(110)$$

$$H_{16} = -4\ s_1/z^2(110)$$

$$H_{17} = 2\ s_1/s_2(100)$$

$$H_2 = xy/xy(000) - 4\ xy/xy(110)$$

$$H_3 = xy/xy(000) + 4xy/xy(110) - 8xy/xy(011)$$

$$H_5 = z^2/z^2(000) - 4x^2/x^2(110)$$

$$H_6 = z^2/z^2(000) - 4\,z^2/z^2(110)$$

$$H_{56} = 2\sqrt{3}\,z^2/z^2(110) - 2\sqrt{3}\,x^2/x^2(110)$$

$$H_{67} = 2\,z^2/s_2(001)$$

$$H_7 = s_2/s_2(000) - 4s_2/s_2(110)$$

$$H_8 = x_2/x_2(000) - 4x_2/x_2(011)$$

$$H_9 = x_2/x_2(000) - 8x_2/x_2(110) + 4x_2/x_2(011).$$

From E-S, we have

$$X_3 = +0.305, \quad X_5 = +0.842, \quad X_{5'} = +0.130, \quad X_2 = +0.807, \quad X_1 = \begin{Bmatrix} +0.818 \\ -1.010 \end{Bmatrix}$$

and $X_{4'} = \begin{Bmatrix} +1.104 \\ -0.039 \end{Bmatrix}$;

thus we may continue the series of equations

5) $xy/xy(000) - 4xy/xy(110) = +0.842$

6) $x_2/x_2(000) - 4x_2/x_2(011) = +0.130$

7) $xy/xy(000) + 4xy/xy(110) - 8xy/xy(011) = +0.305$

8) $x_2/x_2(000) - 8x_2/x_2(110) + 4x_2/x_2(011) = -0.039$

9) $z^2/z^2(000) - 6z^2/z^2(110) + 2x^2/x^2(110) = +0.807.$

If we now carry out the following:

    a) eqn. (2) - eqn. (7), we get $xy/xy(011) = +0.016$,

    b) eqn. (1) - eqn. (8), we get $x_2/x_2(110) = +0.013$,

    c) eqn. (2) - eqn. (5), we get $xy/xy(110) = -0.052$,

    d) eqn. (1) - eqn. (6), we get $x_2/x_2(011) = -0.008$,

if we now put c) into eqn. (5) we get $xy/xy(000) = +0.634$, and by putting

d) into eqn. (6) we get $x_2/x_2(000) = +0.098$ and we can readily see that

eqns. (7) and (8) are consistent.

For TiO with the aforementioned conditions, we obtain only 24 unknown parameters by considering the six points Γ, Σ, Δ, X, L, and W and we have 28 equations to work with involving the parameters to no more order than quadratic. Of these 24 parameters, we have already shown the evaluation of six of them, four more are obtained with ease:

$xy/xz(011) = +0.017,$

$xy/x_2(010) = \pm 0.064,$

$s_2/s_2(000) = -0.946,$

$s_2/s_2(110) = -0.011.$

To obtain the desired analytical functions, for instance, for the cation-s anion-s wave interaction between Γ and Δ, it is a routine matter to incorporate the trigonometric functions into the H equations. This is accomplished by looking up the proper overlap function in the S-K paper and multiplying the proper amount of sine and cosine for the point of interest (i.e. along $\overline{\Gamma \Delta}$) times the evaluated parameters. As an example, $H_{17} = 2s_1/s_2(100) \left[\cos \xi + \cos \eta + \cos \zeta\right]$. When this was done along $\overline{\Gamma X}$ and $\overline{\Gamma L}$ for several of the bands in TiO, the curves obtained by the author showed no discernable difference with the ones obtained by E-S.

BIOGRAPHICAL NOTE

The author was born February 4, 1938, in Memphis, Tennessee. He grew up and attended high school in the cosmopolitan community of Oak Ridge, Tennessee. After completing high school in 1956, he entered the Massachusetts Institute of Technology. In June, 1960, he was awarded the B.Sc. degree in the Department of Metallurgy.

For a year after graduation from M.I.T., he was employed as a Research Staff Member in the Department of Metallurgy under Dr. Roy C. Kaplow and Professor B. L. Averbach, carrying out research in X-ray diffraction studies of liquid metals and alloys.

From September, 1961, to September, 1963, he was employed as a research scientist by the Knolls Atomic Power Laboratory, a division of the General Electric Company, in Schenectady, New York. His investigations included theoretical and experimental studies of the thermal diffusivity and thermal conductance of nuclear reactor materials. While at K.A.P.L., he attended the night division of the Rensselaer Polytechnic Institute and was awarded the Master of Science degree in Metallurgical Engineering in June, 1963.

In September, 1963, he entered the Department of Metallurgy and Materials Science at M.I.T. and commenced studies for the Ph.D. degree. Minor programs in Physics and Mathematics were completed and thesis work was started under the direction of Professor Harry C. Gatos.

The author is married and the father of three small boys.